Dissertation
submitted to the
Combined Faculties for the Natural Sciences and for Mathematics
of the Ruperto-Carola University of Heidelberg, Germany
for the degree of
Doctor of Natural Sciences

Put forward by

Dipl.-Phys. Anis Dadi
born in Tunis, Tunisia

Oral examination: May 02, 2012

Nuclear Processes in Intense Light-Matter Interaction

Referees: **Prof. Dr. Dr. Carsten Müller**
Prof. Dr. Jürgen Schaffner-Bielich

Fakultät für Physik und Astronomie
Ruprecht-Karls-Universität Heidelberg

Zusammenfassung

Die vorliegende Dissertation beschäftigt sich in ihrer ersten Zielstellung mit der quantenmechanischen Berechnung der Protonenemission bei der Wechselwirkung eines kombinierten Feldes aus einem Laserstrahl und einem γ-Strahl mit einem Halo-Kern. Der totale Wirkungsquerschnitt ist wesentlich größer als der bekannte Wert für den Kernphotoeffekt, bei dem ein sehr energiereiches γ-Quant von einem stabilen Kern absorbiert wird. Desweiterens zeigen die Winkelverteilung und das Energiespektrum des emittierten Protons eine starke Abhängigkeit von der Polarisation und der Intensität des Laserfeldes sowie auch von der Orientierung seines elektrischen Vektorfeldes gegenüber dem Vektorfeld des γ-Strahls.

Die zweite Zielsetzung der Dissertation ist die Untersuchung der Paarerzeugung von Pionen beim Stoß eines hochenergetischen Laserfeldes mit einem ultrarelativistischen Protonenstrahl. Die phänomenologische Pion-Proton Kopplungstärke wurde bei $g_\sigma \approx 7.8$ festgelegt, so dass unsere Ergebnisse für den Prozess $\gamma + p \to p + \pi^+ + \pi^-$ mit den von DAPHNE gemessenen Wirkungsquerschnitten als Funktion der Energie des γ-Photons von der Energieschwelle bis ca. ≈ 480 MeV gut übereinstimmen. Die Ergebnisse wurden mit anderen Arbeiten über die Myonen-Paarerzeugung durch Multiphoton-Absorption verglichen. Obwohl die Myonmasse wesentlich kleiner als die Pionmasse ist, ist die Produktionsrate von $\pi^+\pi^-$ Paaren durch 2-Photon-Absorption dominant im Frequenzbereich zwischen ≈ 150 und 210 MeV.

Abstract

The emission of a proton from a halo-nucleus by absorption of a γ-photon in the presence of a strong laser beam is studied. It is shown that the maximum value of the total cross section, when plotted as a function of the γ-photon energy, is considerably larger than those obtained from experimental data of photoproton cross sections in stable nuclei. Furthermore, the angular distribution and the energy spectrum of the emitted proton exhibit a strong dependence on field geometries, polarizations and strengths.

The second project deals with the photoproduction of $\pi^+\pi^-$ pairs via multiphoton absorption from an intense x-ray laser wave colliding with an ultrarelativistic proton. By setting the pion-proton coupling constant to $g_\sigma \approx 7.8$, we reproduce the photoproduction cross section for the process $\gamma + p \to p + \pi^+ + \pi^-$ at 440 MeV as measured with the DAPHNE detector at MAMI. With this choice, we find reasonable agreement with the experimental data in the energy range from threshold up to ≈ 480 MeV. The results was compared with other works on multiphoton $\mu^+\mu^-$ production. Although the muon mass is substantially smaller than the pion mass, $\pi^+\pi^-$ production is found to be dominant in the frequency range between approximately 150 and 210 MeV.

In connection with work performed during the thesis, the following paper was published in a refereed journal:

- A. Dadi, C. Müller, "*Phenomenological model of multiphoto-production of charged pion pairs on the proton*", Phys. Lett. B **697**, 142 (2011).
- Anis Dadi and Carsten Müller, "*Laser-Assisted Photonuclear Effect in Halo-nuclei*", Phys. Rev. C **85**, 064604 (2012).

Contents

List of Figures

Notations, Units and Conventions

Throughout this thesis we will use the natural Heaviside-Lorentz (H.-L.) units

$$\hbar = c = k_B = \epsilon_0 = 1, \tag{1}$$

where $\hbar$ is the reduced Planck's constant, c is the velocity of light, k_B is the Boltzmann constant and ϵ_0 is the vacuum permittivity. So, units of all physical quantities will be attributed in terms of units of energy, i.e. in MeV, which is a typical energy scale in nuclear physics. The units of length and momentum are inverse of each other, units of length and time are same and units of energy, momentum and mass are also same. The H.-L. units set automatically the vacuum permeability $\mu_0 = 1$ since $c^2 = 1/(\epsilon_0\mu_0)$. The product of $\hbar$ and c has the dimension of energy times length and its value is[1]

$$\hbar \cdot c \approx 197.32 \text{ MeV} \cdot \text{fm} \stackrel{\text{def}}{=} 1, \tag{2}$$

We can use this fact to convert energy units into length units, for example the rest mass of $\pi^{\pm}$ meson is approx. 139.57 MeV or 0.707 fm^{-1}. Value of the fine-structure constant becomes $\alpha = e^2/4\pi \approx 1/137$, which clearly means that the elementary charge e is dimensionless and approximately equals to 0.3. The unit of the cross section σ is the micro-barn, and we have $1\ \mu\text{b} = 10^{-4}\ \text{fm}^2 \approx 2.5 \times 10^{-9}\ \text{MeV}^{-2}$.
Thus, to simplify the calculations, our strategy is first to express each physical quantity in MeV^r ($r \in \mathbb{Z}$) using convension (1), i.e. in H.-L. units, and then to convert it to SI units by dividing the result by a conversion constant, which relates both systems of units to each other. We have determined these conversion constants using the latest internationally recommended values of the fundamental physical constants from the "Committee on Data for Science and Technology" (CODATA) [1]. The results are shown in Table 1 below.

[1] We have $1\ \text{fm} = 10^{-15}$ m.

Quantity	Dimensions		Conversions: $1 \cdot [\text{SI Units}] = \textbf{const.}\ \text{MeV}^r\ (r \in \mathbb{Z})$
	SI Units	H.-L. Units	
Action	$\text{J} \cdot \text{s}$	none	$1 \cdot \text{J} \cdot \text{s} = \mathbf{9.4825229 \times 10^{33}}\ \text{MeV}^0$
Velocity	m/s	none	$1 \cdot \text{m/s} = \mathbf{3.3356411 \times 10^{-9}}\ \text{MeV}^0$
Elementary Charge	Coulomb	none	$1 \cdot e = \mathbf{0.302822122029789}\ \text{MeV}^0$
Length	m	MeV^{-1}	$1 \cdot \text{fm} = \mathbf{5.067731496528114 \times 10^{-3}}\ \text{MeV}^{-1}$
Mass	kg	MeV	$1 \cdot \text{kg} = \mathbf{5.609588830519812 \times 10^{29}}\ \text{MeV}$
Time	s	MeV^{-1}	$1 \cdot \text{s} = \mathbf{1.519267660720230 \times 10^{21}}\ \text{MeV}^{-1}$
Energy	$\text{J} \equiv \text{kg} \cdot \text{m}^2/\text{s}^2$	MeV	$1 \cdot \text{Joule} = \mathbf{6241509594067.40}\ \text{MeV}$
Temperatur	Kelvin	MeV	$1 \cdot \text{Kelvin} = \mathbf{8.617343169325341 \times 10^{-11}}\ \text{MeV}$
Momentum	$\text{kg} \cdot \text{m/s}$	MeV	$1 \cdot \text{kg} \cdot \text{m/s} = \mathbf{1.871157424341242 \times 10^{21}}\ \text{MeV}$
Electric Charge	Coulomb	none	$1 \cdot \text{C} = \mathbf{1.890067218174823 \times 10^{18}}\ \text{MeV}^0$
Electric Current	Ampere	MeV	$1 \cdot \text{A} = \mathbf{1.244064668156505 \times 10^{-3}}\ \text{MeV}$
Electric Potential	Volt	MeV	$1 \cdot \text{Volt} = \mathbf{3.302268582857398 \times 10^{-6}}\ \text{MeV}$
Electric Field	Volt/m	MeV^2	$1 \cdot \text{Volt/cm} = \mathbf{6.516265763429796 \times 10^{-17}}\ \text{MeV}^2$
Magnetic Field	$\text{Tesla} = 10^4\ \text{G}$	MeV^2	$1 \cdot \text{Tesla} = \mathbf{1.953527343534453 \times 10^{-10}}\ \text{MeV}^2$
Magnetic Potential	$\text{Volt} \cdot \text{s/m}$	MeV	$1 \cdot \text{Volt} \cdot \text{s/m} = \mathbf{989.995202432763}\ \text{MeV}$
Force	Newton	MeV^2	$1 \cdot \text{Newton} = \mathbf{1.23161801749548}\ \text{MeV}^2$
Power	Watt	MeV^2	$1 \cdot \text{W} = \mathbf{4.108235668696141 \times 10^{-9}}\ \text{MeV}^2$
Intensity	Watt/m^2	MeV^4	$1 \cdot \text{W/cm}^2 = \mathbf{1.599661676609436 \times 10^{-30}}\ \text{MeV}^4$
Production Rate	s^{-1}	MeV	$1 \cdot \text{s}^{-1} = \mathbf{6.582118647387887 \times 10^{-22}}\ \text{MeV}$
Cross-Section	$\text{m}^2 = 10^{28}\ \text{b}$	MeV^{-2}	$1 \cdot \mu\text{b} = \mathbf{2.568190187212365 \times 10^{-9}}\ \text{MeV}^{-2}$

Table 1: List of conversion **constants** for various physical quantities relating SI units to H.-L. units using the 2010 CODATA [1]. We shall use these values throughout this thesis.

–I–

Introduction

Since the beginning of the 20th century, nuclear physics has dealt with the physical properties, structures and reaction mechanisms of atomic nuclei and other forms of nuclear matter. It represents a fundamental branch of modern physics, which was developed intensely after the discovery of the atomic nucleus by Rutherford's famous scattering experiments in 1911. Before, it was difficult to prove the existence of the atomic nucleus because of its tiny dimensions and the shielding of its Coulomb field by the surrounding electrons in the atom. Rutherford's accomplishment thus signalled the birth of nuclear physics.

Two decades after the discovery of the atomic nucleus, photonuclear reactions have started to provide an important means to gain knowledge about the nuclear structure and nuclear forces. The research field was opened with the experiments by Chadwick and Goldhaber on the photodisintegration of the deuteron where γ-rays from a radioactive source were utilized [2]. Systematic investigations of the photonuclear effect were carried out since the early 1930's by Bothe and Gentner in Heidelberg which relied on high-energy γ-rays produced with the aid of a proton accelerator [3]. From 1934 to 1957, various research activities on the photonuclear effect have been initiated at the Kaiser-Wilhelm Institute for Medical Research (KWImF). After Bothe's death in 1958, the KWImF became the Max Planck Institute for Nuclear Physics (MPIK) and the two main building were later named Bothe- and Gentner laboratories.

Photonuclear reactions are dominated by various giant resonance phenomena [4] occurring in the energy level spacing from a few to several tens of MeVs. Studies of such resonance phenomena are of particular importance in determining bulk properties of atomic nuclei (masses, radii, compression moduli, separation energies) and also in investigating radiation from unstable nuclei. In addition, studies of the photonuclear effect have made important contributions to the understanding of some astrophysical processes [5, 6] and for producing artificial radioisotopes as well as proton and neutron sources, which have been used in a variety of applications such as in nuclear medicine, radiography, chemistry and fusion reactors.
Until now, experiments on photonuclear reactions have typically applied energetic photons from synchrotron, electron bremsstrahlung or Compton backscattering sources [7, 8]. However, due to a large and still ongoing technological progress during the last two decades, intense coherent photon beams from powerful laser sources are emerging nowadays into a novel tool for photonuclear studies [9–12], opening the research field of laser-nuclear physics. A facility devoted particularly to laser-nuclear physics is currently being constructed as part of the Extreme Light Infrastructure project [13].

Direct interactions between laser fields and nuclei are usually very weak because of the large mismatch of the relevant energy scales: Both the laser photon energy and the electric work performed by the laser field over the nuclear extension are smaller than the typical nuclear level spacing by orders of magnitude. Indirect laser-nucleus coupling schemes have therefore mostly been considered which are mediated by secondary particles such as electrons. Prominent examples are nuclear reactions in laser-produced plasmas where, for instance, photofission and the generation of photoneutrons through high-energy bremsstrahlung emission by laser-accelerated electrons has been observed [10–12]. The emission of secondary bremstrahlung γ-rays have also led to the observation of an efficient e^+e^- pair production through the Bethe-Heitler effect [14]. The setup also offers prospects for Bethe-Heitler creation of muon pairs [15] and single pion photoproduction through the

reaction [16] $p+\gamma \to n+\pi^+$. Particle reactions such as $\mu^+\mu^-$ and $\pi^+\pi^-$ production were also considered in an e^+e^- plasma coupled to a photon field [17–20]. Theoreticians have investigated moreover laser-assisted internal conversion [21–23], the electron-bridge mechanism [24], nuclear excitation in laser-driven muonic atoms [25]. In view of the ever increasing available laser intensities as well as frequencies also the possibilities for direct laser-induced nuclear reactions are meanwhile being studied. Resonant photoexcitation of nuclear transitions may occur when an intense x-ray laser pulse interacts with a counterpropagating nuclear beam of moderately relativistic energy [26, 27]. For certain applications, it could also be interesting to combine a laser beam with an incoherent radiation source such as x-rays or γ-rays. The study of the (γ, p) reaction and the streaking of low-energy protons may be performed experimentally using the proton streaking technique, where a high-frequency laser beam (of a few attoseconds or 10 keV photons) is used to measure the lifetimes of such nuclear processes [13].

Apart from direct laser-induced nuclear processes, also laser-assisted processes are of interest. These are processes which can already occur without the presence of a laser field and may be modified when a laser field is present. Examples are the laser-assisted internal conversion mentioned above as well as laser-assisted nuclear β-decay, which was studied by several authors [28, 29]. Laser-assisted processes have been studied thoroughly in atomic physics. They comprise laser-assisted electron-atom scattering, laser-assisted x-ray scattering, laser-assisted Mott and Møller scattering and laser-assisted electron-ion recombination. In particular, the laser-assisted photoeffect in atoms has been investigated intensively both in theory and experiment [30–35] in recent years. These studies were motivated and rendered feasible by the availability of synchronized IR and XUV beams, with the latter being produced by a Free Electron Laser (FEL) or High Harmonic Generation (HHG). Characteristic modifications of the photoelectron spectra due to the presence of the low-frequency field have been found. Besides, the process may be utilized to probe the properties of the ionizing FEL/HHG pulse. Here too it would be important to study analogue laser-assisted processes in nuclear physics.
Also, particle accelerators are important tools for fundamental nuclear physics research. The latest generation of high-current particle accelerators (linac, synchrotrons, cyclotrons) are used for increasing the energy of charged particles, up to multi TeV scale. The Tevatron Collider at the Fermi National Accelerator Laboratory (Fermilab) can run at a center of mass energy of 1.96 TeV, and the Large Hadron Collider (LHC) at CERN up to 3.5 TeV per beam with a final expected energy of 7 TeV. When such particles interact directly with intense laser beam, nonlinear quantum electrodynamic (QED) and hadronic processes can well occur, because the frequency and field strength of the electromagnetic field are largely Doppler-enhanced in the particle rest frame. In the late 1990's, multiphoton e^+e^- pair production was observed in ultrarelativistic electron-laser collisions by a pioneering experiment [36] at the Stanford Linear Accelerator Center (SLAC) in the USA. It would be interesting to look at analogue multiphoton processes in hadronic physics. In recent years the interest in the process of pion photoproduction has been revived by improved experimental data which were obtained by using polarized tagged photon beams at the Mainz Microtron (MAMI) in Germany [37, 38], the GRAAL facility in Grenoble/France [39–41], and the Jefferson Laboratory located in Newport News/USA [42–44]. At GRAAL, the high-energy photon beam is produced by Compton backscattering of laser light on a relativistic electron beam. These studies allow insights into the internal structure and excitation spectrum of the proton. A particular focus lies on polarization asymmetry measurements which are sensitive to interference cross terms.

In the present work we will use single or several photons of energy between 2 eV to 3 MeV from different kinds of radiation sources to study different problems associated with nuclear and hadronic processes in super-intense light-matter interaction. Our first study include the photonuclear effect when an exotic halo-nucleus interacts with a combined field consisting of a strong optical laser and a high-energy photon (such as a γ-ray). Here we shall use a halo-nucleus because of its small binding energy (between 0.1 and 1 MeV) and large spatial extension (between 3 and 9 fm), so that photonuclear reactions can easily be induced by using high-energy photons. We therefore expect that photonuclear cross sections are much easier to measure for halo-nuclei than for stable ones. It is important to note that the current realistic and phenomenological models of atomic nuclei, which have been developed to explain the data from (photonuclear reactions and scattering) experiments using stable nuclei only, are in disagreement with a wide range of experiments on the properties of exotic nuclei. We investigate a laser-assisted process which may help to gain new insights in the understanding of exotic states of nuclear matter, and hence to make more consistency between theory and experimental observations. In a second study, we consider the laser-induced pion pair production in ultrarelativistic proton-laser collisions. This study combines the well-established approach to multiphoton QED processes [45–47] with a phenomenological

hadronic model to describe the pion-nucleon interaction. We note that the hadronic interaction is assumed to be mediated by the exchange of isoscalar-scalar σ mesons, and the laser photons participate directly in the pair production process in contrast to the indirect participation mentioned above [10–12, 14]. Such investigation might add important insights to understand the Coulomb and nuclear effects in nuclear matter, parallel to the physics of heavy ion collisions and the astrophysics.
In general terms, the present studies may be considered a first step towards an extension of the theory of laser-dressed QED into the realm of nuclear- and hadronic physics. Our general goal is to generalize tools and knowledge from atomic physics and QED in strong laser fields to laser-nuclear physics.

The present thesis is organized in five Chapters with accompanying two Appendices for Chapters 4 and 5, that contain detailed informations about mathematical techniques that help the reader to understand our projects better. In order to justify our motivation to carry out this work, we give in Chapter 2 a background in nuclear and laser physics, by presenting in Section 2.1 an overview on the basic properties of nuclei and on the nuclear models, and then in Section 2.2 an overview on the historical and future development of intense radiation sources. Chapter 3 provides theoretical methods for the main topics used in this thesis as well as it builds a theoretical framework for further analysis. In Chapter 4 we study the photonuclear effect occurring in the combined electromagnetic fields of γ-rays and an intense laser beam. The proton is emitted by the photonuclear effect, which is assisted here by the strong laser field. In the theoretical part 4.3, we calculate the total and differential cross section of the process by using an approximate wave function of the initially bound halo state. The final state is approximated by a nonrelativistic Volkov wave function in the continuum. In Section 4.4, we investigate the cross section in terms of the number of the absorbed laser photons, the photon energy of the γ-radiation and the polar emission angle of the proton-halo. Chapter 5 deals with the production of $\pi^+\pi^-$ pair via multiphoton absorption from an intense x-ray laser wave colliding with an ultrarelativistic proton beam. In the theoretical part 5.2, we calculate the differential and total cross section of the process by including the contributions from both the electromagnetic and hadronic interactions, where the latter are described phenomenologically by a Yukawa potential. Order-of-magnitude estimates for $\pi^+\pi^-$ production on the proton by two- and three-photon absorption from the high-frequency laser field are obtained in Section 5.3 and compared with the corresponding rates for $\mu^+\mu^-$ pair production. Finally, our conclusions and outlook follow in Chapter 6.

–II–

Background in Nuclear and Laser Physics

2.1 Basic Concepts in Nuclear Physics

There is compelling experimental evidence that the fundamental constituents of matter are six flavor quarks (u, d, s, c, b, t) possessing three types of color charge, and six leptons $(e, \nu_e, \mu, \nu_\mu, \tau, \nu_\tau)$. The atomic nucleus consists essentially of bound states of uncharged neutrons and positively charged protons, that are made up of quarks. In the nucleus, all the four fundamental forces known at present appear. According to quantum physics, the forces between elementary and composite particles in the nucleus arise from an exchange of field quanta. The field quanta for the electromagnetic interaction are photons, massless and electrically neutral bosons with spin one. At the subnuclear level, or in other words in quantum chromodynamics (QCD), the field quanta for the strong interaction are eight gluons carrying color-anticolor charge pair, and therefore they can interact strongly among themselves. Gluons are responsible for the binding of protons and neutrons in the very small space volume of a nucleus, otherwise they would drift apart by the electromagnetic forces.

2.1.1 Properties of Stable Nuclei

What do we know about the physical properties of nuclei? To date, modern scattering experiments and high-resolution spectroscopic methods provide direct evidence for the following physical properties of the atomic nucleus:

(a) The masses of the proton and neutron in the nucleus are approximately the same. The force between two protons is equal to the force between two neutrons (i.e., charge independence of the nuclear force), but it depends strongly on the relative spin orientation. These properties can be proven by studying the inelastic scattering of protons and neutrons by deformed exotic nuclei or by studying the mirror nucleus. Therefore, one introduces the concept of isospin symmetry by considering the proton and the neutron as two different quantum states of the same particle, the nucleon.

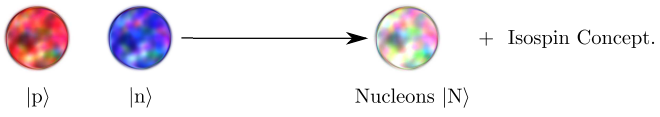

(b) The nuclear force has a very short range (approximately π-meson Compton wavelength). This property provides a good approximation of the nuclear radius, which can be determined by measuring the isotope shift in atomic transition frequencies by use of high precision laser-resonance spectroscopy on single atoms or by the scattering of low-energy electrons from nuclei. The root mean square (rms) charge radius is estimated by [48, 49]

$$r_{\mathrm{rms}} \approx r_1 \cdot A^{1/3} \text{ fm}, \tag{2.1}$$

with $r_1 = 1.16$ fm and A is the total number of nucleons in the atomic nucleus. That is, for the stable isotopes in the periodic table of elements we have

$$1 \text{ fm} \lesssim r_{\text{rms}} \lesssim 5 \text{ fm}, \tag{2.2}$$

which is roughly 10^5 times smaller than the atomic radius.

(c) There is no attractive center, which produces the (strong) binding potential. The exact form of the nuclear potential is not precisely known at present, while in the atom, the Coulomb potential ($\propto 1/r$) is responsible for binding the electrons to the nucleus.

(d) A nucleon may only interact (strongly) with a fixed number of its nearest neighbors and next-nearest neighbors. If one adds a further nucleon, only the nuclear volume becomes larger, not the binding energy per nucleon. From this it follows that the atomic nucleus is a saturated system.

(e) The nuclear interior is homogeneous and isotropic; that is, all directions are equivalent and there is no direction preferred to others. This rotational symmetry is very helpful for investigating the equation of state (EoS) for nuclear matter and generally in theoretical nuclear physics.

(f) The mean free path of the nucleon is much larger than the nucleon size or even larger than the nuclear medium itself, so that one can apply a model of "*independent particles*".

From these physical properties, the atomic nucleus can be compared with a liquid drop, where nucleons play the role of "*molecules*" in normal liquid. This phenomenological ansatz is known as "*liquid-drop model*", whereby the behavior of the total binding energy B is determined as function of the total number A of nucleons and its different values for different isotopes. For a given stable nucleus of volume V and total mass M, consisting of Z bound protons and $N = A - Z$ bound neutrons of free masses m_{p} and m_{n}, one assumes B to be approximately the sum of different types of energies,

$$\begin{aligned} B &= B_{\text{volume}} + B_{\text{asymmetry}} + B_{\text{surface}} + B_{\text{Coulomb}} + ..., \\ &= a_{\text{v}} \cdot A - a_{\text{sym}} \cdot \frac{(N-Z)^2}{A} - a_{\text{surf}} \cdot A^{2/3} - a_{\text{C}} \cdot Z(Z-1)A^{-1/3} + ..., \end{aligned} \tag{2.3}$$

which is equal to the mass defect $M - Zm_{\text{p}} - Nm_{\text{n}}$. This is known as the semi-empirical mass formula [50] (sometimes also called the Bethe-Weizsäcker mass formula). The coefficients a_{v}, a_{sym}, a_{surf}, and a_{C} are constants that can be calculated empirically by fitting to experimentally measured masses of different nuclei. The first term corresponds to the volume energy, which results from the mutual attraction between nucleons. Because the attraction is short-range and rotationally symmetric, the binding energy per nucleon $\mathcal{E}_b \equiv B/A$ is considered to be independent of A, and thus B is proportional to A. So the first term gives an explanation of the experimentally observed constant density of nucleons n_{B}, whereby the volume V is proportional to the number $A = V \cdot n_{\text{B}}$ of nucleons. If we simply estimate V as $4\pi r_1^3/3$ and using Eq. (2.1), the saturation density in the nuclear interior amounts to an extremely high value of

$$n_{\text{B}} = (n_{\text{p}} + n_{\text{n}}) \approx 0.153 \text{ Nucleons/fm}^3, \tag{2.4}$$

where $n_{\text{p}} = Z/V$ and $n_{\text{n}} = N/V$ are the densities of protons and neutrons, respectively. Furthermore, the empirical value of the binding energy per nucleon is known with good accuracy from experimental data [48, 49]

$$5 \text{ MeV} \lesssim \mathcal{E}_b \lesssim 8 \text{ MeV}. \tag{2.5}$$

This value can be obtained from the semi-empirical mass formula (2.3) by considering an isospin symmetric nuclear matter ($n_{\text{n}} = n_{\text{p}}$) in the thermodynamic limit ($A, V \to \infty$), so that all terms vanish except the volume energy. The second term in expression (2.3) has a quantum mechanical meaning, namely, the nucleus can be considered as a quantum degenerate Fermi gas, in which all energy levels are occupied separately by protons and neutrons up to the Fermi energy. From the Pauli exclusion principle, each level allows just two particles of the same type with opposite intrinsic spin orientations. Owing to this prevention, the more nucleons are added, the higher are the energy levels that they have to occupy, increasing the total energy of the medium and decreasing

the binding energy (the latter will be maximum when protons and neutrons occupy the lowest possible levels). If there is an unequal number of protons and neutrons (usually there are more neutrons than protons), the energies of the highest occupied proton and neutron levels, which are the Fermi energies, are unequal. In that case, a contribution to the binding energy should assure that protons and neutrons have the same Fermi energy; otherwise, the energy difference would be balanced through $\beta^{\pm}$-decay of neutrons into protons or vice versa. This contribution is the asymmetry energy. Thus, the asymmetry energy supports the equilibrium between proton and neutron number, vanishes for $n_{\rm n} = n_{\rm p}$, and reduces the total binding energy B for increased the difference $n_{\rm n} - n_{\rm p}$. The empirical value of the asymmetry energy coefficient at the saturation density (2.4) is also well known [51]:

$$a_{\rm sym} \approx 32.5 \text{ MeV}. \tag{2.6}$$

The third term in the mass formula (2.3) describes the relationship from the surface to the volume of the nucleus. The nuclear binding energy is much larger for the central nucleon than that for the surface nucleon, because the latter is surrounded by fewer nearest neighbors than a nucleon inside the nucleus. From there, a destabilizing term (i.e. with minus sign) is needed, which is proportional to the surface of the nucleus. Since V is proportional to A and the nuclear radius to $A^{1/3}$, the surface term should be proportional to $A^{2/3}$ as shown by Eq. (2.3). Finally, the fourth term appearing in the mass formula, which is known as the Coulomb term, takes into account the electrostatic repulsion of the $Z(Z-1)/2$ pairs of protons in the nucleus. The expression of the Coulomb term, as given by this equation, can be approximately calculated using the potential energy of such a charge distribution in a spherical nucleus (i.e. of radius proportional to $A^{1/3}$). We note that there are many other correction terms we have not included in the above semi-empirical mass formula and they will not be discussed in this Chapter.

The next important quantity in the study of nuclear properties is the nucleon effective mass $m_{\rm N}^*$, which results from the mass defect of the nucleon owing to the interaction with its nearest neighbors. From experiments, one determines $m_{\rm N}^*$ by measuring the density of states of the nucleon and the single-particle energy levels in nuclei [52]. However, a precise value is not known at present. So far as known, the range at saturation density, far away from the Fermi surface and for $n_{\rm n} = n_{\rm p}$, is [53, 54]

$$656.8 \text{ MeV} \lesssim m_{\rm N}^* \lesssim 750.6 \text{ MeV}. \tag{2.7}$$

As we mentioned in the Introduction, photonuclear reactions have proved to be valuable tools for the studies of giant resonance phenomena in nuclei which occur in the energy range between a few and several tens of MeVs [4]. These studies are of particular importance in determining the compression modulus $\mathcal{K}$ of the atomic nucleus. This quantity is related with the collective oscillation processes of protons against neutrons in the nucleus, which can be excited to oscillate collectively through absorption of γ-quanta via the photonuclear effect or through inelastic scattering of α particles. Thereby, there are radial (monopole) and nonradial (dipole or quadrupole) oscillations, in which the deformation of the nucleus changes with the oscillation periods. Concretely, the compression modulus can be extrapolated from experimental data on the strength function distribution of the isoscalar giant monopole resonance (GMR) in different heavy nuclei [55–57]. Like the nucleon effective mass, a precise value of the compression modulus is not known at present, but in recent years it has been estimated to be in the range [57–60]

$$230 \text{ MeV} \lesssim \mathcal{K} \lesssim 250 \text{ MeV}. \tag{2.8}$$

As an example, we mention that the value $\mathcal{K} \simeq 234.0$ MeV, has been estimated by Myers and Swiatecki [49] using Thomas-Fermi model calculations. Youngblood *et al.* have reported [56] that $\mathcal{K} = 231 \pm 5$ MeV by measuring the strength function distribution of the GMR in ^{90}Zr,^{116} Sn,^{144} Sm, and ^{208}Pb using inelastic scattering of 240 MeV α particles at extremely forward angles.

2.1.2 Properties of Exotic Halo Nuclei

In some cases, the properties of nuclei might be different from those discussed in the previous Subsection 2.1.1, i.e. regarding their sturctures, density distributions, binding energies, symmetries, etc. These kind of nuclei are referred to as "*exotic nuclei*". One important species is the so-called "*halo-nuclei*". A halo-nucleus contains a tightly bound inner core surrounded by a few outer nucleons that are loosely bound to it. The outer "*halo*"

nucleons are unusually far from the nuclear-core leading to a relatively large rms matter radius between [61]

$$3 \text{ fm} \lesssim r_{\text{rms}} \lesssim 9 \text{ fm}, \tag{2.9}$$

which is substantially higher than the value predicted by the liquid drop model in Eq. (2.1). The binding energy, that holds a nucleon-halo to the nuclear-core is usually between

$$0.1 \text{ MeV} \lesssim \mathcal{E}_b \lesssim 1 \text{ MeV}, \tag{2.10}$$

which is substantially smaller than the binding energy (2.5) of stable nuclei. In general, we can divide halo-nuclei into neutron-halos and proton-halos. The number of neutron-halos discovered so far exceeds significantly the number of proton-halos due to the Coulomb barrier and the $l = 1$ angular momentum barrier, which hinder the proton to penetrate into the out region of the nuclear-core. The formation and stability of halo-nuclei cannot be explained by the classical physics but by the quantum physics. The most known quantum-mechanical effect taking place is the quantum tunnelling, where the wave function of the nucleon-halo tunnels out of the nuclear-core to the classical forbidden region, and hence giving rise to the large rms radius (2.9). Another important effect is the asymmetry energy contribution to the nuclear binding energy as explained above, since halo-nuclei are generally very neutron-rich or proton-rich systems with low A. The larger the proton-neutron asymmetry in the nucleus, the smaller the saturation density, and hence the lower the binding energy that holds nucleons together in the nucleus. In a previous work [62], we have found that nuclei become unbound at a proton-neutron fraction $\eta \equiv (n_{\text{n}} - n_{\text{p}})/(n_{\text{n}} + n_{\text{p}})$ slightly larger than 0.8. This region is called "*drip line*", at which halo-nuclei may be formed. As a consequence, halo-nuclei are characterised by their short lifetimes, so generally between

$$0.43 \text{ ms} \lesssim \tau_{\text{halo}} \lesssim 64.5 \text{ s}. \tag{2.11}$$

The first and the most well-studied case is the neutron-rich ^{11}Li. This isotope was identified as a two-neutron halo-nucleus by Tanihata and co-workers in 1985 at Berkeley [63] from the measurement of the interaction cross sections of a high-energy radioactive beam of ^{11}Li with various target elements. In 1987, Hansen and Jonson [64] explained the large matter radius of ^{11}Li by considering it as binary system of a stable ^{9}Li core (containing three protons and six neutrons) surrounded by a halo of two neutrons. The ^{6}He and ^{11}Be isotopes with two- and one-neutron halo, respectively, have also been well studied in many experiments [65, 66] by measuring the experimental differential and integrated cross sections for their elastic breakup on ^{12}C and ^{208}Pb targets. Few other halo-nuclei have also now been confirmed or predicted, such as the ^{19}C with one-neutron halo [67], ^{17}B, ^{19}B and ^{22}C [68] with two-neutron halos, the ^{8}He and the ^{14}Be with four-neutron halos. Notice that two-nucleon-halos are called Borromean nuclei, because they share with Borromean rings (named after the Borromeo family from the 15th century) the property of making the three-body nuclear system unbound when any one of them is removed. Nevertheless, nuclei which have a one-proton-halo include ^{8}B and ^{26}P [69–76], presumably the ^{17}Ne with two-proton-halos [77] and the ^{100}Sn with one-proton-halo [78]. Let us focus on the ^{8}B, because we will need it later in Chapter 4. This isotope contains a formed heart of four protons and three neutrons surrounded by a halo of one proton. It has an rms radius of $a_0 = 2.58 \pm 0.04$ fm and an rms distance of $R_{\text{p}} = 4.73$ fm for the $^{7}_{4}\text{Be} + \text{p}$ system [79, 80]. The lifetime of the $^{8}_{5}$B against β^{+}-decay and fission is about $\tau_{\text{B}} \approx 769$ ms. By γ-ray absorption, it breaks up into beryllium via the following photonuclear reaction

$$\textit{Boron}: \quad {}^{8}_{5}\text{B} + \gamma \longrightarrow {}^{7}_{4}\text{Be} + \text{p}. \tag{2.12}$$

The lifetime of the $^{7}_{4}$Be is about $\tau_{\text{Be}} \approx 53.22$ days. It decays by electron capture with a decay energy of roughly 0.862 MeV or by γ-radiation with a decay energy of 0.477 MeV [61]. The binding energy, that holds the proton-halo in $^{8}_{5}$B to the nuclear-core is about $\mathcal{E}_b \approx 0.137$ MeV [81–83]. Note that the study of the cross sections for the reaction (2.12) is important for the understanding of some astrophysical processes, in particular the stellar nucleosynthesis [5, 6] and the solarboron-neutrino flux [84, 85].

So far we discussed some general properties of both stable and exotic nuclei, that would be necessary for the study of nuclear and hadronic processes when such objects interact with photons of sufficient energy. Our study is basically related to the investigation of the projectile-target interaction. When the target is a single proton or a halo-nucleus, the projectile, i.e. the photon, must have sufficient energy to exert an appreciable influence on it, i.e. above 5 MeV according to Eq. (2.5) and above 0.1 MeV according to Eq. (2.10). Values given by Eqs. (2.5) and (2.10) are typical energy scales in nuclear physics, and photons of such energies can

well be generated in the laboratories, as we shall show in Section 2.2. Through the interaction, interesting physical effects could happen due to the electromagnetic as well as the hadronic nature of the photon. Here we mention: the photoeffect both in its photoelectric and photonuclear forms, (nuclear) Compton scattering, lepton- and meson pair production. The interaction can also lead to nuclear excitations, transfer-, fission and fusion reactions.

When the photon energy reaches or exceeds the π-meson mass (corresponding to the γ-ray domain), the hadronic nature of photons appear and their interaction with the electric field of the charged target seem to be independent of the electric charge. These photons would mainly interact like massive particles, mesons, with the fundamental constituents of the target from quarks and gluons with the same quantum numbers as each photon, namely spin $S = 1$ and parity $P = -1$. Those mesons include the isoscalar-vector ω and the vector-isovector ρ mesons. In this energy regime, resonant photoproduction of neutral pseudoscalar mesons (pion, Kaon, η) can well occur. Such hadronic process is known as Primakoff effect [44, 86, 87], which takes place inside the hot plasma of stars powered by ultra-strong magnetic fields, where the strength is approximately equal to the Schwinger value $H_c = m_e^2/e = 0.862\ \text{MeV}^2 = 4.41 \times 10^9$ T.

2.1.3 Nuclear Models

Due to the complexity of strong interactions and the substructure of nucleons, the field of nuclear physics has later on emerged into various branches of physics. Among them we cite hadronic physics, whose degrees of freedom include baryons and mesons, and QCD, whose degrees of freedom include quarks and gluons. Hadronic physics ignore, so far at least, the high-energy processes occurring at the subnuclear level. However, the unified goal of theoretical hadronic physics with QCD is to develop mathematical models, that provide an accurate description of nuclear structure and dynamics over a wide range of energies, from the few hundreds of keV to the GeV regime, and this over a wide range of distances, from a small fraction of a femtometer (quark-gluon plasma phase) to a few femtometers.

In general, one tries to reproduce the experimental data as optimally as possible, and on the other hand, one tries to make qualitative and quantitative predictions on the physical behavior of the nuclear system, which are unknown so far. Because the formulation of the quantum mechanics and the relativity, different theoretical approaches have been developed, which can be divided into two different models:

- Microscopic models based on realistic hadron-hadron interaction, and
- Effective models based on a phenomenological parametrization of the interaction potentials.

Numerical solutions of realistic models, such as the [Dirac-] Brückner-Hartree-Fock theory, is very complicated, so they cannot be applied to nuclear systems of finite dimensions. Rather simple and successful approaches generally offer the phenomenological models, such as the [Skyrme-] Hartree-Fock (SHF) model, the effective global color model of QCD, the Nambu-Jona-Lasinio model, the relativistic ($\sigma - \omega$) mean field theory (RMF), etc. The latter model provides an accurate description of the nucleon-nucleon interaction at large distances but breaks down at short distances, because it treats baryons and mesons as elementary degrees of freedom and, of course, at short distances quarks and gluons manifest themselves. In contrast, the theory of elementary degrees of freedom of quarks and gluons, that is, QCD, is simple at short distances but complicated at large distances (in the confinement region). The attempt that allows a transition from QCD out into hadronic physics is known as "*hadronization*" which is, however, not solved so far.

Significant efforts have also been devoted to develop better models to reproduce the main halo properties (e.g., separation energies of the nucleon-halos, mean square radii, etc.) and to study their reaction mechanisms [88,89]. A Glauber model calculation has been successful to evaluate the reaction, interaction, and two-neutron removal cross sections of ^{11}Li [90, 91]. On the other hand, the phenomenological SHF model [89] with standard force parameters and the ($\sigma - \omega$) RMF [78,92] theory have been used to reproduce the one-proton separation energies and mean square radii of some halo-nuclei. Using relativistic Hartree-Bogoliubov theory, Meng and Ring [93] also found a good agreement with experimental values for the total binding energies and the radii of the isotope chain ^{6}Li to ^{11}Li.

Most of the effective hadronic models of nuclei use a Yukawa-type meson exchange potential to describe

the nuclear forces between nucleons. Thereby, pions and other mesons $(\sigma, \omega, \rho, \dots)$ are responsible for the binding of protons and neutrons. For example, the standard version of the $(\sigma - \omega)$ model has been developed to describe the exchange of σ and ω mesons between nucleons, which is known to provide the intermediate-range attraction and short-range repulsion in the nucleon-nucleon potential. The effective interaction is characterized by the meson parameters such as their masses and coupling constants, which are "*adjusted*" to reproduce the saturation properties of stable nuclei.

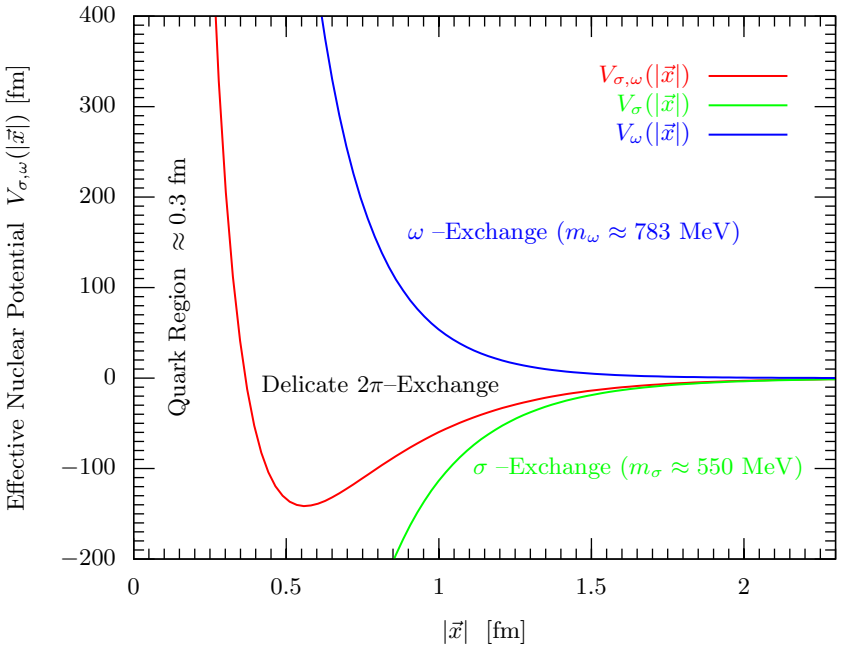

Figure 2.1: Effective nuclear potential in the $(\sigma - \omega)$ model illustrating short-range repulsion and intermediate-range attraction.

This interaction can be expressed phenomenologically for equal numbers of protons and neutrons in terms of two Yukawa potentials,

$$V_{\sigma,\omega}(|\vec{x}|) = V_\sigma(|\vec{x}|) + V_\omega(|\vec{x}|) = \left(-\frac{g_\sigma^2}{4\pi} \cdot \frac{e^{-m_\sigma|\vec{x}|}}{|\vec{x}|}\right) + \left(\frac{g_\omega^2}{4\pi} \cdot \frac{e^{-m_\omega|\vec{x}|}}{|\vec{x}|}\right), \tag{2.13}$$

where g_σ, g_ω, m_σ and m_ω are the coupling constants and masses of the σ and ω mesons, respectively, and $|\vec{x}|$ is the relative distance between two nucleons. The minus sign tells us that the σ meson potential is attractive. Moreover, the heavier (lighter) the exchanged meson is, the more rapidly (slowly) decreases the potential with increasing distance $|\vec{x}|$. Therefore, the range of the resulting interaction (2.13) is mostly determined by the masses of the exchanged σ and ω mesons and the strength by their coupling constants g_σ and g_ω as shown in Fig. 2.1. We shall use this meson exchange potential in the second project of our thesis (Chapter 5) to study the process of $\pi^+\pi^-$ pair production. This is one of the analogies we want to draw with field-induced processes known from atomic physics [45–47], where photon exchange (Coulomb) potential is used to study pair production of e^+e^- [94–101] and $\mu^+\mu^-$ [100, 102, 103].

2.2 Novel Radiation Sources

In the present thesis our target particle is first a pre-accelerated proton and second a halo-nucleus. Our projectile is a single or several photons of energy between 2 eV to 3 MeV using different kinds of radiation sources. In this context, we will deal with different problems associated with nuclear and hadronic processes in the interaction

between high-energy photons and matter at the hadronic level. In order to justify our motivation to carry out this work, we should have the right balance between the typical nuclear level spacings and energies discussed above, and the recent advances in the development of high-energy and high-intensity radiations. Let us then give a brief overview on the present status and future development of radiation sources.

2.2.1 Laser Sources

A laser source is characterised by its coherence, monochromaticity, directionality and high photon density. Since the invention of the first working laser in the early 1960's, the laser-based spectroscopic methods open further opportunities for the study of nuclear structures and properties. For example, in determining the nuclear charge radii of both stable and exotic nuclei via atomic transitions [104]. However, the use of lasers to induce high-energy reactions become especially apparent since the invention of the Chirped Pulse Amplification (CPA) technique by Strickland and Mourou in 1985 [105] for the amplification of ultrashort pulses to high energies. To date, it has been proven that nuclear and hadronic processes can be induced indirectly, when a petawatt laser (peak intensity above 10^{19} W/cm^2) is focused to dimensions of several microns and impinges on a solid-state target. In the resulting plasma wakefields, electrons can be accelerated to relativistic energies up to several 100 MeV and emit secondary bremstrahlung γ-rays. These have led to the observation of laser-induced nuclear fission [106, 107], proton or neutron emission [10–12], and efficient e^+e^- pair production through the Bethe-Heitler effect [14]. In 1999, Ditmire *et al.* [108] have observed the laser-driven inertial fusion from the explosions of deuterium clusters heated with a compact table-top laser. This fusion process is followed by the production of large amounts of neutrons.

A lot of large-scale petawatt and multiterawatt-class laser facilities exist around the world, or are in planning. One of them is the NOVA facility at the Lawrence Livermore National Laboratory in California. The produced 16 trillion watts of laser light can accelerate proton with energies up to 58 MeV [109], and heavier ions such as carbon, aluminium and lead with up to 7 MeV per nucleon [110]. The currently highest laser intensities in the world is about 10^{22} W/cm^2 [111] delivered by the Titanium-Sapphire laser at the Center for Ultrafast Optical Science (CUOS) at Michigan in the USA. This is followed by the VULCAN petawatt laser at the Rutherford Appleton Laboratory in the United Kingdom. Using the CPA technique on the Titanium-Sapphire laser, VULCAN operates at a wavelength of 800 nm and delivers pulses down to 30 fs, giving access to focused intensities of 10^{20} to 10^{21} W/cm^2. With such intensities, many isotopes have been produced and photofissions of ^{238}U and ^{232}Th was for the first time experimentally demonstrated [106, 107]. Some authors, such as Esirkepov *et al.* [112] showed with the help of relativistic Particle-in-Cell (PIC) simulations that at laser intensity of 10^{21} W/cm^2, proton and ions gain an energy as high as 1 GeV due to the Coulomb explosion.

Going further with high intensities and energies, Dubietis *et al.* [113] proposed in 1992 the optical parametric chirped-pulse amplification (OPCPA) for the generation of ultrashort pulses as a promising variant to CPA techniques. The OPCPA is a second-order nonlinear optical process which combines optical parametric amplification (OPA) and CPA technologies to amplify chirped pulses. In this combination, the photon energy and the momentum of an optical source (called the "*pump*") are converted into a new wave known as "*idler*" and an amplified signal that retains the linear chirp and spatial wavefront characteristics of a weak signal source (called the "*seed*"). The OPCPA has been adopted in some laser facilities around the world to achieve in the future very high energies and peak power intensities of 10^{26} to 10^{28} W/cm^2. Recent studies [114, 115] used the PIC simulations to show that the proton energy scales with laser intensity, which theoretically means that with these zetta- and exawatt-lasers, particles may be accelerated at energies up to 100 TeV. At such energy level, (which is not achievable at the Tevatron or even at the LHC, see the Introduction) the photon energy and the electric work performed by the laser field over a nuclear extension of a few femtometers are in the order of magnitude of the typical nuclear level spacing, so that direct laser-nucleus interactions involving giant resonance phenomena and structural changes of the nucleus, become relevant. The study of laser-nucleus interaction in such ultrarelativistic regime would also open up a completely new era of subnuclear physics, that could provide new opportunity for testing specific aspects of QCD, both in the perturbative and nonperturbative regimes, without a direct access to particles accelerators.

In addition to high intensities, also high frequencies laser exist around the world. In recent years, many physicists have started experiments with the aim of generating coherent and polarized x-rays such as the x-ray free electron laser (XFEL) at the Deutsches Elektronen-Synchrotron (DESY) in Hamburg. The XFEL uses the

principle of self-amplified spontaneous emission (SASE) to produce high laser frequencies about 0.1 keV. By the SASE-principle, small bunches of electrons is accelerated to high energies, causing the emission of coherent x-ray radiation from each electron, and each electromagnetic radiation interacts primarily with the nearest-neighbor electrons along the way. The total interaction leads to a "micro-arrangement" (or microbunching) of the electrons, which are so arranged that the spontaneously delivered radiation strengthens exponentially with the properties of high-frequency laser light. We note that the currently highest x-ray laser frequency in the world is about 1 keV, which is produced by the Linac Coherent Light Source (LCLS) at the SLAC National Accelerator Laboratory in Stanford, and in the future coherent laser frequencies up to 10 keV may be achieved. Coherent x-rays are also envisaged via high-order harmonics from oscillating plasma surfaces [116] or atomic gas jets [117]. Such compact and portable x-ray sources hold the potential to be operated in conjunction with the LHC proton beamline. Also efforts are undertaken to develop bursts of coherent γ-rays from an ensemble of long-lived excited (metastable) nuclei, called isomers. The process is known as Induced γ-Emission (IGE), which takes place when an external exitation, such as x-rays or accelerated charged particles, drives a fluorescent emission of γ-rays from isomers. This is quite analogous to conventional fluorescent emission of a photon by an excited electron in an atomic systems, so that quantum control techniques known from atomic physics (quantum electronics) can be transferred to nuclear physics (quantum nucleonics). The significant amounts of excitation energy that may be stored within nuclei over long periods of time, and are capable of being released as pure electromagnetic emission, may allow physicists to construct nuclear batteries or an ultimate coherent light source, the so-called γ-ray laser [118, 119].

2.2.2 Incoherent Radiations

Sources of incoherent radiation are also of increasing importance in nuclear researches. When a charged particle, usually an electron or proton, is accelerated it radiates photons in the form of electromagnetic waves by the mechanisms of bremsstrahlung and synchrotron emission [7, 8]. The emitted radiation has a continuous wavelengths spectrum, from the infrared to the γ-ray region, which becomes more intense and shifts toward higher frequencies by increasing the energy of the accelerated particle. Here we should make clear what we mean by incoherent radiations. First, when the decelerated particle produces electromagnetic waves with the same wavelength and same phase, so that the difference in phase between them remains constant, then the radiation is called coherent. For example, the XFEL source is partially coherent. In contrast, when the produced electromagnetic waves have different wavelengths and/or phases, the radiation is called incoherent.

In general, x-rays and γ-rays from particle accelerators are incoherent like the natural light, since the bunches containing a large numbers of charged particles circulating in the accelerator are longer than the wavelengths they are emitting. Incoherent radiations have been widely used in a variety of applications such as in nuclear medicine, radiography, and chemistry. Since the early 1930's, it's well known that incoherent γ-rays can induce nuclear reactions in nuclei, involving fission, fusion and photonuclear emission of neutrons, protons and deuterons. The photonuclear effect was investigated in detail by Wolfgang Gentner with his teacher Walther Bothe in 1937. They produced artificial radioisotopes using high-voltage equipment of 500 keV, enabling them to generate γ-rays of 17 MeV by bombarding ^{7}Li with protons [3]. These γ-rays made possible the first observation of the photonuclear effect in medium-heavy nuclei. However, at that time, it was not possible to generate γ-photons with energies larger than a few MeVs. More recently, modern particle accelerators provide a new, more efficient technique for generating high-energy γ-photons.

To date, incoherent radiations up to photon energies of about 20 GeV can be generated on earth via Compton backscattering or synchrotron emission from relativistic charged particles. The emitted γ-rays can well be detected in various laboratories using γ-spectroscopy detectors by the mechanisms of the photoeffect, Compton effect, and pair production. The first mechanism is preferred since all the energy of the incident γ-ray can be absorbed by the detector. For example, in the APOLLON- or in the HERMES experiment at the electron storage ring of the HERA accelerator at DESY, highly polarized γ-photons in the energy range between 10 and 20 GeV are generated by Compton backscattering of an ultraviolet laser beam, the so-called LCS, on a longitudinally polarized electron beam of 27.5 GeV energy [120]. Also polarized and tagged photon beam of a few GeV energy is generated at the GRAAL facility [39–41] by the same mechanisms, at the National Institute for Advanced Industrial Science and Technology (AIST) [121], at the MAMI Microtron [37, 38] and at the Jefferson Laboratory [42, 43]. One of the main goals of the GRAAL project (and also in the other facilities) in the

future is to detect ultra-energetic γ-rays above 20 GeV, which may provide a better understanding of various astrophysical phenomena related to the γ-ray bursts from collapsing stars and supernova explosions.

Thus, we can conclude this Chapter by saying that coherent and incoherent radiation sources may be generated by different techniques in modern laboratories. As a result, high-energy and high-intensity levels have already been achieved, and further increases and improvements in terms of coherence, monochromaticity and intensity are expected in the future. By comparing these photon energy levels with the nuclear excitation energies of nuclei as discussed in Section 2.1, we can easily say that these radiation sources can be used thoroughly for nuclear physics experiments and the experimental results could open up new theoretical studies of high-energy phenomena in the interaction between photons and matter from subnuclear particles, atoms, and molecules, to stars and galaxies.

–III–

Theoretical Methods

3.1 Strong-Field Approximation in Laser-Assisted Dynamics

We have mentioned above that a strong laser beam is characterised by its high photon density and monochromaticity, so that its depletion by emitting or absorbing photons from it is negligible. For these reasons, the laser field can be treated classically as an electromagnetic plane wave. Usually the strong laser field is characterised by its frequency ω_L and its electric field strength E_L. Its time dependent vector potential may be represented by the following linearly polarized or circularly polarized plane wave

$$\vec{A}_L = a\cos\left(\omega_L t - \vec{k}_L\vec{r}\right)\cdot\vec{e}_x + a\ \delta_0\ \sin\left(\omega_L t - \vec{k}_L\vec{r}\right)\cdot\vec{e}_y, \tag{3.1}$$

where $a = |-E_L/\omega_L|$ and $\vec{k}_L$ is the laser wave vector. The term $\delta_0 = 0$ stands for linear and $\delta_0 = \pm 1$ for circular polarization of the laser field. We work in the Coulomb gauge with div $\vec{A}_L = 0$ and vanishing scalar potential, $V_L = 0$.

The time-dependent Schrödinger equation, as well as the Klein-Gordon or the Dirac equation, of a free charged particle in an electromagnetic plane wave can be solved analytically, which are known as Volkov states [122]. These exact solutions have been used extensively by several authors to explore numerous QED processes such as Compton scattering, photoelectric effect and pair production. In general terms, the present study may be considered a first step towards an extension of the theory of laser-dressed QED into the realm of hadronic physics.

Notice that the use of Volkov wave function to describe particle in continuum state is denoted as "*Strong-Field Approximation*" because other interactions which might be present (such as the Coulomb forces) are assumed to be weaker than the strong laser field.

3.2 Volkov States

3.2.1 Nonrelativistic Volkov States

Let us consider a spinless particle of rest mass m, which carries an electric charge e and momentum $\vec{p}$ moving in the potential of a strong laser field. We assume the laser parameters ω_L and E_L, where the dynamics of the particle remains nonrelativistic. This means that the coupling parameter ξ between the laser field and the particle defined by

$$\xi = \frac{eE_L}{m\omega_L}, \tag{3.2}$$

will always be small, $\xi \ll 1$. Generally, values of $\omega_L \equiv |\vec{k}_L|$ are between 10^{-6} and 10^{-3} MeV, which correspond to wavelengths $\lambda_L \equiv 2\pi/\omega_L$ above 10^6 femtometer. Since λ_L is much larger than the relevant values of $|\vec{r}|$ of

few femtometers, and also much larger than the excursion length $\xi \cdot \lambda_L$ of the particle in the continuum, then we can approximate

$$\exp\left(i\ \vec{k}_L \cdot \vec{r}\right) = 1 + i\ \vec{k}_L \cdot \vec{r} + \cdots,$$

by its first term, unity. This is known as "*the dipole approximation*". Consequently, the term "propagation direction" of the laser field or any other formulation close to define a "laser wave vector, $\vec{p}_L \equiv \vec{k}_L$", has no definite meaning under this approximation. Hence, the vector potential can be written as

$$\vec{A}_L = a\cos(\omega_L t)\cdot\vec{e}_x + a\ \delta_0\ \sin(\omega_L t)\cdot\vec{e}_y. \tag{3.3}$$

In this Subsection we briefly discuss the nonrelativistic Volkov states. For a detailed discussion on this field, readers can refer to Ref. [122]. We first assume that our particle is a pointlike object and moving at nonrelativistic speed in the time-dependent potential (3.3) created by the laser field. The Hamiltonian governing the dynamics of the free particle is given by

$$H_0 = \frac{1}{2m}\ \left(\hat{p} - e\vec{A}_L(t)\right)^2 = \frac{\hat{p}^2}{2m} - e\ \hat{p}\ \vec{A}_L(t) + \frac{e^2 A_L(t)^2}{2m}, \tag{3.4}$$

where $\hat{p} \equiv -i\vec{\nabla}$ is its momentum operator, which corresponds to the spatial derivative $\vec{\nabla}$. The Schrödinger equation describing the evolution of the particle wave function $\psi(\vec{r},t)$ in the laser field is then

$$i\frac{d}{dt}\psi(\vec{r},t) = H_0\ \psi(\vec{r},t), \tag{3.5}$$

which may be solved analytically, and gives the so called Volkov wave function

$$\psi_p(\vec{r},t) = \frac{1}{\sqrt{V}}\exp\left[i\vec{p}\vec{r} - \frac{i}{2m}\int_0^t \left(\vec{p} - e\vec{A}_L(t')\right)^2 dt'\right]. \tag{3.6}$$

Here V is a normalization constant and the subscript "p" in $\psi_p(\vec{r},t)$ denotes the momentum of the particle, which means that to each p there corresponds a Volkov wave function. The nonrelativistic wave function (3.6) will be used in Chapter 4 to study the laser-assisted photonuclear effect in halo-nuclei.

3.2.2 Relativistic Gordon-Volkov States for Composite Particles

We now discuss a more complicated example of Volkov states. We consider a charged spinless particle with internal structure, for example a π-meson, and moving at relativistic speed in the following laser four-potential

$$A_L^\mu(k_L x) = a_1^\mu\cos(k_L x) + a_2^\mu\ \delta_0\ \sin(k_L x). \tag{3.7}$$

Here a_1^μ and a_2^μ are two constant four-vectors and $k_L \equiv k_L^\mu = (\omega_L, \vec{k}_L)$. The space-time four-vector and the four-momentum of the particle are denoted by $x \equiv x^\mu \equiv (t,\vec{x})$ and $p^\mu = (p^0,\vec{p})$, respectively. The free space-time evolution of the particle wave function $\phi(x)$ may be described by the following unperturbed covariant Lagrangian density up to second order in $F_{\mu\nu}$ [123]

$$\mathcal{L}_0 = (D_\mu\phi)^*\,(D^\nu\phi)\,[\delta_{\mu\nu} - \mathcal{K}_{\mu\nu}] - m^2\phi\phi^*. \tag{3.8}$$

Here $D^\mu = \partial^\mu + ieA_L^\mu$ denotes the gauge covariant derivative with respect to the laser field, where $\partial^\mu = \partial/\partial x_\mu$ and $\delta_{\mu\nu}$ is the Kronecker symbol. All terms in Eq. (3.8) multiplied by the Kronecker symbol contribute to the usual Lagrangian density for a pointlike spinless particle in an external electromagnetic field. The internal structure of our relativistic particle is taken into account by including its electric and magnetic polarizabilities λ_e and λ_m, which may be expressed by the following symmetric contribution

$$\mathcal{K}_{\mu\nu} = \frac{\lambda_e + \lambda_m}{m_\pi}F_{\mu\alpha}F_{\nu\alpha}, \tag{3.9}$$

where $F^{\mu\nu} = \partial^\mu A_L^\nu - \partial^\nu A_L^\mu$ is the antisymmetric strength tensor of the external electromagnetic field of the laser. We note that the electromagnetic polarizabilities are fundamental low-energy characteristics of the strong

hadronic interactions. They are a measure for the strength of the induced electric dipole moment $\vec{\mathcal{P}}_L = \lambda_e \cdot \vec{E}_L$ and the induced magnetic moment $\vec{\mathcal{M}}_L = \lambda_m \cdot \vec{B}_L$ of the charged particle by the external laser field.

The field theory of $\mathcal{L}_0$ in Eq. (3.8), which contains the electromagnetic coupling of the charged particle to the laser field, can be solved exactly[1]. Namely, we use the Hamilton's principle of least action with respect to $\phi(x)$ (i.e. the Euler-Lagrange equation)

$$\frac{\partial \mathcal{L}_0}{\partial \phi(x)} - \partial_\mu \frac{\partial \mathcal{L}_0}{\partial\left(\partial_\mu \phi(x)\right)} = 0, \tag{3.10}$$

to obtain from $\mathcal{L}_0$ the equation of motion of the relativistic particle. So, using Eq. (3.10) with respect to the complex conjugate of $\phi(x)$, we have

$$\begin{aligned}
&\frac{\partial \mathcal{L}_0}{\partial \phi^*(x)} = \left(-ieA_\mu \partial_\nu \phi(x) + e^2 A_\mu A_\nu \phi(x)\right)\left[\delta_{\mu\nu} - \mathcal{K}_{\mu\nu}\right] - m^2\phi(x). \\
&\frac{\partial \mathcal{L}_0}{\partial\left(\partial_\mu \phi^*(x)\right)} = \left(\partial_\nu \phi(x) + ieA_\nu \phi(x)\right)\left[\delta_{\mu\nu} - \mathcal{K}_{\mu\nu}\right]. \\
\Longleftrightarrow\ & \partial_\mu \frac{\partial \mathcal{L}_0}{\partial\left(\partial_\mu \phi^*(x)\right)} - \frac{\partial \mathcal{L}_0}{\partial \phi^*(x)} = \\
& \left[\partial_\mu \partial_\nu + ie\partial_\mu A_\nu + ieA_\mu \partial_\nu - e^2 A_\mu A_\nu\right]\left[\delta_{\mu\nu} - \mathcal{K}_{\mu\nu}\right]\phi(x) + m^2\phi(x) = 0 \\
\Longleftrightarrow\ & \left(\partial_\mu + ieA_\mu\right)\left(\partial_\nu + ieA_\nu\right)\left[\delta_{\mu\nu} - \mathcal{K}_{\mu\nu}\right]\phi(x) + m^2\phi(x) = 0 \\
\\
\Longleftrightarrow\ & D_\mu D^\mu \phi(x) - D_\mu\left[\mathcal{K}_{\mu\nu}\left(D_\nu \phi(x)\right)\right] + m^2\phi(x) = 0.
\end{aligned} \tag{3.11}$$

For a pointlike boson, we have $\lambda_e = \lambda_m = 0 \Longrightarrow \mathcal{K}_{\mu\nu} = 0$, and then we arrive at the following known expression for the Klein-Gordon equation

$$(D^2 + m^2)\phi(x) = 0.$$

Eq. (3.11) is thus a generalization of the Klein-Gordon equation for composite spin-zero particle interacting with an external electromagnetic field. We now require that the four-potential[2] (3.7) satisfies the Lorentz gauge condition with respect to the phase variable $\eta = k_\mu x^\mu$

$$\partial_\mu A^\mu(\eta) = \frac{d\left(A^\mu(\eta)\right)}{dx^\mu} = k_\mu \frac{d\left(A^\mu(\eta)\right)}{d\eta} = \frac{d\left(k_\mu A^\mu(\eta)\right)}{d\eta} = 0 \quad \Longrightarrow k_\mu A^\mu(\eta) = const. = 0,$$

and as a boundary condition we suppose that its switch-on is adiabatic in space and time, $\lim\limits_{x\to\pm\infty} A^\mu(\eta) = 0$.

Taking these approximations into account, we can start to derive from Eq. (3.11) the relativistic Gordon-Volkov wave function for a composite spinless particle. To simplify the notations, we shall put $\phi \equiv \phi^-(t, \vec{x})$, and after expanding Eq. (3.11), we write it as follows $\mathcal{H} = \mathcal{E} - \mathcal{F}$, where

$$\mathcal{E} = D_\mu D^\mu \phi + m^2\phi \quad \text{and} \quad \mathcal{F} = D_\mu\left[\mathcal{K}_{\mu\nu}\left(D_\nu\right)\right]\phi.$$

First we have

$$\begin{aligned}
\mathcal{E} &= \left(\partial_\mu + ieA_\mu\right)\left(\partial^\mu + ieA^\mu\right)\phi + m^2\phi \\
&= \left[\partial_\mu\partial^\mu + ie\partial_\mu A^\mu + ieA_\mu\partial^\mu - e^2 A_\mu A^\mu + m^2\right]\phi \\
&= \partial_\mu\partial^\mu\phi + ie\left[\partial_\mu\left(A^\mu\phi\right) + A_\mu\partial^\mu\phi\right] - e^2A^2\phi + m^2\phi \\
&= \partial_\mu\partial^\mu\phi + ie\left[\underbrace{\partial_\mu A^\mu}_{=0}\cdot\phi + A^\mu\partial_\mu\phi + A_\mu\partial^\mu\phi\right] + m^2\phi - e^2A^2\phi \\
&= \partial_\mu\partial^\mu\phi + 2ieA^\mu\partial_\mu\phi - e^2A^2\phi + m^2\phi,
\end{aligned} \tag{3.12}$$

[1] The calculations can also be found in Ref. [123].

[2] To simplify the notations, we leave out the subscript L from the laser vector potential ($A^\mu_L \to A^\mu$).

and second

$$\begin{aligned}\mathcal{F} &= (\partial_\mu + ieA_\mu)\left[\mathcal{K}_{\mu\nu}\left(\partial_\nu\phi + ieA_\nu\phi\right)\right] \\ &= ieA_\mu\mathcal{K}_{\mu\nu}\left(\partial_\nu + ieA_\nu\right)\phi + \partial_\mu\mathcal{K}_{\mu\nu}\left(\partial_\nu + ieA_\nu\right)\phi \\ &= \mathcal{K}_{\mu\nu}\left(ieA_\mu\partial_\nu - e^2A_\mu A_\nu\right)\phi + \left(\partial_\mu\mathcal{K}_{\mu\nu}\right)\cdot\left(\partial_\nu + ieA_\nu\right)\phi + \mathcal{K}_{\mu\nu}\left(\partial_\mu\partial_\nu + ie\partial_\mu A_\nu\right)\phi \\ &= \mathcal{K}_{\mu\nu}\left(\partial_\mu\partial_\nu + 2ieA_\mu\partial_\nu + ie(\partial_\mu A_\nu) - e^2A_\mu A_\nu\right)\phi + \left(\partial_\mu\mathcal{K}_{\mu\nu}\right)\cdot\left(\partial_\nu + ieA_\nu\right)\phi. \end{aligned} \tag{3.13}$$

In order to find an expression for the symmetric tensor $\mathcal{K}_{\mu\nu}$ given by Eq. (3.9), we use again the Lorentz gauge condition: $\partial_i A^i(\eta) = k_i A^i(\eta) = 0$ with $\eta = k_i x^i$, $\forall\ i = \mu,\nu,\alpha$. Furthermore, the electromagnetic four-potential of the laser described by Eq. (3.7) corresponds to a circularly or linearly polarized plane wave, so that both the electric and magnetic field vectors, $\vec{E}_L$ and $\vec{B}_L$, are perpendicular to the wave vector $\vec{k}_L$ and we have $\|\vec{E}_L\| = \|\vec{B}_L\|$ (for more details, see Appendix B.4). Thus we have $F_{\mu\nu}F^{\mu\nu} = 0$, and then we obtain

$$\begin{aligned}\mathcal{K}_{\mu\nu} &= \frac{\lambda_e + \lambda_m}{m}F_{\mu\alpha}F_{\nu\alpha} \\ &= \frac{\lambda_e + \lambda_m}{m}\left(\partial_\mu A_\alpha - \underbrace{\partial_\alpha A_\mu}_{=0}\right)\left(\partial_\nu A_\alpha - \underbrace{\partial_\alpha A_\nu}_{=0}\right) \\ &= \frac{\lambda_e + \lambda_m}{m}\left(\partial_\mu A_\alpha\partial_\nu A_\alpha\right) \\ &= \frac{\lambda_e + \lambda_m}{m}\cdot k_\mu\frac{\partial A_\alpha}{\partial\eta}\cdot k_\nu\frac{\partial A_\alpha}{\partial\eta}. \end{aligned} \tag{3.14}$$

This result means that all terms in the upper expression of $\mathcal{F}$ containing A_μ and A_ν will vanish as well. That is,

$$\mathcal{F} = \frac{\lambda_e + \lambda_m}{m}\cdot k_\mu k_\nu\left(\frac{\partial A_\alpha}{\partial\eta}\right)^2\partial_\mu\partial_\nu\phi,$$

and then we arrive at

$$\mathcal{H} = \partial_\mu\partial^\mu\phi + 2ieA^\mu\partial_\mu\phi - e^2A^2\phi + m^2\phi - \frac{\lambda_e + \lambda_m}{m}\cdot k_\mu k_\nu\left(\frac{\partial A_\alpha}{\partial\eta}\right)^2\partial_\mu\partial_\nu\phi = 0. \tag{3.15}$$

We look now for solutions of the differential equation (3.15) in the form $\phi(x) = e^{i(px)}F(\eta)$. For our physical particles corresponding to plane wave photons ($k^2 = k^ik_i = 0$ with $i = \mu,\nu$) and to a real boson ($p^2 = m^2$) we have

$$\partial^\mu\phi(x) = ip^\mu e^{-i(px)}F(\eta) + e^{-i(px)}\cdot\frac{dF(\eta)}{d\eta}k^\mu,$$

$$\partial^\mu\partial_\mu\phi(x) = -p^2e^{i(px)}F(\eta) + 2i(kp)e^{i(px)}\frac{dF(\eta)}{d\eta} + \underbrace{k^2}_{=0}e^{i(px)}\frac{d^2F(\eta)}{d\eta^2},$$

$$\partial_\mu\partial_\nu\phi(x) = -p_\nu p_\mu e^{i(px)}F(\eta) + ip_\nu e^{i(px)}\frac{dF(\eta)}{d\eta}k_\mu + ip_\mu e^{i(px)}\frac{dF(\eta)}{d\eta}k_\nu + e^{i(px)}\frac{d^2F(\eta)}{d\eta^2}k_\nu k_\mu.$$

Inserting these three expressions in (3.15) yields

$$
\begin{aligned}
&-p^2F(\eta)+2i(kp)\frac{dF(\eta)}{d\eta}+2ieA_\mu\left(ip^\mu F(\eta)+k^\mu\frac{dF(\eta)}{d\eta}\right)+m^2F(\eta)-e^2A^2F(\eta)-\\
&\frac{\lambda_e+\lambda_m}{m}k_\mu k_\nu\left(\frac{\partial A_\alpha}{\partial\eta}\right)^2\left(-p^\nu p^\mu F(\eta)+ip^\nu k^\mu\frac{dF(\eta)}{d\eta}+ip^\mu k^\nu\frac{dF(\eta)}{d\eta}+k^\nu k^\mu\frac{d^2F(\eta)}{d\eta^2}\right)=0\\
&\iff\ \frac{dF(\eta)}{F(\eta)}=-i\left[\frac{e(pA)}{(kp)}+\frac{e^2A^2}{2(kp)}-\frac{\lambda_e+\lambda_m}{2m}(kp)\left(\frac{\partial A_\alpha}{\partial\eta}\right)^2\right]d\widetilde{\eta}\\
&\iff\ F(\eta)=F(\eta\to0)\cdot\exp\left[-i\int_{-\infty}^{kx}\left(\frac{e(pA)}{(kp)}+\frac{e^2A^2}{2(kp)}-\frac{\lambda_e+\lambda_m}{2m}(kp)\left(\frac{\partial A_\alpha}{\partial\eta}\right)^2\right)d\widetilde{\eta}\right]\\
&\iff\ \phi(x)=N\cdot\exp\left[i(px)-i\int_{-\infty}^{kx}\left(\frac{e(pA)}{(kp)}+\frac{e^2A^2}{2(kp)}-\frac{\lambda_e+\lambda_m}{2m}(kp)\left(\frac{\partial A_\alpha}{\partial\eta}\right)^2\right)d\widetilde{\eta}\right].
\end{aligned}
\tag{3.16}
$$

We now calculate for this wave function the corresponding current density to obtain the proper normalization constant $N=F(\eta\to-\infty)$. We have

$$
\begin{aligned}
j_\mu(x)&\equiv-i\left(\frac{\partial\mathcal{L}}{\partial\left(\partial_\mu\phi\right)}\phi-\frac{\partial\mathcal{L}}{\partial\left(\partial_\mu\phi^*\right)}\phi^*\right)\\
&=\frac{1}{i}\left[\left(D_\nu^+\phi^*\right)\phi-\left(D_\nu\phi\right)\phi^*\right]\left[\mathcal{K}_{\mu\nu}-\delta_{\mu\nu}\right]\\
&=\frac{1}{i}\left[(\partial_\nu\phi^*)\phi-ieA_\nu\phi^*\phi-(\partial_\nu\phi)\phi^*-ieA_\nu\phi\phi^*\right]\left[\mathcal{K}_{\mu\nu}-\delta_{\mu\nu}\right]\\
&=\frac{1}{i}\left[(\partial_\nu\phi^*)\phi-(\partial_\nu\phi)\phi^*-2ieA_\nu\right]\left[\mathcal{K}_{\mu\nu}-\delta_{\mu\nu}\right]\\
&=\frac{N^2}{i}\left\{\left[-ip_\nu+ik_\nu\left(\frac{e(pA)}{(kp)}+\frac{e^2A^2}{2(kp)}-\frac{\lambda_e+\lambda_m}{2m}(kp)\left(\frac{\partial A_\alpha}{\partial\eta}\right)^2\right)\right]-\right.\\
&\left.\left[ip_\nu-ik_\nu\left(\frac{e(pA)}{(kp)}+\frac{e^2A^2}{2(kp)}-\frac{\lambda_e+\lambda_m}{2m}(kp)\left(\frac{\partial A_\alpha}{\partial\eta}\right)^2\right)\right]-2ieA_\nu\right\}\left[\mathcal{K}_{\mu\nu}-\delta_{\mu\nu}\right]\cdot e^0
\end{aligned}
$$

$$
\iff j_\mu(x)=2N^2\left[p_\mu+eA_\mu-\left(\frac{e(pA)}{(kp)}+\frac{e^2A^2}{2(kp)}-\frac{\lambda_e+\lambda_m}{2m}(kp)\left(\frac{\partial A_\alpha}{\partial\eta}\right)^2\right)k_\mu\right]
\tag{3.17}
$$

The electromagnetic potential $A\equiv A_L^\mu(kx)$ is a periodic function, so that the mean value of $j_\mu(x)$ gives

$$
\overline{j_\mu(x)}=2N^2\left[p^\mu-\left(\frac{e^2\overline{A_L^2}}{2(kp)}-\frac{\lambda_e+\lambda_m}{2m}(kp)\overline{\left(\frac{\partial A_\alpha}{\partial\eta}\right)^2}\right)k^\mu\right],\quad\text{because}\quad\overline{A_L^\mu(kx)}=0.
$$

On the other hand, we have

$$
A_L^2(\eta)=-a^2\cos^2\eta-a^2\delta_0^2\sin^2\eta\ \implies\ \overline{A_L^2}:=-\frac{a^2}{\pi}\int_0^\pi\cos^2\eta d\eta-\frac{a^2\delta_0^2}{\pi}\int_{-\pi/2}^{\pi/2}\sin^2\eta d\eta=-\frac{a^2}{2}(1+\delta_0^2).
$$

We define

$$
q^\mu\overset{\text{def}}{=}p^\mu-\left(\frac{e^2\overline{A_L^2}}{2(kp)}-\frac{\lambda_e+\lambda_m}{2m}(kp)\overline{\left(\frac{\partial A_\alpha}{\partial\eta}\right)^2}\right)k^\mu=p^\mu+\frac{a^2}{4(kp)}\left(e^2-\frac{\lambda_e+\lambda_m}{m}(kp)^2\right)(1+\delta_0^2)k^\mu,
$$

as an *effective* momentum of the spin-zero particle in the electromagnetic field of the laser. Taking into account that $k^2 = 0$ and $p^2 = m^2$, we get

$$q^2 \overset{\text{def}}{=} m^{*2} = q^\mu q_\mu = m^2 - \left(\frac{e^2 \overline{A_L^2}}{2(kp)} - \frac{\lambda_e + \lambda_m}{2m}(kp) \overline{\left(\frac{\partial A_\alpha}{\partial \eta} \right)^2} \right) \cdot 2(kp) = m^2(1 + \xi^2),$$

where

$$\xi \overset{\text{def}}{=} \sqrt{ - \left(\frac{e^2 \overline{A_L^2}}{m^2} - \frac{\lambda_e + \lambda_m}{m^3}(kp)^2 \overline{\left(\frac{\partial A_\alpha}{\partial \eta} \right)^2} \right)} = \frac{a}{m\sqrt{2}} \cdot \sqrt{ \left(e^2 - \frac{\lambda_e + \lambda_m}{m}(kp)^2 \right)(1 + \delta_0^2)},$$

denotes an *effective* electromagnetic intensity parameter related to an effective mass $m^* = m\sqrt{1 + \xi^2}$ of the particle. Thus we can write

$$\overline{j_\mu} = 2N^2 q^\mu.$$

In order to determine the normalization constant N, we can consider the time component of the averaged current density $\overline{j_0}$ as the probability to find our particle wave function inside an infinitesimal volume $dV = d^3\vec{x}$, that is

$$P \overset{!}{=} 1 = \int_{\text{space volume V}} d^3\vec{x}\, \overline{j_0} \quad \Longleftrightarrow \quad 1 = 2VN^2 q^0 \quad \Longleftrightarrow \quad \boxed{N = \frac{1}{\sqrt{2Vq^0}}}.$$

Finally, if we consider ϕ to be normalized in a box having a large (but finite) volume $V = L^3$, then we obtain

$$\phi(x) = \frac{1}{\sqrt{2Vq^0}} \cdot \exp\left[i(px) - i \int_{-\infty}^{kx} \left(\frac{e(pA)}{(kp)} + \frac{e^2 A^2}{2(kp)} - \frac{\lambda_e + \lambda_m}{2m}(kp) \left(\frac{\partial A_\alpha}{\partial \eta} \right)^2 \right) d\widetilde{\eta} \right], \tag{3.18}$$

which corresponds to the wave function for a composite spin-zero particle of charge e in the external laser field. The corresponding antiparticle wave function can easily be obtained by making the substitution: $p \longleftrightarrow -p$. The relativistic wave function (3.18) will be used later in Chapter 5 to study the multiphoto-production of charged pion pairs in proton-laser collision.

3.2.3 Relativistic Gordon-Volkov States for Pointlike Particles

A relativistic Gordon-Volkov wave function for pointlike and spin-zero particle may easily be obtained from the previous derivations just by setting $\lambda_e = \lambda_m = 0 \Longrightarrow \mathcal{K}_{\mu\nu} = 0$, and hence we arrive at

$$\phi(x) = \frac{1}{\sqrt{2Vq^0}} \cdot \exp\left[i(px) - i \int_{-\infty}^{kx} \left(\frac{e(pA)}{(kp)} + \frac{e^2 A^2}{2(kp)} \right) d\widetilde{\eta} \right]. \tag{3.19}$$

–IV–

Laser-Assisted Photonuclear Effect in Halo-Nuclei

In the present Chapter we start our theoretical study of nuclear processes in intense light-matter interaction with the laser-assisted photonuclear effect in exotic 'halo' nuclei. While the photoelectric effect can knock out electrons from the atom, the photonuclear effect can knock out hadrons from the nucleus. The principle is the same, but the energy scales and the physical processes involved in both reactions are not. In particular, we focus on one-proton-halo-nuclei like ^{8}B, because the proton can be affected by the electromagnetic forces. To the best of our knowledge, there are no theoretical studies on nuclear processes involved in the interaction of high-power electromagnetic radiations with halo-nuclei, but there are many reasons which have led us to make this study, which will be discussed in the Outlook of this work.

4.1 Historical Background

The research field of the photonuclear effect was opened with the experiments by Chadwick and Goldhaber on the photodisintegration of the deuteron where γ-rays from a radioactive source were utilized [2]. In 1934, they measured the active cross section of the following (γ, n) reactions

$$\textit{Deuteron}: \quad {}^{2}_{1}\mathrm{H} + \gamma \longrightarrow {}^{1}_{1}\mathrm{p} + {}^{1}_{0}\,\mathrm{n}, \tag{4.1a}$$

$$\textit{Beryllium}: \quad {}^{9}_{4}\mathrm{Be} + \gamma \longrightarrow {}^{8}_{4}\mathrm{Be} + {}^{1}_{0}\,\mathrm{n}, \tag{4.1b}$$

which was found to be $\sigma \approx 2 - 5 \times 10^{-26}$ cm^2 $= 20 - 50$ millibarn at a γ-photon energy of 2.62 MeV [2]. Systematic investigations of the photonuclear effect were carried out since the early 1930's by Bothe and Gentner in Heidelberg which relied on high-energy γ-rays produced with the aid of a proton accelerator. Inspired by the experiments of Chadwick and Goldhaber, Bothe and Gentner published in 1938 on the energy dependence of the photonuclear effect, which was the first clear evidence that photonuclear absorption spectra are accumulative and continuous, a phenomenon later known as the nuclear giant dipole resonance [4]. From 1934 to 1957, Bothe supervised various research activities on the photonuclear effect, which have been initiated at the Kaiser-Wilhelm/Max-Planck-Institute for Medical Researches. One year after his death, this institute became the Max Planck Institute for Nuclear Physics and its main building was later named Bothe laboratory. Ever since then, Bothe's students succeeded in investigating photonuclear reactions in further elements, such as

$$\textit{Sulphur}: \quad {}^{32}_{16}\mathrm{S} + \gamma \longrightarrow {}^{31}_{16}\mathrm{S} + {}^{1}_{0}\,\mathrm{n},$$

$$\textit{Aluminum}: \quad {}^{27}_{13}\mathrm{Al} + \gamma \longrightarrow {}^{26}_{13}\mathrm{Al} + {}^{1}_{0}\,\mathrm{n},$$

$$\textit{Copper}: \quad {}^{63}_{29}\mathrm{Cu} + \gamma \longrightarrow {}^{62}_{29}\mathrm{Cu} + {}^{1}_{0}\,\mathrm{n}.$$

Up to date, the (γ, n) reactions have been more investigated by several authors (see, e.g., [124] and recently [125, 126]). Furthermore, (γ, p), (γ, d) and (γ, α) reactions involving the photoemission of protons,

deuterons and α-particles have also been reported [127–129], where high energy photons from synchrotron and electron bremsstrahlung sources with end point energies ranging from 22 to 30 MeV were utilized. Recent studies show that (γ, p) reactions are playing an important role in the synthesis of proton-rich nuclei [130, 131], and hence for our understanding of stellar nucleosynthesis and galactic chemical evolution. However, no experimental studies of the photonuclear effect in halo-nuclei were carried out so far, which may be performed in the laboratory, and also there are no theoretical treatments of this process. This is what we shall try to do in the next lines of the present Chapter.

By a direct laser-induced photonuclear reaction in halo-nuclei, the pulse duration of the laser should be shorter than the lifetime of the halo-nucleus we want to study. Furthermore the laser photon energy should be higher than the binding energy of the nucleon-halo. The first condition is fulfilled by using, for example, the VULCAN (~ 30 fs) or the XFEL (~ 100 fs) type laser. But the second condition is not, when the halo-nucleus is initially considered in a stationary state. In what follows we will show how we can solve this problem, but we first give several estimates and orders of magnitude.

4.2 Motivations

We consider a one-proton-halo-nucleus ${}^{A}_{Z}[\mathrm{Xp}]$, which initially is in a stationary state and exposed to a laser beam of frequency ω_L and electric field strength E_L. Since the proton can be affected by the electromagnetic forces, an appreciable influence on it depends mainly on ω_L and/or E_L. At low frequency where the radiation wavelength $\lambda_L = 2\pi/\omega_L$ is much larger than the rms matter radius R_{p}, the proton oscillates linearly back and forth, at the same frequency ω_L as the laser field itself. However, at high energy interesting physical effects could happen, if one of the following conditions is fulfilled (, or both of them):

(i) The work done by the electric field on the (weakly bound) proton over the rms matter radius R_{p} approaches the nuclear binding energy, $\mathcal{E}_b \simeq eE_L R_{\mathrm{p}}$.

(ii) The laser frequency is greater than or equal to the nuclear binding energy, $\omega_L \gtrsim \mathcal{E}_b$.

In the second case, the proton would be well ejected from the core via the photonuclear effect with the kinetic energy $E_{kin} = E_{ph} - E_{\mathrm{core}} - \mathcal{E}_b$, where $E_{ph} = \omega_L$ (or $E_{ph} = n\omega_L$ in the multiphoton case) is the initial energy of the laser photons, and E_{core} the kinetic energy of the recoiling nuclear-core. This principle of energy conservation shows that the velocity of the proton is mainly affected by the photon energy of the laser radiation. The first condition may be viewed as a semiclassical limit of the laser, while the second one is a quantum mechanical process by which the proton-halo escapes from the nuclear-core by simultaneously absorbing one or several photons.
Our first aim here is to remove the proton directly from the halo-nucleus via the photonuclear reaction. So theoretically we need to fulfil the condition (i) and/or (ii). For (i), taking $R_{\mathrm{p}} = 4.73$ fm and $\mathcal{E}_b = 0.137$ MeV (for Boron-8), we obtain $E_L \gtrsim 2.89 \times 10^{17}$ V/cm, which corresponds to a laser intensity of 1.1×10^{32} W/cm^2. Such intensity exceeds the Schwinger critical value of roughly 4.6×10^{29} W/cm^2, and thus cannot be achieved for either current or near future laser source technologies. Also the second condition cannot be fulfilled even with the currently highest frequencies of 1 keV from the LCLS machines [132, 133]. Thus, it is not possible to generate directly a laser induced photoproton reaction from halo-nuclei, and of course from stable ones, since the vast majority of them have an average binding energy above 100 keV per nucleon, as given by Eqs. (2.10) and (2.5) in Section 2.1.

However, inspired from the discussion in Chapter 2, our first aim can well be realised when the weakly bound proton interacts with a combined field consisting of a strong laser pulses and a γ-ray photon of frequency ω' above the nuclear binding energy $\mathcal{E}_b$ ($\omega' \gtrsim 0.137$ MeV), i.e. according to the following (γ, p) reaction scheme

$$ {}^{A}_{Z}[\mathrm{Xp}] + \omega' + n\omega_L \quad \longrightarrow \quad {}^{A-1}_{Z-1}[\mathrm{X}] + {}^{1}_{1}\,\mathrm{p}. \tag{4.2} $$

Obviously, the use of the γ-ray photon in the absence of the laser is enough to remove the proton-halo via a photonuclear reaction. But one of the motivations behind our attempt is to look if the assisting laser field can modify the properties of the photonuclear effect in a characteristic way, and if this would be the case, then we might have to recognize which conclusions and lessons can be drawn from the results of our study.

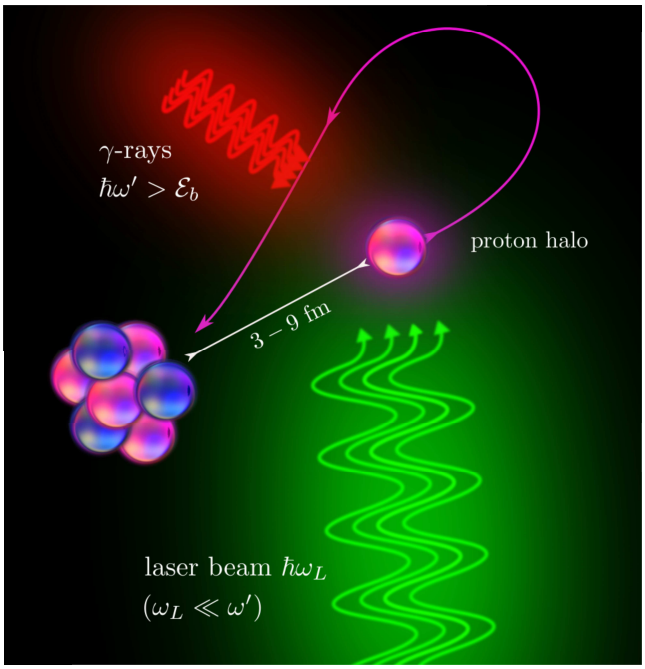

Figure 4.1: An illustration of the process of using a combined field consisting of a strong optical laser (green) and a hard x-ray or a γ-ray (red) photon to induce a photoproton emission from an exotic 'halo' nucleus.

After simultaneous interaction with both radiation fields, the proton-halo is first emitted through the photonuclear effect and its trajectory is influenced afterwards by the strong laser field. Thus, we may expect that the laser will serve as an accelerator or eventually inhibitor (retarder) of the photoproton, whereby its mean kinetic energy changes with increasing intensity and/or decreasing frequency of the laser. The process described by Eq. (4.2) is illustrated in Figure 4.1.

The present Chapter is organized as follows: In the theoretical framework, Sec 4.3, we calculate the differential and total cross sections for the laser-assisted reaction (4.2) by using the theoretical methods described in Chapter 3, and also by introducing and discussing various approximation levels which characterize the process. Afterward, we discuss in Section 4.4 the theoretical results at different input parameters, field geometries and polarizations of the laser wave and of the γ-radiation.

4.3 Theoretical Framework

The wave function describing the proton-halo of nuclear binding energy $-\mathcal{E}_b$ and mass m_p, which initially is in a stationary state, may be approximated by

$$\psi_0(\vec{r},t) = \psi_0(\vec{r}) \cdot \exp\left(i\mathcal{E}_b t\right), \tag{4.3a}$$

with [134]

$$\psi_0(\vec{r}) = \frac{c_0}{\sqrt{4\pi}} \left(1 - \left(\frac{|\vec{r}|}{a_0}\right)^2\right) \exp\left(-\frac{|\vec{r}|}{r_0}\right). \tag{4.3b}$$

Here the spin-orbit coupling between the proton-halo and nuclear-core is neglected due to the large scale structure of the halo-nucleus. We also neglect the kinetic energy of the recoiling nuclear-core, E_core, due to its higher rest mass-energy. The above approximation of the radial wave function (4.3b) is not unique, but using Hartree-Fock calculations [89] it appears to be adequate for describing the main halo properties (e.g., the mean square radii, binding energies).

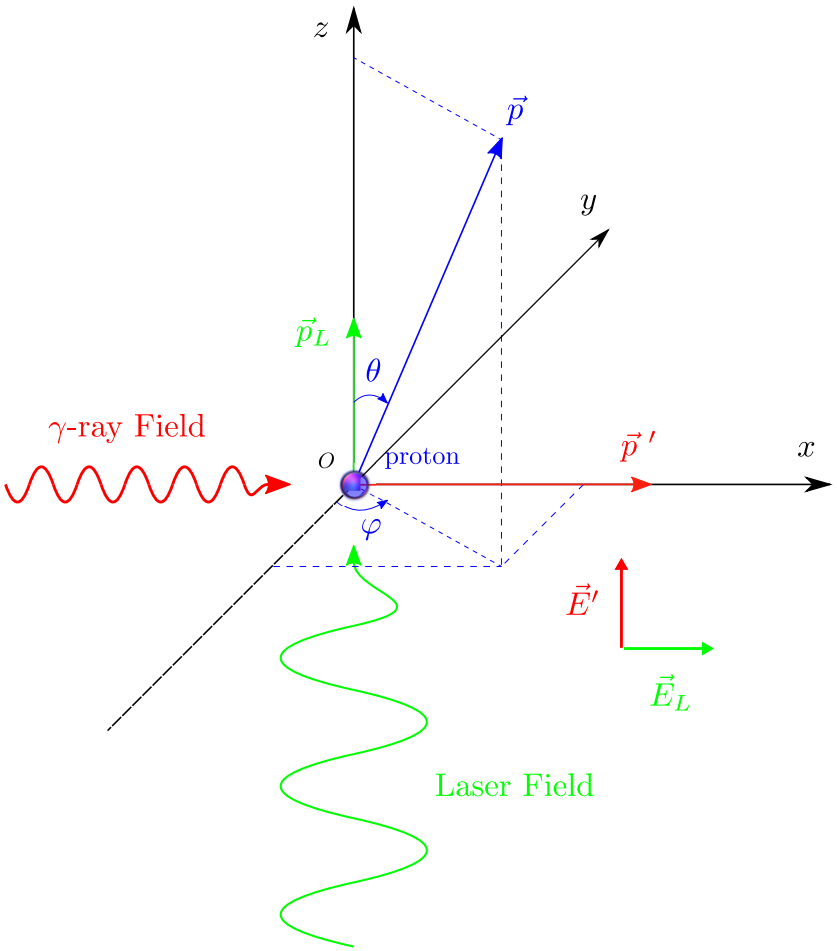

Figure 4.2: Schematic diagram of the laser-assisted photonuclear effect. The electric field strengths of the laser wave and the γ-photon are perpendicular to each other, $\vec{E}_L \perp \vec{E}'$.

Throughout, we denote by $\vec{r}$ the position of the proton-halo measured back from the center of mass of the daughter nucleus. Notice that relevant values of $|\vec{r}|$ correspond to the range of the, let's say, "*nuclear-halo potential*" ($\sim 1 - 9$ fm), where the exchange of photons takes place. We suppose that the initial quantities a_0, r_0 and $\mathcal{E}_b$ define thoroughly the one-proton-halo isotope ${}^{A}_{Z}$[Xp], which are phenomenological fit parameters to experimental values of the mean square radius, density distribution and one-proton separation energy. The constant c_0 can easily be calculated by the normalization condition

$$\int d^3\vec{r}\,\langle\psi_0|\psi_0\rangle = 4\pi \int_0^{+\infty} d|\vec{r}|\; r^2\psi_0(\vec{r})^2 \stackrel{!}{=} 1,$$

which yields

$$c_0 = \left(\frac{2}{r_0}\right)^{3/2} \frac{a_0^2}{\sqrt{45r_0^4 + 2a_0^4 - 12(a_0 r_0)^2}}.$$

Input Parameters	Values
Proton rest mass	$m_{\rm p} = 938.272$ MeV
Binding energy of the proton-halo	$\mathcal{E}_b = 0.137$ MeV
Mean square radius of the proton-halo	$a_0 = 2.58$ fm
Density distribution of the proton-halo	$r_0 = 1.45$ fm

Table 4.1: The input parameters that will be used later for the numerical calculations. As discussed in Subsection 2.1.2, values of $\mathcal{E}_b$, a_0 and r_0 appearing in the wave function (4.3) correspond approximately to the proton-halo-isotope $^{8}_{5}$B [79–83], where its lifetime against β^+-decay and fission is about $\tau_{\rm B} \approx 769$ ms [61].

Now, we turn to the description of the proton-halo in the final state. Before we proceed, the dipole approximation for the laser vector potential discussed in Section 3.1 can be used: We will assume laser field parameters, where the dynamics of the emitted proton remains nonrelativistic. This means that the coupling parameter ξ in Eq. (3.2) between the laser beam and the proton-halo will always be small, $\xi \ll 1$. Here ω_L and E_L denote as before the frequency and the electric field strength of the laser field, respectively, while e denotes the electric charge of the emitted proton-halo. Further, the particle mass m in Eq. (3.2) should be replaced by the proton mass $m_{\rm p}$. Besides, in the present situation, the dipole approximation for the laser vector potential may be used, which gives Eq. (3.3).

As mentioned above, the laser serves as an accelerator or eventually inhibitor of the emitted proton. While the accelerations can significantly change the emitted proton energy, the work performed by the laser field on the proton will always be much smaller than the proton rest mass for the laser parameters under study. The final photoproton wave function can therefore be approximated as a nonrelativistic Volkov state in the continuum, as given by Eq. (3.6)

$$\psi_V(\vec{r},t) = \frac{1}{\sqrt{V_{\rm p}}} \exp\left[i\vec{p}\vec{r} - \frac{i}{2m_{\rm p}}\int_0^t \left(\vec{p} - e\vec{A}_L\right)^2 dt'\right], \tag{4.4}$$

where $\vec{p}$ represents the free momentum of the emitted proton-halo. In Eq. (4.4), the Coulomb interaction between the photoproton and the core-halo (having a total electric charge $(Z-1)\cdot e$) is neglected to another good approximation, because the velocity v of the photoproton is assumed to be high enough, that the latter cannot be affected significantly by the Coulomb field of the core. More details about this approximation will be pointed out in the beginning of Section 4.4.

By inserting Eq. (3.3) into Eq. (4.4) and by evaluating the integrals in the exponent, the Volkov wave function (4.4) of the photoproton-halo may be written in the following general form

$$\psi_V(\vec{r},t) = \frac{1}{\sqrt{V_{\rm p}}} \exp i\left[\vec{p}\vec{r} - \frac{p^2}{2m_{\rm p}}t - U_{\rm p}t\right]\cdot f(t), \tag{4.5}$$

with the time-dependent periodic function

$$f(t) = \exp\left[i\left(\alpha_1 \sin\omega_L t - \alpha_2\cos\omega_L t - \beta_1 \sin 2\omega_L t\right)\right]. \tag{4.6}$$

Assuming the laser field to be a monochromatic plane wave, polarized in the xy-plane and its electric field vector $\vec{E}_L$ perpendicular to the electric field vector $\vec{E}'$ of the γ-ray, we obtain

$$\alpha_1 \equiv \alpha_1^{\perp} = \frac{eE_L}{\omega_L^2 m_{\rm p}}\, p_x, \tag{4.7a}$$

$$\alpha_2 \equiv \alpha_2^{\perp} = \frac{eE_L}{\omega_L^2 m_{\rm p}}\, \delta_0\, p_y, \tag{4.7b}$$

$$\beta_1 = \frac{(eE_L)^2}{8\omega_L^3 m_{\rm p}}(1-\delta_0^2). \tag{4.7c}$$

Here the superscript "$\perp$" is used to indicate that the laser electric field vector is perpendicular to the polarization vector $\vec{\varepsilon}$ of the γ-ray, which is assumed along the z-axis throughout, as illustrated in Figure 4.2. The cycle averaged kinetic energy, also called the "*ponderomotive energy*" of the photoproton is given by

$$U_{\rm p} = \frac{(eE_L)^2}{4\omega_L^2 m_{\rm p}}(1+\delta_0^2), \tag{4.7d}$$

which accelerates or decelerates the photoproton as it travels out through the laser field. As we can see in this equation, the proton energy increases as the oscillation period $T_L = 2\pi/\omega_L$ and the electric field strength E_L increase. Notice that in Eq. (4.5) a constant phase $eE_L\delta_0 p_y/(\omega_L^2 m_{\rm p})$ arising from the lower boundary $t' = 0$ in Eq. (4.4) was ignored, because it will vanish by squaring the S-matrix as will be shown later.

The kinematic and dynamic behaviors of the photoproton depend not only on the physical quantities ω_L and E_L of the laser, but also on those of the γ-radiation, namely the wave vector $\vec{k}' \equiv \vec{p}\,'$, the frequency $\omega' \equiv 2\pi/\lambda'$ and the polarization vector $\vec{\varepsilon} \equiv \vec{e}_z$. The vector potential of the γ-radiation have to be expressed without the dipole approximation, because its wavelength λ' is not too large in comparison with the relevant values of $|\vec{r}|$ at the nuclear scale. It is thus safe to keep only the (resonant) energy-conserving terms in the γ-photon-proton interaction by writing the vector potential as follows

$$\vec{A}' = \sqrt{\frac{2\pi}{V_{ph}\cdot\omega'}}\cdot e^{i(\vec{p}\,'\vec{r}-\omega' t)}\vec{\varepsilon}. \tag{4.8}$$

This is known in quantum optics as the "*rotating wave approximation*".

In fact, in our theory, the proton-halo is affected by three types of interaction: First, the laser-proton interaction after the proton is removed from the nuclear-core by the γ-ray-induced photonuclear effect. This interaction may be described by the unperturbed Hamiltonian H_0 as expressed by Eq. (3.4). Second, the simultaneous interaction of the proton-halo with both radiation fields (the laser and the γ-ray), let us denote it by $H_{\rm coupling}$. Third, the strong interaction between the bound-proton-halo and the nuclear-core denoted $V_{\text{nuclear halo}}$. To take into account all these interactions, we can write the total Hamiltonian as follows

$$\begin{aligned} H &= \frac{1}{2m_{\rm p}}\left(\hat{p} - e\vec{A}_L - e\vec{A}'\right)^2 + V_{\text{nuclear halo}}, \\ &= \frac{1}{2m_{\rm p}}\left(\hat{p} - e\vec{A}_L\right)^2 + \frac{e}{m_{\rm p}}\left(\hat{p} - e\vec{A}_L\right)\vec{A}' + \underbrace{\frac{e^2\vec{A}'^2}{2m_{\rm p}}}_{\approx 0} + V_{\text{nuclear halo}}, \\ &= H_0 + H_{\rm coupling} + V_{\text{nuclear halo}}. \end{aligned} \tag{4.9}$$

In the second line we considered the term $e\vec{A}'$ as a perturbation, so that the second-order term $e^2\vec{A}'^2/2m_{\rm p}$ can be neglected. Now, the action of H_0 on the final proton wave function yields the Volkov State (4.5). Further, we assume that the action of $V_{\text{nuclear halo}}$ on the initial proton wave function yields the wave function (4.3) describing the bound-proton-halo state. Thus, we can use the expressions (4.3), (4.4) and (4.8) to write down the S-matrix in the first-order Born approximation for the transition from the initial bound halo state to the continuum Volkov state as follows

$$\begin{aligned} S &= \frac{ie}{m_{\rm p}}\int dt\, d^3\vec{r}\, \langle\psi_V|\left(-i\vec{\nabla} - e\vec{A}_L\right)\vec{A}'\,|\psi_0\rangle \\ &= \frac{i\ e\ \sqrt{2\pi}}{m_{\rm p}\sqrt{V_{\rm p}V_{ph}\omega'}}\int dt\, d^3\vec{r}\,\vec{\varepsilon}\left(\vec{p} - e\vec{A}_L\right)\cdot e^{-i(\vec{p}-\vec{p}\,')\cdot\vec{r}}\cdot e^{i\left(\frac{p^2}{2m_{\rm p}}+U_{\rm p}-\omega'\right)\cdot t}\cdot\psi_0(\vec{r},t)\cdot f(t). \end{aligned} \tag{4.10}$$

Here the momentum operator $-i\vec{\nabla} - e\vec{A}_L$ describes the electromagnetic coupling between the laser and the photoproton. The expression of the Volkov state in Eq. (4.5) is not well suited for calculating the S-matrix elements (4.10) due to the sinusoidal time dependent terms that appear on the right-hand side of the following expression

$$\vec{\varepsilon}\left(\vec{p} - e\vec{A}_L\right)\cdot f(t) = \vec{\varepsilon}\vec{p}\cdot f(t) - ae\varepsilon_x\cdot\cos(\omega_L t)f(t).$$

In order to make progress on this issue, we first make the calculations for a linearly polarized laser beam, $\delta_0 = 0 \Rightarrow \alpha_2 = 0$, then we expand analytically $f(t)$ and $\cos(\omega_L t) f(t)$ into Fourier series of coefficients B_n and C_n, respectively, we have

$$f(t) = \sum_{n=-\infty}^{+\infty} B_n \; e^{-in\omega_L t}, \tag{4.11a}$$

$$\cos(\omega_L t) f(t) = \sum_{n=-\infty}^{+\infty} C_n \; e^{-in\omega_L t}. \tag{4.11b}$$

These coefficients can be expressed in terms of the generalized Bessel-functions $\widetilde{J}$ of integer order n

$$\widetilde{J}_n(\alpha_1, \beta_1) = \sum_{m=-\infty}^{+\infty} J_{n-2m}(\alpha_1) J_m(\beta_1), \tag{4.12}$$

where J are ordinary Bessel-functions. We use the so-called "*Jacobi-Anger expansion*", which gives (see App. A.1)

$$\exp(i\alpha_1 \sin \omega_L t) = \sum_{l=-\infty}^{+\infty} J_l(\alpha_1) \; e^{-il\omega_L t}, \tag{4.13a}$$

$$\exp(-i\beta_1 \sin 2\omega_L t) = \sum_{m=-\infty}^{+\infty} J_m(\beta_1) \; e^{-im2\omega_L t}. \tag{4.13b}$$

Thus, we can express f in Eq. (4.6) (at $\delta_0 = 0$) as follows

$$\begin{aligned}
f(t) &= \exp\left(i\alpha_1 \sin \omega_L t - i\beta_1 \sin 2\omega_L t\right) \\
&= \sum_{l=-\infty}^{+\infty} J_l(\alpha_1) \; e^{-il\omega_L t} \cdot \sum_{m=-\infty}^{+\infty} J_m(\beta_1) \; e^{-i2m\omega_L t} \\
&= \sum_{m=-\infty}^{+\infty} \sum_{l=-\infty}^{+\infty} J_l(\alpha_1) J_m(\beta_1) \exp\left[-i \underbrace{(l+2m)}_{=n} \omega_L t\right] \\
&= \sum_{m=-\infty}^{+\infty} \sum_{n=-\infty}^{+\infty} J_{n-2m}(\alpha_1) J_m(\beta_1) \cdot e^{-in\omega_L t} \\
&= \sum_{n=-\infty}^{+\infty} \left(\sum_{m=-\infty}^{+\infty} J_{n-2m}(\alpha_1) J_m(\beta_1) \right) \cdot e^{-in\omega_L t} \\
&= \sum_{n=-\infty}^{+\infty} \widetilde{J}_n(\alpha_1, \beta_1) \cdot e^{-in\omega_L t}.
\end{aligned} \tag{4.14}$$

The above transitions from line 2 to line 4 are always true since the sum over n runs from $-\infty$ to $+\infty$. Now a simple identification of B_n and C_n by using Eqs. (4.11) and Eq. (4.14) yields[1]

$$B_n = \widetilde{J}_n(\alpha_1, \beta_1), \tag{4.15a}$$

$$C_n = \frac{1}{2}\left[\widetilde{J}_{n+1}(\alpha_1, \beta_1) + \widetilde{J}_{n-1}(\alpha_1, \beta_1)\right]. \tag{4.15b}$$

Hence, the S-matrix elements (4.10) can be written in the following discrete form

$$\begin{aligned}
S = &\frac{i\; e\; \sqrt{2\pi}}{m_{\rm p}\sqrt{V_{\rm p} V_{ph} \omega'}} \sum_{n=-\infty}^{+\infty} \int dt \; \exp\left[i\left(\frac{p^2}{2m_{\rm p}} + U_{\rm p} - \omega' - n\omega_L\right) \cdot t\right] \times \left[\vec{\varepsilon}\vec{p}\; B_n - ae\varepsilon_x \; C_n\right] \times \\
&\int d^3\vec{r} \; \exp\left[-i\,(\vec{p} - \vec{p}\,') \cdot \vec{r}\,\right] \cdot \psi_0(\vec{r}).
\end{aligned} \tag{4.16}$$

[1] The result in Eq. (4.15b) is obtained by replacing $\cos(\omega_L t)$ in Eq. (4.11b) by $\left(e^{i\omega_L t} + e^{-i\omega_L t}\right)/2$.

The first integral over time gives the following delta function

$$\int dt\ \exp\left[i\left(\frac{p^2}{2m_{\rm p}}+U_{\rm p}-\omega'-n\omega_L\right)\cdot t\right]=2\pi\times\delta\left(\frac{p^2}{2m_{\rm p}}+U_{\rm p}+\mathcal{E}_b-\omega'-n\omega_L\right),$$

which expresses the energy conservation for the photonuclear process observed in the center of mass of the daughter nucleus (or the core-halo). Further, we simplify the notations by setting $q=\|\vec{p}-\vec{p}\,'\|$ the momentum transfer from the γ-ray field to the photoproton, and by

$$\mathcal{M}_n\equiv\mathcal{M}_n^{\perp}=\vec{\varepsilon}\vec{p}\ B_n-ae\varepsilon_x\ C_n, \tag{4.17}$$

the transition amplitude for the photonuclear process, which is expressed in terms of the above generalized Bessel-functions. The second integral in Eq. (4.16) over the three spherical coordinates yields the fourier transform of the bound halo state

$$G(q)=\frac{4r_0^3\left[12r_0^2\ (q^2r_0^2-1)+a_0^2(1+q^2r_0^2)^2\right]}{a_0^2(1+q^2r_0^2)^4}. \tag{4.18}$$

We finally arrive to the following expression for the S-matrix

$$S=\frac{2i\sqrt{2}c_0e\pi^2}{m_{\rm p}\sqrt{V_{\rm p}V_{ph}\omega'}}\sum_{n=n_0}^{+\infty}\mathcal{M}_n\cdot G(\vec{p}-\vec{p}\,')\cdot\delta\left(\frac{p^2}{2m_{\rm p}}+U_{\rm p}+\mathcal{E}_b-\omega'-n\omega_L\right), \tag{4.19}$$

where n_0 represents the smallest integer that satisfies the energy conservation relation for the photonuclear reaction (4.2)

$$n_0=\text{floor}\left[\frac{1}{\omega_L}\left(\frac{p^2}{2m_{\rm p}}+U_{\rm p}+\mathcal{E}_b-\omega'\right)\right]+1. \tag{4.20}$$

The total rate for the photonuclear proton emission in the presence of the combined field consisting of the strong optical laser and the γ-radiation is obtained by squaring the S-matrix (4.19), integrating over all possible momenta configurations of the final proton state and dividing by a unit time T, that is

$$R=\frac{1}{T}\int\frac{V_{\rm p}\ d^3\vec{p}}{(2\pi)^3}\cdot|S|^2. \tag{4.21}$$

First the square of Eq. (4.19) is

$$|S|^2=\frac{8\pi^4(ec_0)^2}{V_{\rm p}V_{ph}\omega' m_{\rm p}^2}\cdot\sum_{n\geqslant n_0}\sum_{n'\geqslant n_0}\mathcal{M}_n\mathcal{M}_{n'}\ G(q)^2\cdot\delta(Q_n)\delta(Q_{n'}),$$

with

$$Q_n\equiv\frac{p^2}{2m_{\rm p}}+U_{\rm p}+\mathcal{E}_b-\omega'-n\omega_L.$$

For large but finite values of T, we consider transitions in the time interval $[-T/2,T/2]$, during which the total energy $n\omega_L$ of the exchanged laser photons, satisfies the energy conservation relation $Q_n\to0$. In that case, the energy δ-function can approximately be written as follows

$$\delta(Q_{n'})\approx\frac{1}{2\pi}\int_{-T/2}^{T/2}dt\ e^{iQ_{n'}t}=\frac{1}{2\pi Q_{n'}}\cdot\left[\sin(Q_{n'}t)-i\cos(Q_{n'}t)\right]_{-T/2}^{T/2}=\frac{1}{\pi Q_{n'}}\sin\left(\frac{T}{2}Q_{n'}\right).$$

Since we have

$$\lim_{Q_{n'}\to0}\delta(Q_{n'})=\frac{T}{2\pi}\lim_{Q_{n'}\to0}\frac{\sin\left(\frac{T}{2}Q_{n'}\right)}{\left(\frac{T}{2}Q_{n'}\right)}=\frac{T}{2\pi},$$

the square of the S-matrix under the constraint $Q_{n'} \to 0$ becomes

$$|S|^2 = \frac{4\pi^3 (ec_0)^2\ T}{V_\mathrm{p} V_{ph} \omega' m_\mathrm{p}^2} \cdot \sum_{n \geqslant n_0} \mathcal{M}_n^2\ G(q)^2 \cdot \delta(Q_n). \tag{4.22}$$

After substitution of Eq. (4.22) into Eq. (4.21) we thus arrive at the following expression for the total rate

$$\begin{aligned} R &= \frac{1}{T} \int \frac{V_\mathrm{p}\ d^3\vec{p}}{(2\pi)^3} \cdot |S|^2 \\ &= \frac{(ec_0)^2}{2 V_{ph} \omega' m_\mathrm{p}^2} \sum_{n=n_0}^{+\infty} \int_0^\pi d\theta \int_0^{2\pi} d\varphi \int_0^{+\infty} dp\ |\vec{p}|^2 \mathcal{M}_n^2 \cdot G(\vec{p} - \vec{p}\,')^2 \cdot \delta\left(\frac{p^2}{2m_\mathrm{p}} + U_\mathrm{p} + \mathcal{E}_b - \omega' - n\omega_L \right). \end{aligned} \tag{4.23}$$

We remember that the total and differential rates refer to the core-halo frame. The polar emission angle θ is measured with respect to $\vec{e}_z$, which coincides with the polarization direction of the γ-ray, and perpendicular to its wave vector $\vec{k}' = k'\vec{e}_x$ (see Fig. 4.2). The integration over the photoproton momentum p can be performed by using the following general formula

$$\int dp\ \delta\left(g(p)\right) F(p) = \sum_{i=1}^{m} \frac{F(p_i)}{|g'(p_i)|},$$

where p_i are the roots of the equation $g(p) = 0$. In our case the function g of p is equivalent to $g(p) \equiv Q_n = p^2/(2m_\mathrm{p}) + U_\mathrm{p} + \mathcal{E}_b - \omega' - n\omega_L$, so that its derivative with respect to p is simply $g'(p) = p/m_\mathrm{p}$, and we have only one positive root

$$p_n \equiv \|\vec{p}\| = \sqrt{2m_\mathrm{p}\left(\omega' + n\omega_L - U_\mathrm{p} - \mathcal{E}_b\right)}. \tag{4.24}$$

From there we can deduce the three components of the final photoproton momentum as follows

$$p_x = p_n \sin\theta \cos\varphi, \tag{4.25a}$$
$$p_y = p_n \sin\theta \sin\varphi, \tag{4.25b}$$
$$p_z = p_n \cos\theta. \tag{4.25c}$$

Physically, the subscript n refers to the number of coherently emitted (for $n > 0$) or coherently absorbed (for $n < 0$) laser photons. Further, the above function F is equivalent to

$$F(p) \equiv |\vec{p}|^2 \left[\vec{\varepsilon}\vec{p}\ B_n - ae\varepsilon_x\ C_n\right]^2 \cdot G(\vec{p} - \vec{p}\,')^2.$$

Thus the expression of the total rate in Eq. (4.23) becomes

$$R = \sum_{n=n_0}^{+\infty} R_n = \frac{(ec_0)^2}{2 V_{ph} \omega' m_\mathrm{p}} \sum_{n=n_0}^{+\infty} \int_0^\pi d\theta \int_0^{2\pi} d\varphi\ p_n\ \mathcal{M}_n^2 \cdot G(\vec{p}_n - \vec{p}\,')^2. \tag{4.26}$$

We finally deduce the total cross section of the photonuclear process by dividing Eq. (4.26) by the γ-photon flux $\Phi = 1/V_{ph}$, i.e. the number of photons (quanta of the γ-radiation) per unit area per unit time, to obtain explicitly

$$\boxed{\sigma = \sum_{n=n_0}^{+\infty} \sigma_n = \frac{(ec_0)^2}{2\omega' m_\mathrm{p}} \sum_{n=n_0}^{+\infty} \int_0^\pi d\theta \int_0^{2\pi} d\varphi\ p_n\ \left[\vec{\varepsilon}\vec{p}_n\ B_n - ae\varepsilon_x\ C_n\right]^2 \cdot G(\vec{p}_n - \vec{p}\,')^2.} \tag{4.27}$$

This equation gives a measure of the probability that reaction (4.2) will occur and can be solved numerically. It includes two integrals, one over the polar emission angle θ and the other over the azimuthal angle φ, and a summation of infinite series associated with Bessel-functions.

4.4 Results and Discussion

For the presentation of the numerical results we have chosen to mainly discuss the characteristic influences of the assisting laser field on the properties of the photonuclear effect. We investigate the energy distribution of the ejected proton in terms of the number of absorbed laser photons, as well as the angular proton distribution as a function of the polar emission angle with respect to the electric field vector of the γ-photon, which coincides with $\vec{e}_z$. The dependencies on the photon energy, the laser polarization, and the field geometry are discussed as well. We first show and discuss the results obtained for the case where the laser beam is linearly polarized, and after that the case of circular polarization.

In fact, we extend our discussion of the numerical results by considering two scenarios of the laser assisted photonuclear process: (i) The electric field vectors of the laser wave and the γ-photon are perpendicular to each other, $\vec{E}_L \perp \vec{E}'$, as illustrated before in Figure 4.2, and (ii) the electric field vectors of the laser wave and the γ-photon are parallel to each other, so that the laser beam copropagates with the γ-ray along the x-axis, $\vec{E}_L \parallel \vec{E}'$, as illustrated in Figure 4.3.

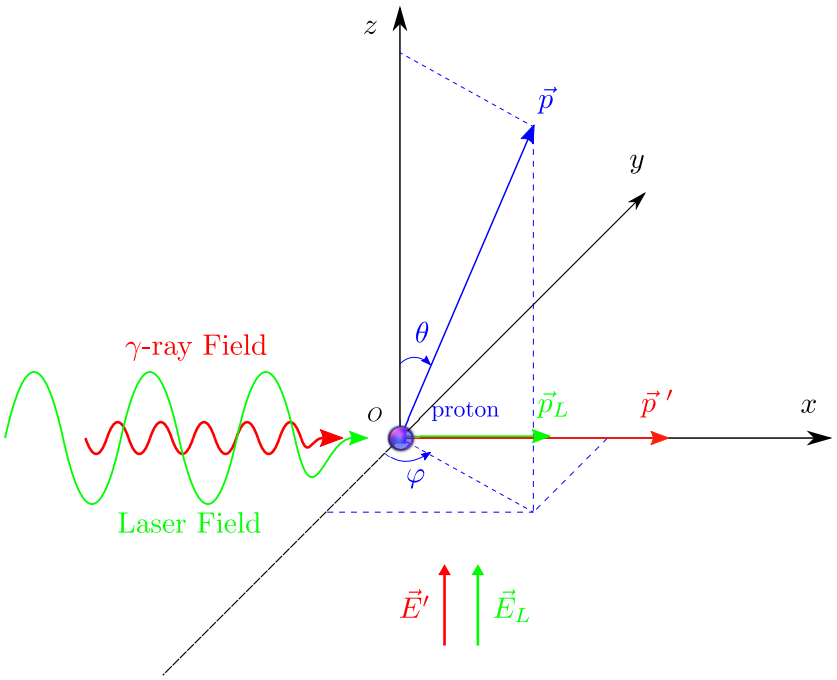

Figure 4.3: Schematic diagram of the laser-assisted photonuclear effect. The z-axis has been chosen along the polarization direction of the laser wave and the γ-radiation, $\vec{E}_L \parallel \vec{E}'$.

In the second scenario, few modifications should be made to the arguments $\alpha_1^{\perp}$ and $\alpha_2^{\perp}$ of the Bessel-functions, as well as to the transition amplitude for the photonuclear process. Concretely, Eq. (4.7a) should be replaced by[2]

$$\alpha_1 \equiv \alpha_1^{\parallel} = \frac{eE_L}{\omega_L^2 m_{\rm p}}\, p_z, \tag{4.28}$$

and Eq. (4.17) by

$$\mathcal{M}_n \equiv \mathcal{M}_n^{\parallel} = \vec{\varepsilon}\vec{p}\, B_n - ae\varepsilon_z\, C_n. \tag{4.29}$$

Values of the input parameters indicated in the Table 4.1 of Section 4.3 have been used throughout the discussion of our results. Furthermore, we keep the γ-ray photon energy fixed at $\omega' = 3$ MeV (i.e. $\lambda' \sim 413.28$ fm)

[2]In analogy to what we did before, the superscript "$\parallel$" is used to indicate that the laser electric field vector is parallel to the polarization vector $\vec{\varepsilon}$ of the γ-ray, i.e. $\vec{E}_L \parallel \vec{E}'$, as illustrated in Figure 4.3.

for the following reason: In the theoretical calculation, we assumed that the velocity $v_n = p_n/m_\mathrm{p}$ (for an explicit expression of p_n, see Eq. (4.24)) of the photoproton is high enough, that the latter cannot be affected significantly by the Coulomb field of the core-halo. This approximation may be justified from the rather small Gamow factor [135]

$$G = \frac{\eta}{1 - e^{-\eta}} \simeq 1 \sim 3, \tag{4.30}$$

with $\eta = 2\pi(Z-1)\alpha/v_n \ll 1$ and α is the fine-structure constant. So, taking $Z = 5$ for boron, the Gamow factor varies between 1 and 3, which means that the nonrelativistic Volkov state given by Eq. (4.4) remains a reasonable approximation for the description of the final photoproton wave function in the continuum, and may be applied instead of the so called "improved Coulomb-Volkov state" [30, 32, 33].

4.4.1 The case of linearly polarized laser beam

We first consider a linearly polarized hard x-ray free-electron laser (e.g. based on planar undulator systems) with wavelength $\lambda_L \simeq 0.62$ nm and photon energy $\omega_L = 2$ keV. This energy scale can in principle be achieved experimentally by the XFEL at DESY or the LCLS at SLAC.

In Figure 4.4 we show the total cross section $\sigma^\perp$ for the photoproton as a function of the frequency ω' of the γ-ray photon, keeping fixed the laser's electric field strength at $E_L = 3.07 \times 10^{13}$ V/cm for the red curve. This plot is compared with the case when the photonuclear process is induced classically, i.e. without the assistance of the high-frequency laser beam as shown by the dashed black curve. We see that both curves practically superpose on each other, which means that the presence of the laser beam, with such a high frequency and electric field strength, has only a minor effect on the γ-photon energy dependence of the total cross section.

Photonuclear reactions	σ_max **[mb]**
$^4\mathrm{He}(\gamma,\mathrm{p})^3\mathrm{H}$	≈ 1.75 [136]
$^{12}\mathrm{C}(\gamma,\mathrm{p})^{11}\mathrm{B}$	≈ 13.1 [137]
$^{17}\mathrm{O}(\gamma,\mathrm{p})^{16}\mathrm{N}$	≈ 4.0 [138]
$^{24}\mathrm{Mg}(\gamma,\mathrm{p})^{23}\mathrm{Na}$	≈ 25.0 [138]
$^{26}\mathrm{Mg}(\gamma,\mathrm{p})^{25}\mathrm{Na}$	≈ 18.0 [138]
$^{28}\mathrm{Si}(\gamma,\mathrm{p})^{27}\mathrm{Al}$	≈ 45.0 [138]
$^{34}\mathrm{S}(\gamma,\mathrm{p})^{33}\mathrm{P}$	≈ 33.0 [138]
$^{93}\mathrm{Nb}(\gamma,\mathrm{p})^{92}\mathrm{Zr}$	≈ 15.0 [139]

Table 4.2: Maximum cross sections of some photoproton reactions that have been induced by energetic photons (between 22 and 30 MeV) from synchrotron and electron bremsstrahlung sources. The cross-sectional data are taken from [136–139].

In both cases, the total cross section attains its maximum value of roughly 366.7 mb at $\omega' \approx 0.74$ MeV, and decreases steadily towards higher γ-photon energies. This maximum value is approximately 16 times larger than those obtained from experimental data of photoproton cross sections in stable nuclei [136–139], as listed in Table 4.2. The result confirms our expectation that it is easier to induce a photonuclear reaction in halo-nuclei than in stable ones by using high-energy photons, because of their small binding energy and their large spatial extension.

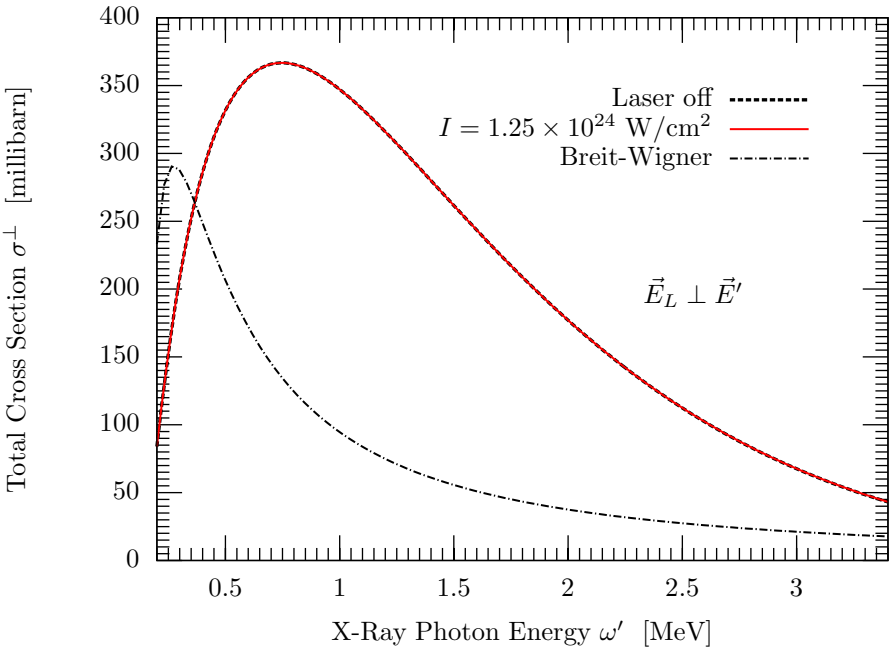

Figure 4.4: The total cross section given by Eq. (4.27) for the photoproton-halo in the presence of the combined field of the γ-ray and the high-frequency laser, as a function of the photon energy of the γ-ray. The input parameters for the red curve are: $E_L = 3.07 \times 10^{13}$ V/cm and $\omega_L = 2 \times 10^{-3}$ MeV, which correspond to a laser intensity of 1.25×10^{24} W/cm^2. The dashed black curve represents the classical case of the photonuclear reaction (4.2) induced by the γ-photon without the assistance of the laser beam. The electric field vectors of both the laser wave and the γ-photon are perpendicular to each other, $\vec{E}_L \perp \vec{E}'$. The results were compared with those obtained from the Breit-Wigner single level formula, which permits to calculate the photodisintegration cross section of the deuteron (black dot-dashed curve).

It would be interesting to compare our results with those obtained from relevant theories of photonuclear reactions. For example, the cross section for the reaction (4.2) my be estimated by the following Breit-Wigner formula [140, 141]

$$\sigma(\omega') = \frac{8\pi(Ze)^2}{3m_{\rm p}\mathcal{E}_b} \cdot \left(\frac{\mathcal{E}_b(\omega' - \mathcal{E}_b)}{\omega'^2}\right)^{3/2}, \tag{4.31}$$

which is one of the most successful expressions ever written in nuclear and hadronic physics. We point out that the following assumptions are behind Eq. (4.31): First, it gives the photodisintegration cross section of the deuteron ($Z = 1$) described by the photonuclear reaction (4.1a), around the resonance energy, and considers the transition from the bound $^3S_1$ state to the $^1S_0$ state of the continuum. Second, Eq. (4.31) assumes that the reaction (4.1a) is induced at energies far above the threshold.
Compared to our calculations, the Breit-Wigner cross section is strongly dependent on the γ-photon energy, strongly suppressed and peaked at small energies, as shown in Fig. 4.4 by the black dot-dashed curve. At $\omega' = 0.274 = 2 \cdot \mathcal{E}_b$, the total cross section attains its maximum value of 290.889 mb, which is roughly 76 mb smaller than those obtained in our calculations.

In Figs. 4.5 and 4.6, we investigate the energy distribution of the photoproton in terms of the number n of absorbed ($n > 0$) or emitted ($n < 0$) laser photons by considering different polarization directions of the radiation fields. Here, the photoproton absorbs an amount of energy from the laser beam equal to $n\omega_L$. In each graph we keep the γ-ray photon energy fixed at 3 MeV, the laser frequency at 2 keV and we increase the laser's electric field strength from 2.45×10^{11} V/cm to 3.07×10^{13} V/cm, or equivalently the laser intensity from 8×10^{19} W/cm^2 to 1.25×10^{24} W/cm^2.

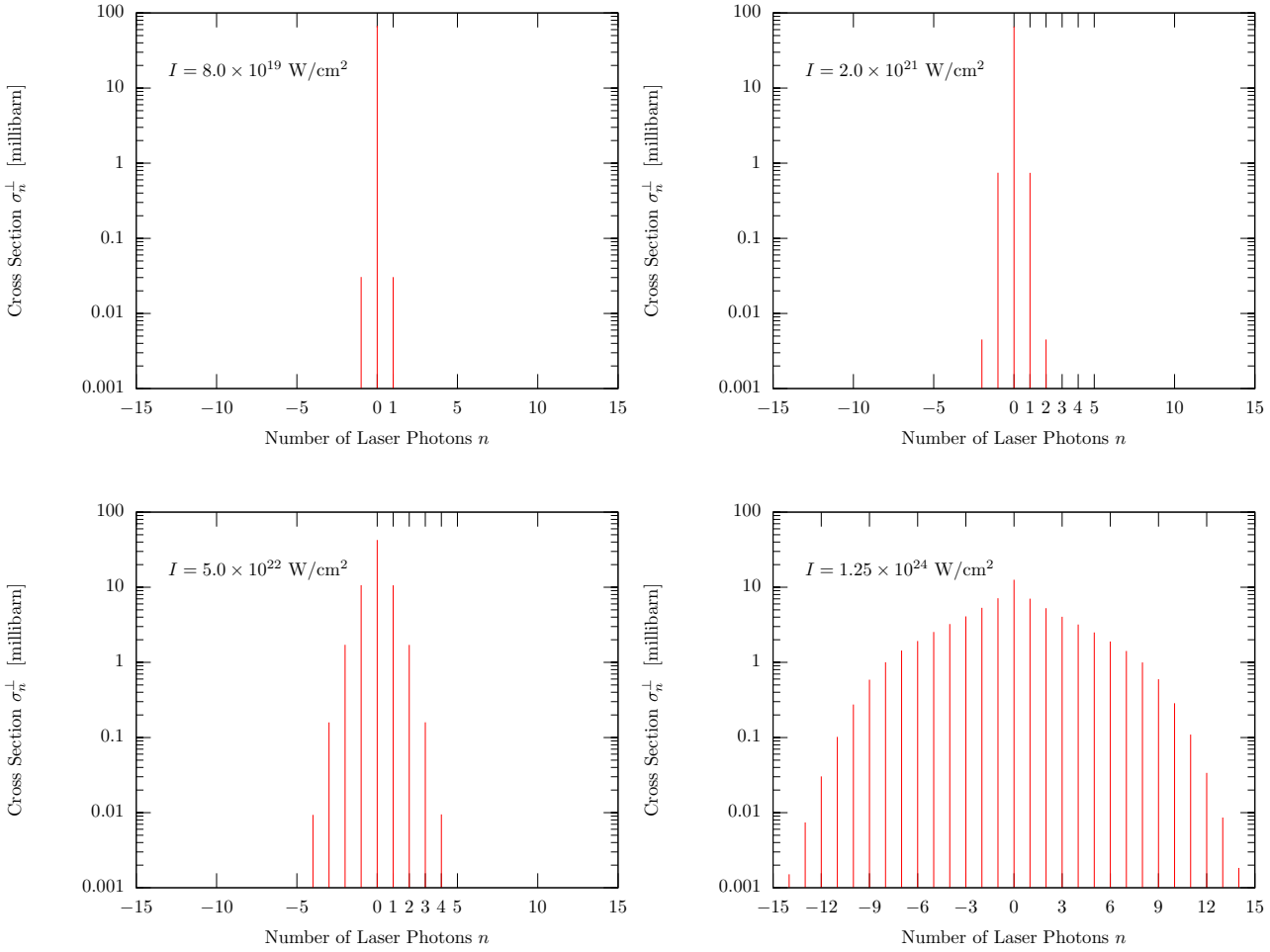

Figure 4.5: The energy distribution of the photoproton in term of the number n of exchanged laser photons and at various laser intensities. For example, when $n = 12$, the proton absorbs an amount of energy from the laser light equal to 12×2 keV $= 24$ keV. The polarization directions of the laser field and the γ-ray are perpendicular to each other, $\vec{E}_L \perp \vec{E}'$ as described by Fig. 4.2. Values of the photon energy of the laser and of the γ-ray are held fixed as before. The laser's electric field strength is increased from top to bottom as follows: $E_L = 2.45 \times 10^{11}$, 1.22×10^{12}, 6.14×10^{12}, and 3.07×10^{13} V/cm. The corresponding laser intensities are indicated on each graph. The total cross section $\sigma^\perp = \sum_n \sigma_n^\perp$ remains unchanged in all graphs at roughly 67.6 mb.

For a given integer n, each photonuclear reaction in Eq. (4.2), involving emission or absorption of n laser photons, has its own probability and cross section σ_n. For each type of multiphoton or single-photon reaction channel, we obtain an individual probability, so that the total probability of any photonuclear reaction occurring is the sum of the individual probabilities. Similarly, the sum of all the individual photoproton cross sections σ_n is the total cross section σ, which remains unchanged at

$$\sigma \equiv \sigma_{\text{linear}} = 67.578 \pm 0.001 \text{ mb}, \tag{4.32}$$

for a linearly polarized laser. This value is independent on the orientation of the electric field vector $\vec{E}_L$ with respect to $\vec{E}'$ of the γ-ray, i.e. we have $\sigma^\perp = \sigma^\parallel = 67.578 \pm 0.001$ mb at $\omega' = 3$ MeV, and it also remains unchanged when the laser is turned off.

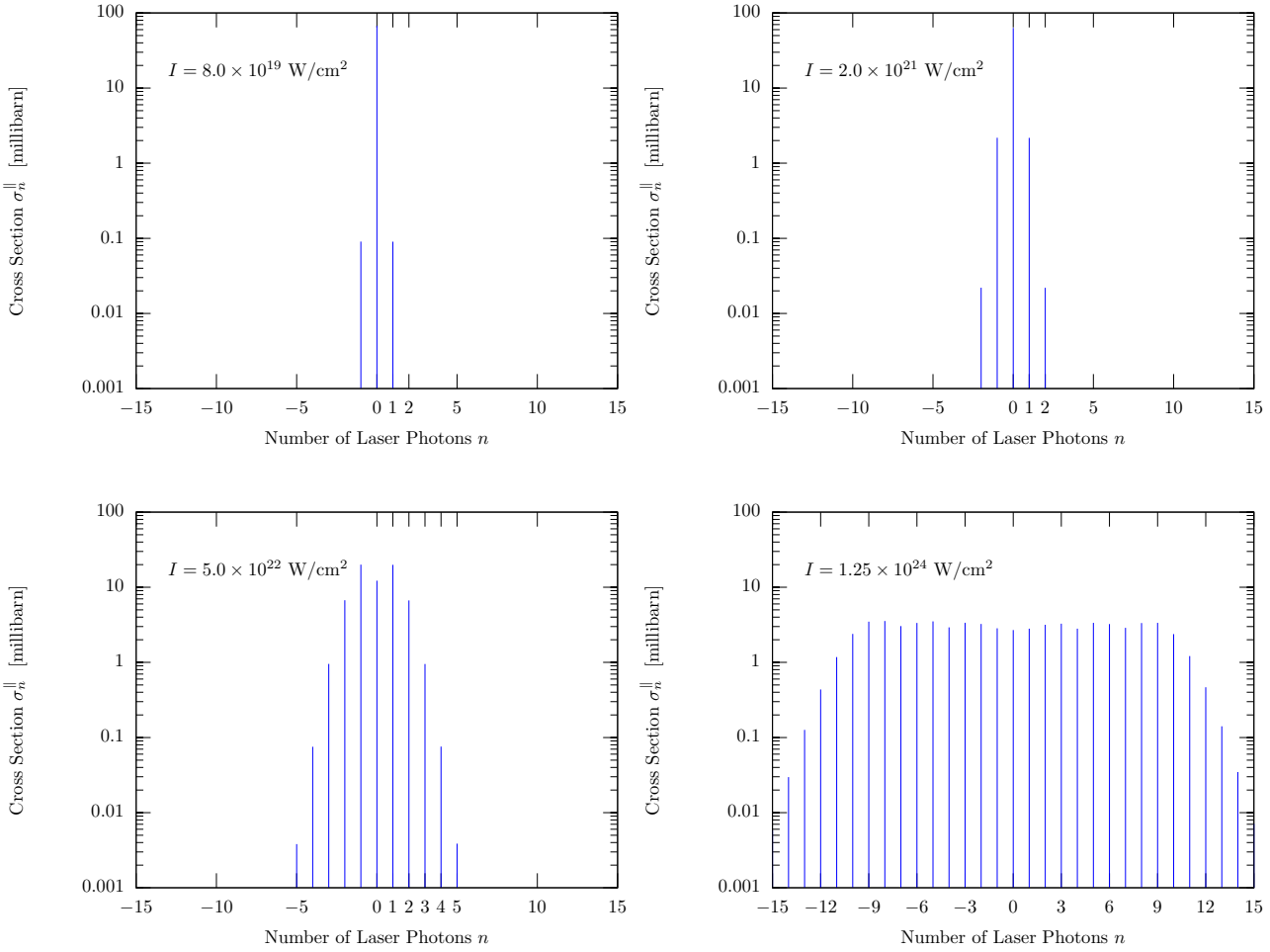

Figure 4.6: Same as Fig. 4.5 except that the second scenario described by Fig. 4.3 is considered, where $\vec{E}_L \parallel \vec{E}'$.

There are two other common characteristics shared by Figs. 4.5 and 4.6, independently on the laser intensity. First, the energy spectrum becomes broader by increasing the laser intensity, and in each graph the total cross section remains constant at the value given by Eq. (4.32). Second, all graphs are symmetric around $n = 0$, which means that the absorption and the emission of n laser photons have almost the same probabilities. The latter characteristic agrees with that reported by the Low's theorem for multiphoton processes [142].

Apart from common characteristics, there are also some noteworthy differences between Figs. 4.5 and 4.6. First of all, in Fig. 4.5 where $\vec{E}_L \perp \vec{E}'$, $\sigma_n^{\perp}$ reaches its maximum value for $n = 0$, where the laser does not interact with the photoproton, and afterwards it decreases with increasing the number of absorbed or emitted laser photons. This behavior is explained by the fact that the arguments $\alpha_1^{\perp}$ and β_1 in Eqs. (4.7) are much smaller than 1 at all intensities. So we have $4.7 \times 10^{-5} \leqslant \alpha_1^{\perp} \leqslant 5.7 \times 10^{-3}$ and $3.9 \times 10^{-7} \leqslant \beta_1 \leqslant 6.1 \times 10^{-3}$. Therefore, we can well approximate $B_n(\alpha_1^{\perp})$ and $C_n(\alpha_1^{\perp})$ as: $const \cdot (\alpha_1^{\perp})^n$ and the cross section behavior is perturbative

$$\sigma_n^{\perp} \sim \alpha_1^{2n}.$$

In contrast, in Fig. 4.6 where $\vec{E}_L \parallel \vec{E}'$, the α_1^{2n} approximation of $\sigma_n^{\parallel}$ cannot be justified for high intensities, because $9.6 \times 10^{-2} \leqslant \alpha_1^{\parallel} \leqslant 12.03$. A maximum value of $\sigma_n^{\parallel}$ for $n = 0$ can already be seen in the first and second graphs of Fig. 4.6, but just at laser intensity below 2×10^{21} W/cm^2 because we still have $\alpha_1^{\parallel} < 1$. The meaning of this result is clear: When the intensity of the assisted linearly polarized laser is low, the change of orientation of $\vec{E}_L$ with respect to $\vec{E}'$ plays no significant role on the photonuclear effect.

However, the third and fourth graphs in Fig. 4.6 show that the assisting laser field with high intensity modifies the properties of the photonuclear effect in a characteristic way. In other words, when $I \gtrsim 5 \times 10^{22}$ W/cm^2 and $\vec{E}_L \parallel \vec{E}'$, we have $2.4 \lesssim \alpha_1^{\parallel} \leqslant 12.03$, i.e. greater than 1, and therefore we cannot approximate $B_n(\alpha_1)$ and $C_n(\alpha_1)$ as: $const \cdot (\alpha_1)^n$. In that case, the coupling of the continuum proton to the laser field is nonperturbative. For this reason, we cannot see a maximum value of the cross section for $n = 0$ in the high-intensity regime, and σ_n depends strongly on the laser parameters ω_L and E_L.

From this comparison we conclude that the multiphoton character of the photonuclear reaction (4.2) in the halo-nucleus ${}^{A}_{Z}$[Xp] becomes most apparent at higher laser's electric field strengths and for copropagating waves. In contrast, single-photon character of the photonuclear process is apparent at low electric field strengths and particularly for orthogonally propagating waves. In general terms, we observed a strong effect of the orientation of the laser's electric field vector on the energy spectra of the photoproton-halo, particularly in the high-intensity regime. As we shall explain below, the dependence on the field orientation arises from the fact that the photoproton is preferentially emitted along the polarization direction of the γ-ray field (i.e., $\vec{e}_z$), whereas the coupling strength between the proton and the laser field depends on the proton momentum component along the laser polarization direction.

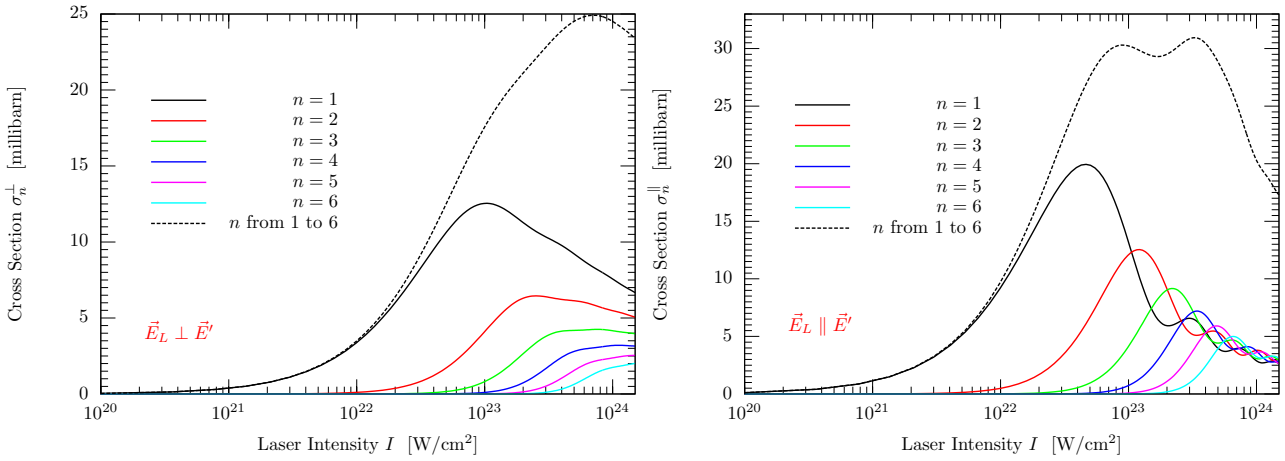

Figure 4.7: The cross sections of the photoproton as a function of the laser intensity for various numbers of absorbed laser photons. The left plot gives the cross section when $\vec{E}_L \perp \vec{E}'$ and the right one when $\vec{E}_L \parallel \vec{E}'$. The photon energies of the γ-ray and of the laser beam are held fixed at $\omega' = 3$ MeV and $\omega_L = 2$ keV, respectively.

Inspired from the results obtained in Figs. 4.5 and 4.6, we want to check now whether the photonuclear reaction in the halo-nucleus can be affected by increasing the laser intensity and by changing as before the polarization directions of the laser wave and the γ-photon, or not. In the left plot of Figure 4.7 we give the photoproton cross section in term of the laser intensity for various numbers of absorbed ($n > 0$) laser photons and when $\vec{E}_L \perp \vec{E}'$. In the right plot we give the same cross section but when $\vec{E}_L \parallel \vec{E}'$. The dashed curves represent the "total" cross sections by summing over all the number of absorbed laser photons from 1 to 6.

When $\vec{E}_L \perp \vec{E}'$ and for one-photon absorption, the cross section attains its maximum value of

$$\sigma^{\perp}_{\rm max}[n = 1, \text{linear}] \simeq 12.54 \text{ mb}, \tag{4.33}$$

at $I = 1.04 \times 10^{23}$ W/cm^2, as indicated by the solid black curve in the left plot. When $\vec{E}_L \parallel \vec{E}'$, the maximum value of the cross section increases to

$$\sigma^{\parallel}_{\rm max}[n = 1, \text{linear}] \simeq 19.94 \text{ mb}, \tag{4.34}$$

at lower intensity of $I = 4.65 \times 10^{22}$ W/cm^2, as indicated by the solid black curve in the right plot. This fact can be intuitively understood from the values of the first argument α_1 of the generalized Bessel-function, which

depends on $p_x = \|\vec{p}\| \sin\theta \sin\varphi$ when $\vec{E}_L \perp \vec{E}'$ as given by Eq. (4.7a), and on $p_z = \|\vec{p}\| \cos\theta$ when $\vec{E}_L \parallel \vec{E}'$ as given by Eq. (4.28). Since the integration over the polar emission angle θ goes from 0 to π, and the emission of the photoproton is mostly pronounced in the same direction as $\vec{E}'$ (i.e. along the z-axis), we have $\theta \sim 0$ and thus $p_x < p_z$. That is $\alpha_1^{\perp} < \alpha_1^{\parallel}$. By comparing the transition amplitude (4.17) with (4.29) for $n = 1$, we have $|\mathcal{M}_{n=1}^{\perp}|^2 \leqslant |\mathcal{M}_{n=1}^{\parallel}|^2$, because

$$|\widetilde{J}_{n=1}(\alpha_1^{\perp}, \beta_1)|^2 \leqslant |\widetilde{J}_{n=1}(\alpha_1^{\parallel}, \beta_1)|^2 \quad \forall\ \varphi \in [0, 2\pi],$$

and consequently, $\sigma_{\max}^{\perp} < \sigma_{\max}^{\parallel}$. This means physically, that the probability of inducing the photonuclear process by one-photon absorption, that we have defined in Eq. (4.10) by the transition from the initial bound halo state to the continuum Volkov state, is higher when the high-frequency laser wave is copropagating with the γ-ray. Indeed, we have found that $2 \times 10^{-4} \leqslant \alpha_1^{\perp} \leqslant 8 \times 10^{-3}$ and $0.67 \leqslant \alpha_1^{\parallel} \leqslant 16.57$ when the laser intensity varies between 10^{20} and 10^{24} W/cm^2.

There are some common and contrasting features between the left and right plots in Fig. 4.7: First, in each one the photoproton cross section decreases with increasing the number of absorbed laser photons from 1 to 6. Second, for any $n > 0$ the cross sections $\sigma_n^{\perp}$ and $\sigma_n^{\parallel}$ exhibit a monotonous increase at low laser intensities. The larger the integer n, the broader the linear region will be. This happens because $\alpha_1^{\parallel}$ (~ 0.67) and particularly $\alpha_1^{\perp}$ ($\sim 2 \times 10^{-4}$) are less than 1, so that the coefficients B_n and C_n appearing in Eqs. (4.15) [, which are expressed in terms of the generalized Bessel-function $\widetilde{J}_n(\alpha_1, \beta_1)$] are proportional to α_1^n. After the region of linearity, i.e. at higher intensities, the cross sections exhibit a decreasing behavior, which is mainly caused by the Bessel-functions like $J_n(\alpha_1)^2$. This behavior also agrees with that reported by C. Leone *et al.* in 1988 by studing "*two-frequency multiphoton ionization of hydrogen atoms*" [32].
Above 10^{23} W/cm^2, the cross section $\sigma_n^{\parallel}$ is strongly affected by the asymptotic behavior of the Bessel-functions, i.e. it oscillates with slowly decreasing amplitude for large arguments $\alpha_1^{\parallel}$ and β_1, or briefly at higher electric field strength E_L. On the other hand, the cross section $\sigma_n^{\perp}$ is less sensitive to the oscillation of the Bessel-functions. The non-oscillating behavior observed for $\sigma_n^{\perp}$ at such a high intensity is due to the fact that $\alpha_1^{\perp}$ is always less than 1, while $\alpha_1^{\parallel}$ becomes greater than 1 (~ 16.5, and hence causing the decreasing oscillation of $\sigma_n^{\parallel}$). Physically, we explain these facts by the back and forth motion of the photoproton as it travels out through the high-frequency laser field, which becomes more sensitive for copropagating waves than for orthogonally propagating waves.

Let us now explore the dependencies of the angular proton distribution on field orientations and intensities. First, we display in Fig. 4.8 the differential cross sections for the photonuclear reaction (4.2) as a function of the polar emission angle θ of the photoproton between 0 and $\pi/2$. Here $d\sigma/d\cos\theta$ are computed by integrating the azimuthal angle φ as usual from 0 to 2π and summing over all numbers of absorbed laser photons. We consider as before two polarization directions of the radiation fields, i.e. $\vec{E}_L \perp \vec{E}'$ and $\vec{E}_L \parallel \vec{E}'$ as illustrated in Figs. 4.2 and 4.3, respectively. In both scenarios, the polar emission angle θ is measured with respect to the z-axis, which coincides with $\vec{E}'$.

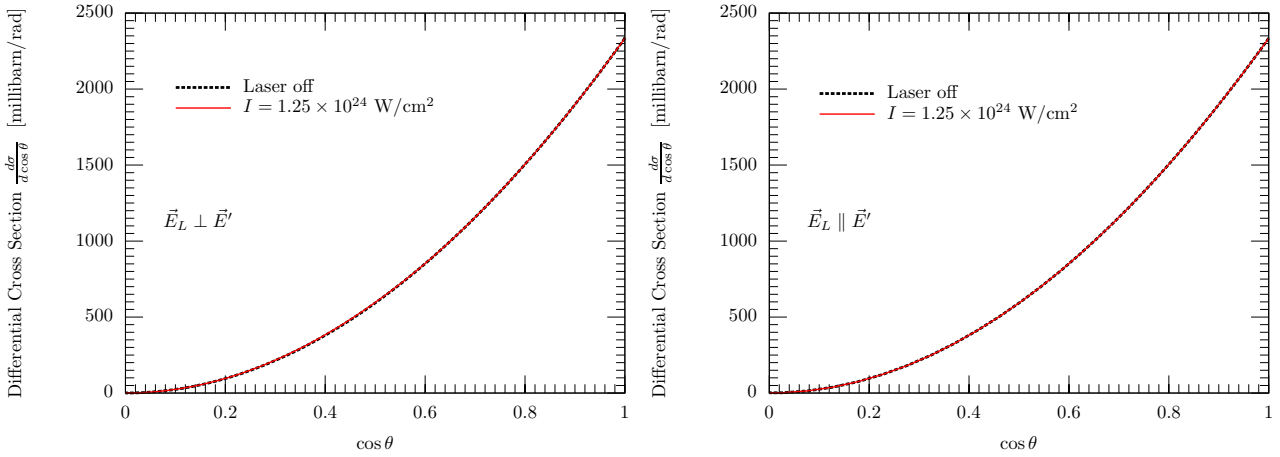

Figure 4.8: The differential cross sections as a function of the polar emission angle of the proton-halo. The left plot gives $d\sigma/d\cos\theta$ when the polarization directions of the high-frequency laser wave and the γ-photon are orthogonal to each other, $\vec{E}_L \perp \vec{E}'$ (see Fig. 4.2); while the right plot gives $d\sigma/d\cos\theta$ when the x-axis is chosen along the "propagation direction of the laser wave" and the γ-ray, $\vec{E}_L \parallel \vec{E}'$ (see Fig. 4.3). The photon energies of the γ-ray and of the laser beam are held fixed at $\omega' = 3$ MeV and $\omega_L = 2$ keV, respectively.

In each plot, we compute $d\sigma/d\cos\theta$, where the electric field strength E_L is held fixed at 3.07×10^{13} V/cm as shown by the red curves. The corresponding laser intensity is indicated on each plot, the laser frequency and the γ-ray photon energy are held fixed as before. Both were compared with the dashed black curves, where the photonuclear process is induced without the assistance of the laser beam. We see that both curves practically superpose on each other (so that the dashed black curves are hardly visible), which means that the presence of the laser field in terms of very high intensity or orientation does not modify the angular distribution of the photoproton-halo. Apart from that, both differential cross sections tend to shift towards small ejection angles due to the strong dynamical influence of the incident γ-photon. Indeed, this behavior exhibits a clear analogy to situations reported by several authors in atomic physics [30, 32, 33].

In a second investigation of the angular proton distribution, we plot in Fig. 4.9 $d\sigma/d\cos\theta$ in term of $\cos\theta$ for one-, two- and three-photon absorption. The different input parameters and field geometries are shown on each plot. As we can see, the oscillation behavior of the angular distribution is strongly dependent on the arguments $\alpha_1^{\perp}$ and $\alpha_1^{\parallel}$ of the Bessel-function as given by Eqs. (4.7a) and (4.28), respectively. Because $p_x < p_z$, the right three plots where $\vec{E}_L \parallel \vec{E}'$, exhibit more oscillations than the left ones where $\vec{E}_L \perp \vec{E}'$, and this nonperturbative behavior arise from the large values of $\alpha_1^{\parallel}$ (from top to bottom we have found $\alpha_1^{\parallel} \approx 9.46,\ 4.73,\ 11.83$). The larger the argument α, the more sinusoidal the oscillations of the Bessel functions become.

On the other hand, the left three plots begin to oscillate (although weak compared with the right ones) at small emission angle θ, because the component p_x of the photoproton momentum is maximized when $\theta \to 0$. Another factor which leads to increase α_1, and hence the oscillation behavior of the angular distribution, is the ratio E_L/ω_L^2 as given by Eqs. (4.7a) and (4.28), which has the smallest value in the middle plots of Fig. 4.9. According to our calculations, we have found for $\vec{E}_L \perp \vec{E}'$ and from top to bottom that $\alpha_1^{\perp} \approx 1.04 \times 10^{-4},\ 5.2 \times 10^{-5}$ and 1.3×10^{-4} (i.e. $\alpha_1 \ll 1$), and this corresponds to the perturbative regime.

Thus, we can conclude from this comparison that, it is more difficult to gain informations about the probability for the photoproton to be emitted in a certain direction for copropagating linearly polarized laser and γ-ray photon than for orthogonally propagating ones. Further, the probability of inducing the photonuclear reaction (4.2) in the presence of the linearly polarized laser beam decreases by increasing the number n of absorbed laser photons, which means that the laser serves as an inhibitor (retarder) of the photoproton, and this effect becomes especially apparent when $\vec{E}_L \perp \vec{E}'$. This conclusion also agrees with various reports by the

authors cited above.

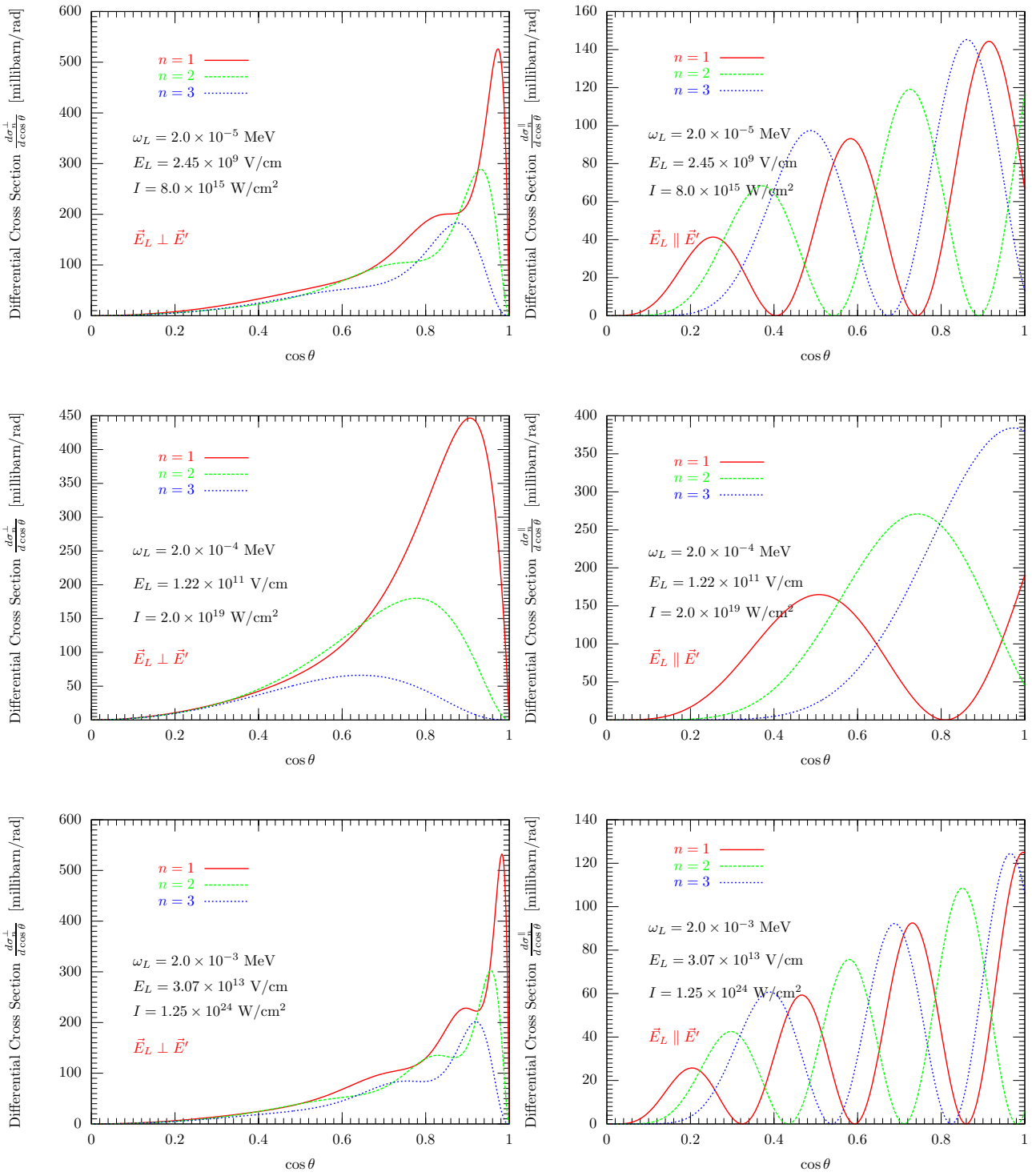

Figure 4.9: The angular distribution as a function of the polar emission angle of the photoproton-halo for one-, two- and three-photon absorption. The photon energies of the γ-ray is held fixed as before, and the laser parameters ω_L and E_L are indicated on each plot.

4.4.2 The case of circularly polarized laser beam

We now discuss the results obtained from the laser-assisted photonuclear reaction (4.2) when the laser wave is circularly polarized ($\delta_0 = 1$). Circular polarization of the laser wave leads to expressions for the cross sections and rates identical to those obtained for the linear polarization, except that the generalized Bessel-functions (4.12) are replaced by the ordinary Bessel-functions (B.3). In order to proceed with our discussion, we may consider again the two scenarios described in Figs.4.2 and 4.3.

(i) When $\vec{E}_L \perp \vec{E}'$, we replace the transition amplitude (4.17) by

$$\mathcal{M}_n \equiv \mathcal{M}_n^{\perp} = \vec{\varepsilon}\vec{p}\, B_n - ae\varepsilon_x\, C_n - ae\varepsilon_y\, D_n, \tag{4.35}$$

where the Fourier coefficients B_n, C_n and D_n are expressed in terms of the ordinary Bessel-functions of integer order n as follows

$$B_n = J_n(\alpha)e^{in\eta_0}, \tag{4.36a}$$

$$C_n = \frac{1}{2}\left[J_{n+1}(\alpha)e^{i(n+1)\eta_0} + J_{n-1}(\alpha)e^{i(n-1)\eta_0}\right], \tag{4.36b}$$

$$D_n = \frac{1}{2i}\left[J_{n+1}(\alpha)e^{i(n+1)\eta_0} - J_{n-1}(\alpha)e^{i(n-1)\eta_0}\right], \tag{4.36c}$$

and the argument α is given by

$$\alpha \overset{\text{def}}{=} \sqrt{\alpha_1^2 + \alpha_2^2} \equiv \alpha^{\perp} = \frac{eE_L}{\omega_L^2 m_{\rm p}}\tilde{p}, \tag{4.37a}$$

$$\tilde{p} = \sqrt{p_x^2 + p_y^2}, \tag{4.37b}$$

$$\eta_0 \equiv \eta_0^{\perp} = \arccos\left(\frac{p_x}{\tilde{p}}\right). \tag{4.37c}$$

(ii) When $\vec{E}_L \parallel \vec{E}'$, we replace the transition amplitude (4.17) by

$$\mathcal{M}_n \equiv \mathcal{M}_n^{\parallel} = \vec{\varepsilon}\vec{p}\, B_n - ae\varepsilon_y\, C_n - ae\varepsilon_z\, D_n. \tag{4.38}$$

Here the Fourier coefficients B_n, C_n and D_n have the same expressions as in Eqs. (4.36), but the argument α in Eqs. (4.37) should be replaced by

$$\alpha \overset{\text{def}}{=} \sqrt{\alpha_1^2 + \alpha_2^2} \equiv \alpha^{\parallel} = \frac{eE_L}{\omega_L^2 m_{\rm p}}\tilde{p}, \tag{4.39a}$$

$$\tilde{p} = \sqrt{p_y^2 + p_z^2}, \tag{4.39b}$$

$$\eta_0 \equiv \eta_0^{\parallel} = \arccos\left(\frac{p_y}{\tilde{p}}\right). \tag{4.39c}$$

Otherwise, all other derivations performed in Section 4.3 are mathematically identical.

For the presentation of numerical results we have chosen circularly polarized laser radiations with different frequencies and intensities, so varying from Ruby/HeNe up to VUV/XUV lasers. Concretely, we shall consider the following frequencies: $\omega_L = 2$, 20 and 200 eV, which correspond to wavelengths of $\lambda_L \approx 620$, 62 and 6.2 nm, respectively. The photon energy of the γ-ray is held fixed at 3 MeV as before.

In Fig. 4.10, we show the photoproton energy spectra in term of the number n of absorbed ($n > 0$) or emitted ($n < 0$) laser photons, where $\vec{E}_L \perp \vec{E}'$. The photoproton absorbs an amount of energy from the laser beam equal to $n\omega_L$. When the laser intensity varies between 10^{13} and 9×10^{13} W/cm^2, the shapes of the energy spectra show roughly similar behavior in comparison with the spectra obtained in Fig. 4.5. That is, the spectrum becomes broader by increasing the laser intensity and in each graph the total cross section remains constant at

roughly 67.6 mb. Furthermore, the sidebands in each energy spectrum become a bell-shaped distribution and each spectrum reaches its maximum value for $n = 0$, where the laser does not interact with the photoproton. Afterwards, it decreases with increasing the number of exchanged laser photons. This happens because we have found from Eq. (4.37a) that $1.15 \times 10^{-2} \leqslant \alpha_1^{\perp} \leqslant 5.7 \times 10^{-2}$, so that the approximation of $B_n(\alpha_1^{\perp})$, $C_n(\alpha_1^{\perp})$ and $D_n(\alpha_1^{\perp})$ in Eqs. (4.36) as $const \cdot (\alpha_1^{\perp})^n$ always holds. The larger the argument of the Bessel-functions, the less likely is the multiphoton proton emission process, and the coupling of the continuum photoproton to the low-frequency laser field is perturbative.

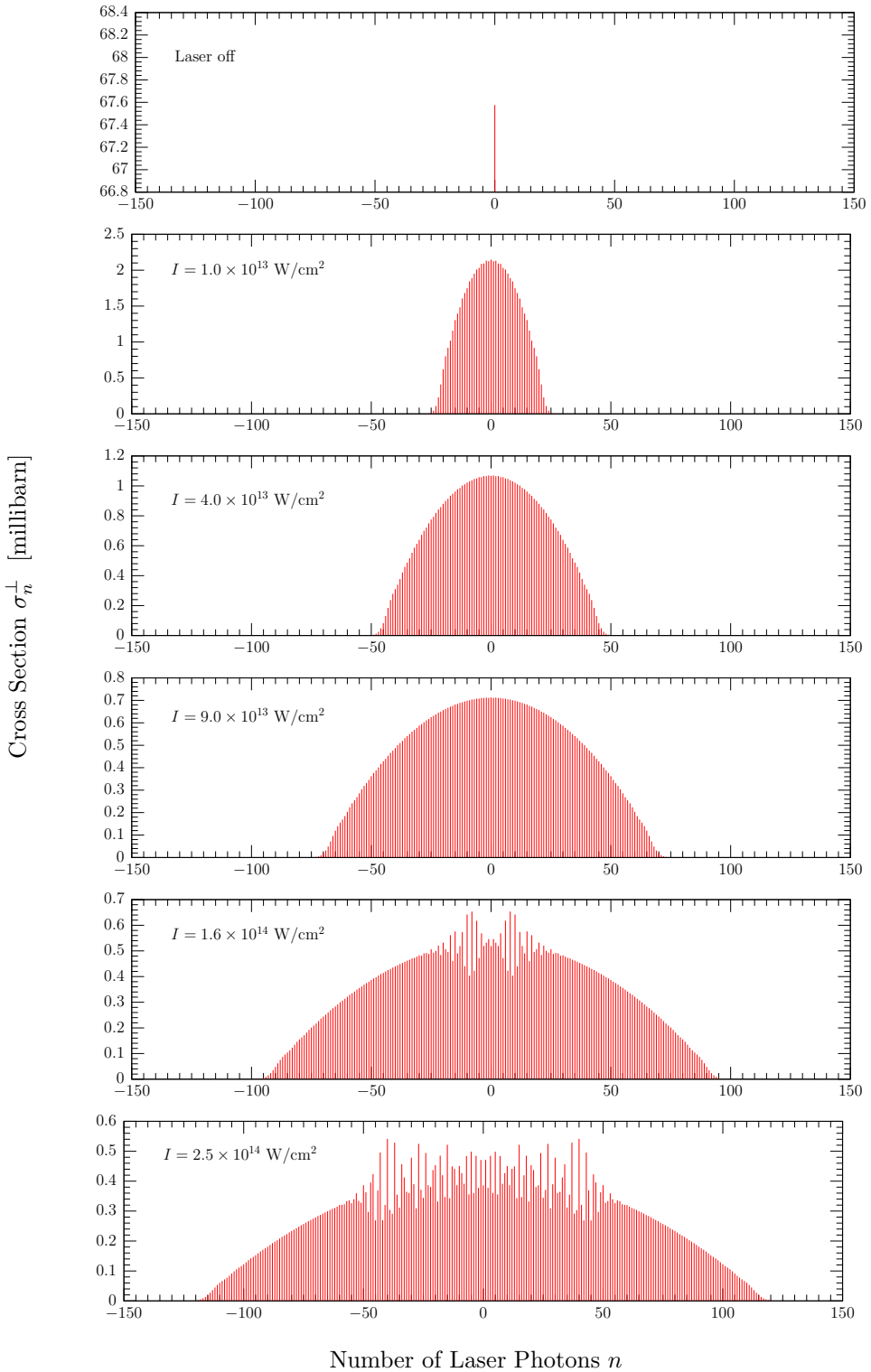

Figure 4.10: The energy distribution of the photoproton in term of the number of absorbed laser photons and for different values of the laser intensity. The electric field vectors of the laser and the γ-ray are perpendicular to each other, $\vec{E}_L \perp \vec{E}'$, as described by Fig. 4.2. Values of the photon energy of the γ-ray and of the laser field are held fixed at $\omega' = 3$ MeV and $\omega_L = 2$ eV, respectively. The laser's electric field strength is increased from top to bottom as follows: $E_L = 0.0,\ 6.1 \times 10^7,\ 1.22 \times 10^8,\ 1.84 \times 10^8,\ 2.45 \times 10^8$, and 3.07×10^8 V/cm. The corresponding laser intensities are indicated on each graph. The total cross section $\sigma^{\perp} = \sum_n \sigma_n^{\perp}$ remains unchanged in all graphs at roughly 67.6 mb.

However, above 1.6×10^{14} W/cm^2 and for $|n| < 50$ the sidebands in the photoproton energy spectrum exhibit drastic fluctuations (see the fifth and sixth graphs at the bottom of Fig. 4.10), which originate from the oscillating behavior of the Bessel-functions as $\alpha^{\perp}$ takes larger values. We note that the maximum value of $\alpha^{\perp}$ appears when $\theta \to \pi/2$ and from (4.37) we obtain: $\tilde{p} \to p_n$, so that

$$\alpha^{\perp} \longrightarrow \alpha^{\perp}_{\max} = \frac{eE_L}{\omega_L^2 m_{\mathrm{p}}} p_n \approx 946.3 \gg 1.$$

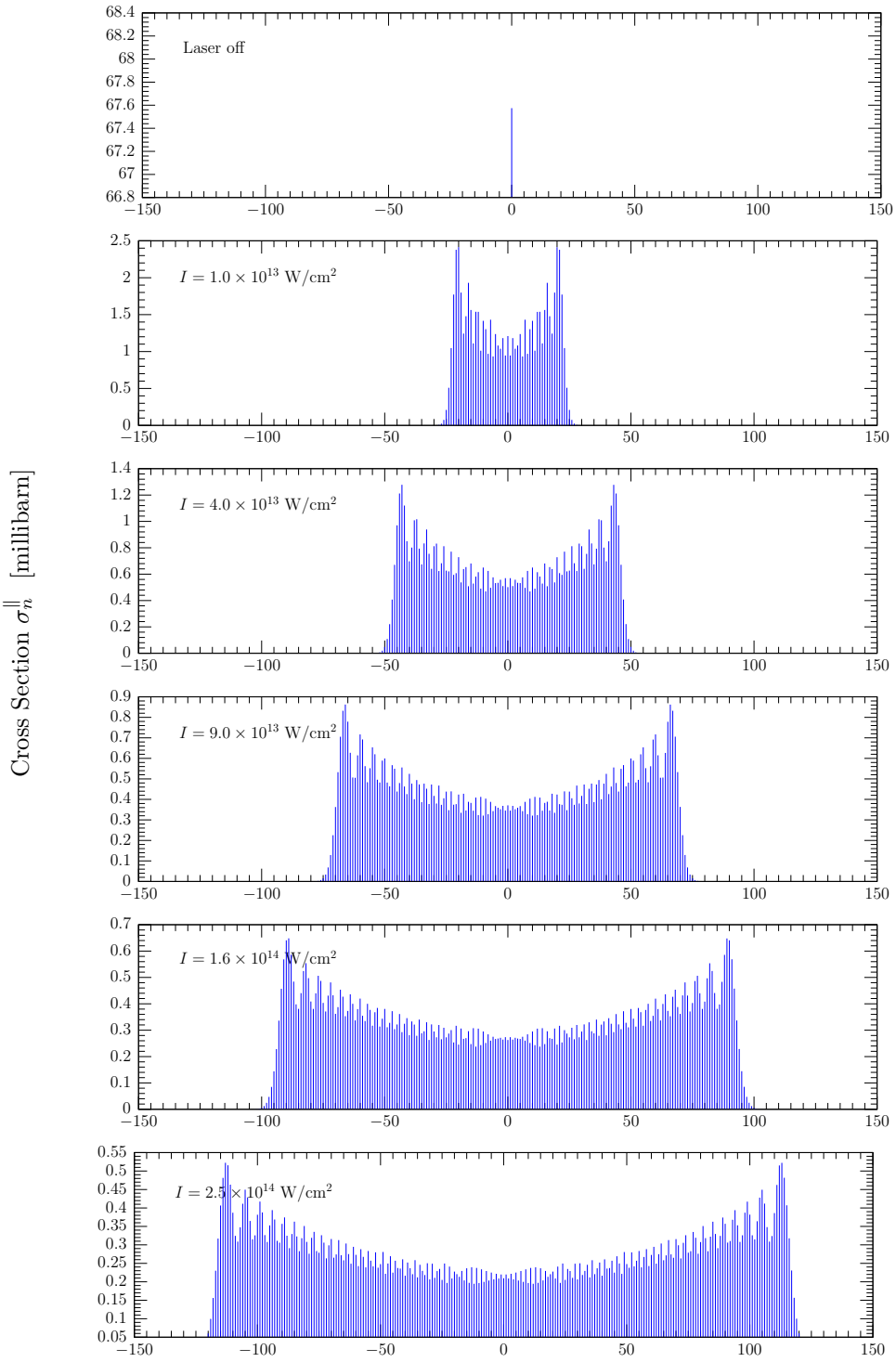

Figure 4.11: Same as Fig. 4.10, but $\vec{E}_L \parallel \vec{E}'$.

If we look at Fig. 4.11 in the case when $\vec{E}_L \parallel \vec{E}'$, we can see that the photoproton energy spectrum looks qualitatively different in comparison with that in Fig. 4.10. In fact, the spectrum becomes broader by increasing

the laser intensity (from top to bottom), and its height increases with increasing the number of exchanged laser photons. As a first conclusion we can say that the energy spectrum depends strongly on the direction of the photoproton motion with respect to $\vec{E}'$. In addition, the sidebands in Fig. 4.11 exhibit oscillation-like fluctuations when the laser intensity varies between 10^{13} and 2.5×10^{14} W/cm^2, and these fluctuations become apparent even between n and $n+1$ exchanged laser photons. This behavior can also be attributed to the large values of the arguments $\alpha^{\parallel}$ in Eq. (4.39a), which varies between 23.65 and 118.28. The larger the argument of the Bessel-functions, the more likely is the multiphoton proton emission process, which means that the coupling of the continuum photoproton to the low-frequency laser field is nonperturbative.

The increase of the sidebands in each energy spectrum with increasing n, which is more clearly seen in Fig. 4.11 than in Fig. 4.6, can be understood as follows: The photoproton is preferentially emitted parallel to $\vec{E}'$ where $\theta\to0$ due to the strong influence of the γ-photon's polarization. When $\vec{E}_L\parallel\vec{E}'$, the argument α of the Bessel-functions is maximized, since $|p_x|<|p_z|$ and hence, from Eqs. (4.37a) and (4.39a) we get $\alpha^{\perp}<\alpha^{\parallel}$. According to our calculations, values of the momentum components p_x, p_y and p_z of the photoproton are roughly 14.37, 6.70 and 71.56 MeVs, respectively, so that in total we have

$$\|\vec{p}\|\equiv\sqrt{p_x^2+p_y^2+p_z^2}\approx73.3\ \text{MeV}. \tag{4.40}$$

The total cross section remains unchanged at the value obtained previously for linearly polarized laser beam, i.e.

$$\sigma\equiv\sigma_{\text{circular}}=67.578\pm0.001\ \text{mb}=\sigma_{\text{linear}}. \tag{4.41}$$

We note that, in the case of two copropagating waves, the increase in the energy spectrum towards the side wings where the number n of exchanged photons is large has also been reported by Leone *et al.* [32]. In their study of two-frequency multiphoton ionization, an hydrogen atom is exposed to a combined field consisting of a low-frequency linearly polarized laser beam ($\omega_L\simeq1.17$ eV) and a high-frequency photons (50 eV $<\omega'<$ 100 eV). The initial state was the ground state of the hydrogen atom and the final state was the Coulomb-Volkov state [30, 32, 33]. This comparison should not be understood as a verification of the validity of our calculations or of others in atomic physics, because the energy levels and the physical mechanisms involved in the two processes are entirely different, but rather as a first step of the generalization of the strong-field approximation to laser-assisted processes from atoms to nuclei.

The comparison between Fig. 4.10 and Fig. 4.11 leads us to the following conclusions: Similarly to the case of linearly polarized laser field, the multiphoton character of the photonuclear reaction (4.2) in the halo-nucleus ${}^{A}_{Z}$[Xp] becomes apparent for copropagating circularly polarized laser and γ-ray photon. In contrast, single-photon character is apparent for orthogonally propagating laser and γ-ray photon. In both cases, multiphoton and single-photon characters, appear more clearly and rapidly by increasing the electric field strength, or equivalently the intensity of the circularly-polarized laser beam. However, this result is quite different to what we have seen before by comparing Fig. 4.5 with Fig. 4.6 in the case of linearly polarized laser: The difference between the multiphoton and the single-photon character becomes most apparent at higher intensities of the linearly-polarized laser, not at lower intensities. In general terms, we observed a strong effect of the orientation of the laser's electric field vector on the energy spectra of the photoproton-halo.

Let us now investigate the photonuclear reaction (4.2) by increasing the intensity of the circularly polarized laser beam. In the left three plots of Figure 4.12 where $\vec{E}_L\perp\vec{E}'$, we show the cross sections $\sigma_n^{\perp}$ of the photoproton as a function of the laser intensity for different numbers of absorbed laser photons. In the right three plots we show $\sigma_n^{\parallel}$ where $\vec{E}_L\parallel\vec{E}'$.

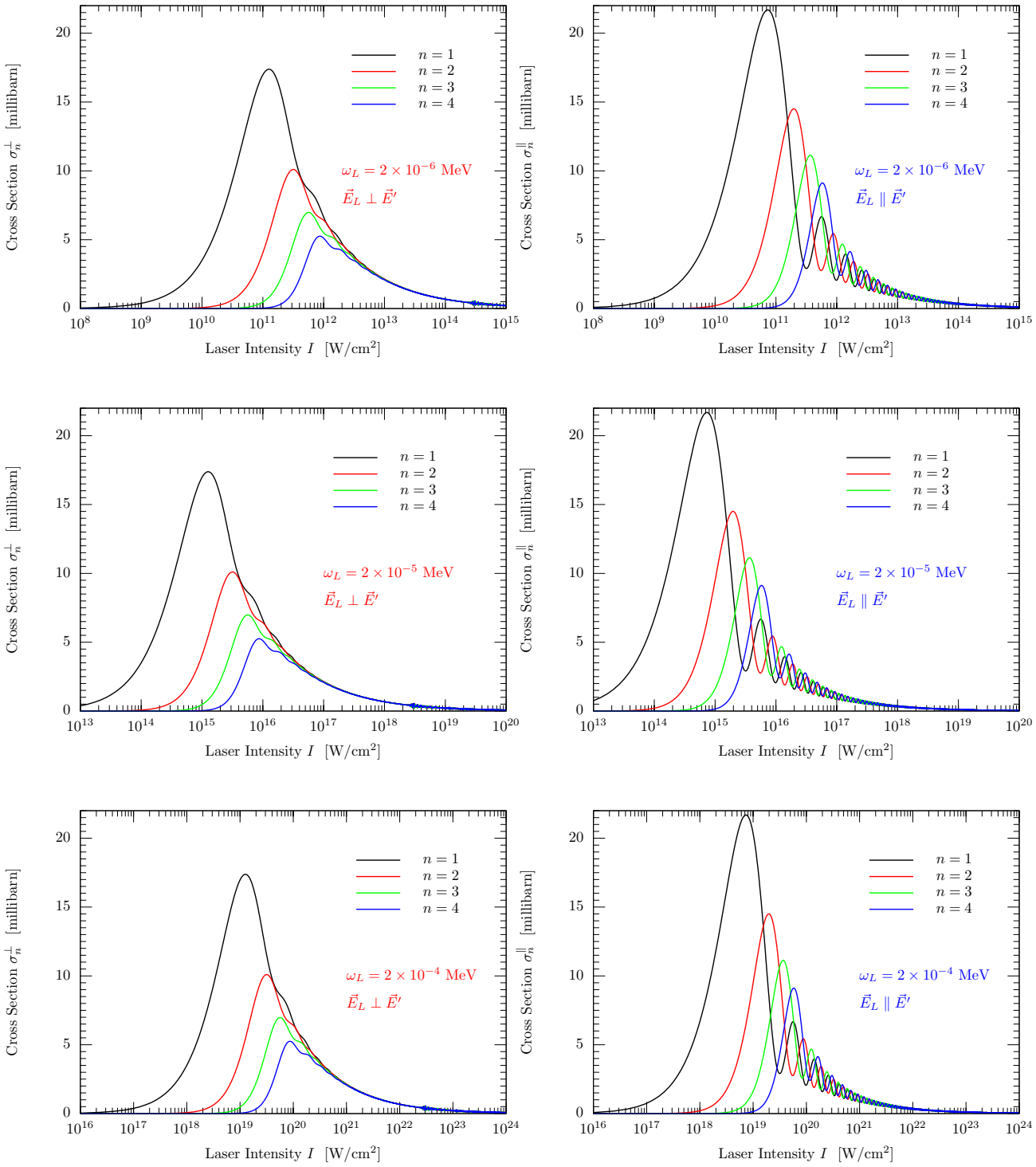

Figure 4.12: The cross sections $\sigma_n^{\perp}$ and $\sigma_n^{\parallel}$ of the photoproton as a function of the laser intensity for different numbers of absorbed photons ($n = 1, \ldots, 4$). The left plots give the cross section when $\vec{E}_L \perp \vec{E}'$ and the right ones when $\vec{E}_L \parallel \vec{E}'$. The photon energy of the γ-ray is held fixed at $\omega' = 3$ MeV and the laser frequency is increased from top to bottom as follows: $\omega_L = 2$, 20 and 200 eV.

When $\vec{E}_L \perp \vec{E}'$ and for one-photon absorption, the cross sections (see the solid black curves in the left plots) attain the same maximum value of

$$\sigma^{\perp}_{\max}[n=1,\text{circular}] \simeq 17.4 \text{ mb}. \tag{4.42}$$

That is, it remains unchanged by increasing the laser frequency from top to bottom as follows $\omega_L = 2$, 20 and 200 eV. The laser intensities corresponding to this maximum value are $I \approx 1.25\times10^{11}$, 1.25×10^{15} and 1.25×10^{19} W/cm^2. On the other hand, when $\vec{E}_L \parallel \vec{E}'$, we obtain a quite larger value of

$$\sigma^{\parallel}_{\max}[n=1,\text{circular}] \simeq 21.7 \text{ mb}, \tag{4.43}$$

and the laser intensities corresponding to this maximum cross section are quite smaller: $I \approx 7.3\times10^{10}$, 7.3×10^{14} and 7.3×10^{18} W/cm^2, as shown by the solid black curves in the right plots. Essentially the same remarks can be made for the cases when $(n=2,3,\ldots)$ photons from the laser are absorbed.
These results can be explained in a manner similar to that discussed in the previous Subsection regarding Fig. 4.7, which indicate that the photoproton is preferentially emitted parallel to $\vec{E}'$ due to the strong infulence of the γ-photon's polarization. When $\vec{E}_L \parallel \vec{E}'$, the argument α of the Bessel-functions is maximized, and hence, $\sigma^{\perp}_{\max} < \sigma^{\parallel}_{\max}$. According to our calculations, we have found that $1.5\times10^{-4} \leqslant \alpha^{\perp}_1 \leqslant 0.1$ and $0.3 \leqslant \alpha^{\parallel}_1 \leqslant 771.0$.

In order to ensure a fair comparison between circular and linear polarization, we have computed in Fig. 4.13 the photoproton cross sections σ_n with exactly the same input parameters for the laser and the γ-ray as in Fig. 4.7. We have found that values of both $\sigma^{\perp}_{\max}$ and $\sigma^{\parallel}_{\max}$ obtained in Eqs. (4.42) and (4.43), which also remain unchanged for $\omega_L = 2$ keV, are respectively larger by the factors 1.38 and 1.08, than those obtained previously in Eqs. (4.33) and (4.34), where the laser is linearly polarized.

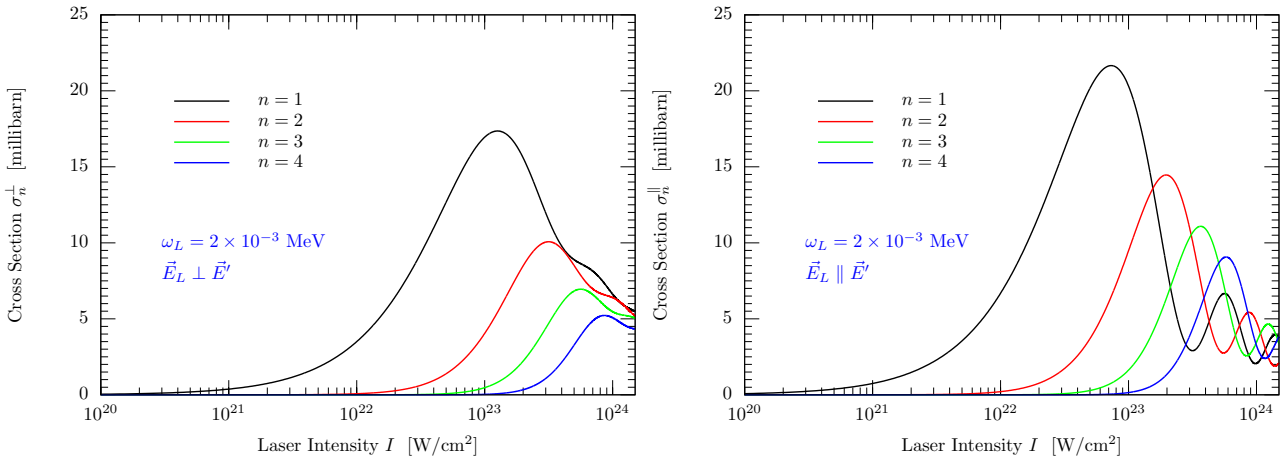

Figure 4.13: The cross section of the photoproton as a function of the laser intensity for different numbers of absorbed photons $(n=1,\ldots,4)$. The left plot gives the cross section when $\vec{E}_L \perp \vec{E}'$ and the right ones when $\vec{E}_L \parallel \vec{E}'$. The photon energies of the γ-ray and of the laser beam are held fixed at $\omega' = 3$ MeV and $\omega_L = 2$ keV, respectively. We compare this Figure with Fig. 4.7 to show the influence of linearly and circularly polarized laser on the photoproton cross section.

This means physically, that the probability of inducing the photonuclear reaction (4.2) by absorbing n-photons (with total energy $n\omega_L$) from a circularly polarized laser is higher than that from a linearly polarized laser. This result is in good agreement with experimental observations of Fox, Kogan and Robinson [143,144] in atomic physics, as they measured the total multiphoton ionization rates of atomic cesium by the simultaneous absorption of Ruby-laser photons. In addition, our result also agrees with perturbation theory calculations for weak couplings (see [145–147] and more recently in [148,149]), which indicate that circular polarization cross sections and rates are somewhat larger than for linear polarization due to the field correlation (photon statistics) effects in single-photon and multiphoton processes. We note, for example, that Lambropoulos [146] came to this

conclusion as he derived the rate of two-photon transition from the ground 1s to the 2s state in hydrogenlike atom interacting with plane waves, and found that the rates depend on the correlation function of the radiations field.

We further note that, the (decreasing) oscillation of the photoproton cross section above 10^{23} W/cm^2 becomes more apparent for circular than for linear polarization of the laser field. However, at low intensities below 10^{23} W/cm^2, there is no substantial influence of the laser polarization. This behavior is expected due to the p_y-contribution of the photoproton momentum in the argument α of the Bessel-functions when the laser is circularly polarized.

Now in Fig. 4.14 we plot $d\sigma/d\cos\theta$ as a function of the polar emission angle between 0 and π. The solid curves show $d\sigma/d\cos\theta$ where the azimuthal angle φ is integrated as usual from 0 to 2π, and summing over all numbers of absorbed laser photons. The dashed and the dot-dashed curves show $d\sigma/d\cos\theta$ where φ is held fixed first at 0 and then at π, respectively. These are divided by 2π in order to make a comparison with the differential cross sections shown by the solid curves. The laser's electric field strength is held fixed for all curves at 6.14×10^{12} V/cm, which corresponds to a laser intensity of 5×10^{22} W/cm^2.

When the photoproton is ejected at $\varphi = 0$, the total cross section is $\sigma \simeq 79.925$ mb, which is larger than the one obtained previously in Eq. (4.41). However, the cross section, or equivalently, the probability to eject the proton at $\varphi = \pi$ is quite smaller, since we obtained $\sigma \simeq 56.296$ mb. In these cases, the kinetic energy of the ejected photoproton-halo is about 2.913 MeV, which corresponds to a nonrelativistic momentum of 73.93 MeV and a velocity of 2.36×10^7 m/s. The left and right plots in Fig. 4.14 are quite similar, and this result confirms that the angular proton distribution depends neither on the polarization of the laser light, nor on the orientation of its electric field vector $\vec{E}_L$ with respect to that of the γ-photon, i.e. $\vec{E}'$.

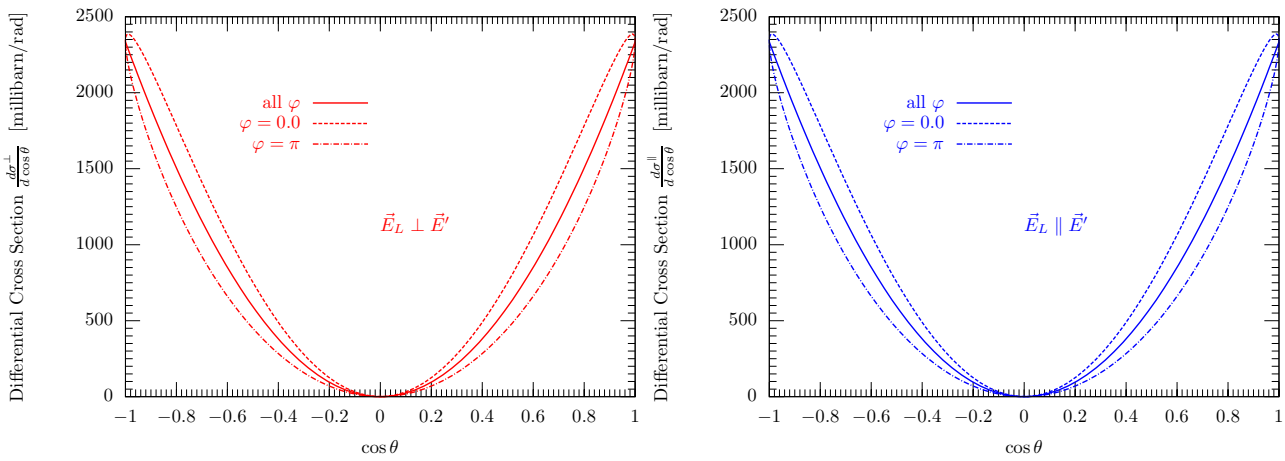

Figure 4.14: The differential cross sections as a function of the polar emission angle of the proton-halo. The left plot gives $d\sigma^\perp/d\cos\theta$ where $\vec{E}_L \perp \vec{E}'$; while the right one gives $d\sigma^\parallel/d\cos\theta$ when $\vec{E}_L \parallel \vec{E}'$. Both are divided by 2π. The photon energies of the γ-ray and of the laser beam are held fixed at $\omega' = 3$ MeV and $\omega_L = 2$ eV, respectively. The azimuthal angle of the ejected photoproton is held fixed at $\varphi = 0$ (dashed curves) and $\varphi = \pi$ (dot-dashed curves).

Finally, we show in Fig. 4.15 the angular distribution of the photoproton-halo by one-, two and three-photon absorption. Our aim here is to gain informations about the probability for the photoproton to be emitted in a certain direction when we know the number of absorbed laser photons, and also for given field configurations and strengths. This Figure is analogous to that presented in Figure 4.9 where the laser is linearly polarized.

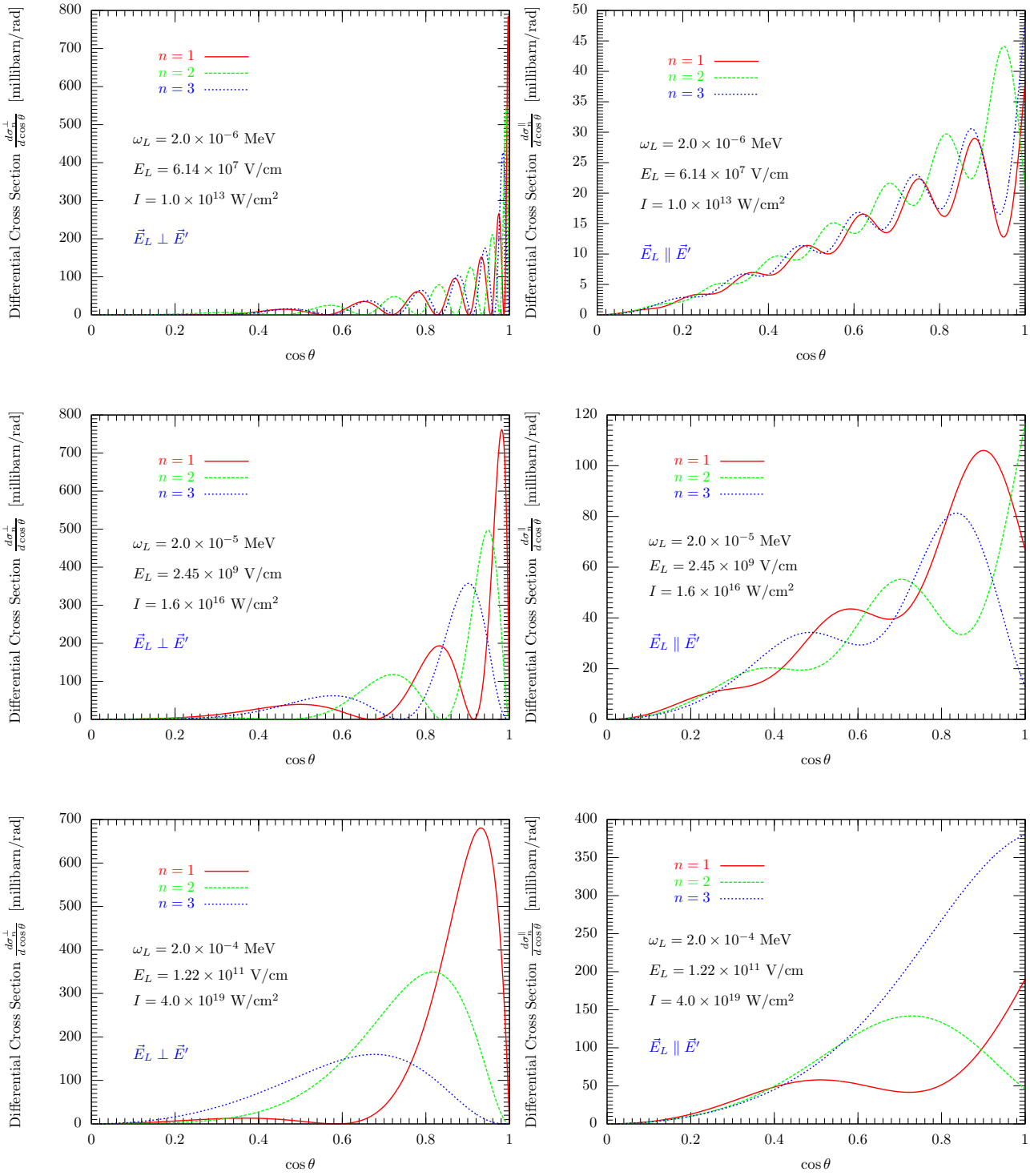

Figure 4.15: The angular distribution as a function of the polar emission angle of the photoproton-halo for one-, two- and three-photon absorption. The photon energies of the γ-ray is held fixed as before, and the input parameters ω_L and E_L of the circularly polarized laser are indicated on each plot.

In left three plots of Fig. 4.15, we see that for orthogonally propagating laser and γ-ray photon, the maxima of the differential cross sections are shifted toward smaller angle, and strongly oscillating near $\theta = 0$. These

behaviors arise from the rapid oscillations of the Bessel-functions for such field geometries, which means that the nonperturbative effects are dominant.

Furthermore, we see from top to bottom that $d\sigma^{\perp}/d\cos\theta$ increases with increasing the laser parameters ω_L and E_L. That is, the higher the energy of the incoming laser photons, the more likely the photoproton is emitted. On the other hand, the ratio E_L/ω_L^2 is maximized for the first left plot followed by the second one, and for this reason the first plot exhibits the strongest oscillations. Thus, we can say that the laser beam serves as an accelerator of the photoproton, and basically the same remarks can be made for $d\sigma^{\parallel}/d\cos\theta$.

It is also important to note that for copropagating laser and γ-ray photon (when $\vec{E}_L \parallel \vec{E}'$), the differential cross sections exhibit oscillating growth toward smaller angle, a phenomenon which is not observed when $\vec{E}_L \perp \vec{E}'$. Further, $d\sigma^{\parallel}/d\cos\theta$ shows a qualitative difference between linearly and circularly polarized laser at fixed input parameters ω_L and E_L. That is, we have oscillations like $f(x) \approx x + x \cdot \sin(x)$ for linear polarization and $f(x) \approx x^2 + (x \cdot \sin(x))^2$ for circular polarization (compare the right three plots in Figs. 4.9 and 4.15). Thus, we can conclude from these comparisons that single-photon and multiphoton angular distributions of the photoproton at a given proton energy depend strongly on the field geometries, polarizations and strengths.

–V–

Multiphoto-Production of Charged Pion Pairs on the Proton[1]

We have already studied in Chapter 4 the laser-assisted photonuclear effect in halo-nuclei. In this Chapter we shall deal with another high-energy process in intense light-matter interaction on the hadronic scale: the multiphoto-production of charged pion pairs, when a relativistic proton collides with an ultra-high laser beam.

5.1 Background and Motivations

Photoproduction of pion pairs on the proton has been studied extensively both in theory and experiment since the 1960s. In recent years the interest in the process has been revived by improved experimental data which were obtained by using polarized tagged photon beams at the MAMI Microtron [37, 38], the GRAAL facility [39–41], and the Jefferson Laboratory [42, 43]. At GRAAL, the high-energy photon beam is produced by Compton backscattering of laser light on a relativistic electron beam. These studies allow insights into the internal structure and excitation spectrum of the proton. A particular focus lies on polarization asymmetry measurements which are sensitive to interference cross terms. Photoproduction of neutral mesons in nuclear electric fields, known as the Primakoff effect [86, 87], was clearly observed at the Jefferson Laboratory [44]. This process could also give a direct evidence for the production of charged meson pairs ($\pi^+\pi^-, K^+K^-$), when high-energy photons interact with hadrons.

When charged particles interact directly with intense laser beams (rather than with single photons from synchrotron or Compton backscattering sources), multiphoton processes may arise involving the simultaneous absorption of more than one photon. Multiphoton e^+e^- pair production was observed in ultrarelativistic electron-laser collisions at SLAC [36] and theoreticians have studied related e^+e^- pair production processes by relativistic proton impact on intense laser beams [94–101]. In this setup, the laser frequency and field strength are largely Doppler-enhanced in the projectile rest frame. Inspired by the sustained progress in laser technology, very recently theoreticians started to study laser-induced $\mu^+\mu^-$ pair production in proton-laser collisions [100, 102, 103]. The apparent gap between the laser photon energy and the $\sim$ 100 MeV energy scale of the process can in principle be bridged by combining upcoming x-ray laser sources ($\omega_L^{\rm lab} \sim 10$ keV) with the ultrarelativistic proton beam at the LHC ($\gamma \approx 7000$) [150]. The Doppler-upshifted photon energies $\omega_L \approx 2\gamma\omega_L^{\rm lab} \sim 100$ MeV lie in the desired range. This effect is explained in more detail below. Large-scale [151, 152] as well as table-top [153] free-electron lasers (FELs) are currently being developed aiming at the generation of intense coherent x-ray pulses. Coherent x-rays are also envisaged via high-order harmonics from oscillating plasma surfaces [116] or atomic gas jets [117]. Such compact and portable x-ray sources hold the potential to be operated in conjunction with the LHC proton beamline.

In this Chapter, we propose a phenomenological model of $\pi^+\pi^-$ pair production by multiphoton absorption

[1] Chapter based on A. Dadi, C. Müller, Phys. Lett. B **697**, 142 (2011).

in ultrarelativistic proton-laser collisions, i.e. the reaction

$$p + n\omega_L \longrightarrow p^* + \pi^+ + \pi^-, \tag{5.1}$$

with the photon number $n \geq 1$ (see Fig. 5.1).

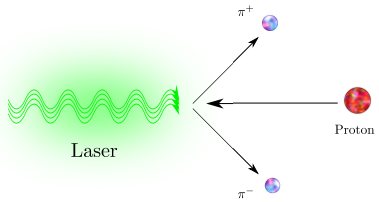

Figure 5.1: A simplified sketch of the $\pi^+\pi^-$ photoproduction through a head-on collision of an incident laser beam with an ultrarelativistic proton.

To this end, we combine the well-established approach to multiphoton processes in QED [45–47] with a simple phenomenological model to describe the pion-nucleon interaction. In general terms, the present study may be considered a first step towards an extension of the theory of laser-dressed QED into the realm of hadronic physics. More specifically, our main goals are

(i) to provide order-of-magnitude estimates for $\pi^+\pi^-$ multiphoto-production rates, demonstrating the observability of the process;

(ii) to compare with the corresponding rates for $\mu^+\mu^-$ production through the reaction

$$p + n\omega_L \longrightarrow p^* + \mu^+ + \mu^-, \tag{5.2}$$

and show that a range of laser frequencies exists where $\pi^+\pi^-$ production dominates over the (direct) production of muons; and

(iii) to discuss prospects why detailed investigations of multiphoto-production of pions might be useful.

We note that highly energetic reactions can also be induced indirectly when high-power laser pulses interact with solid targets. In the resulting plasma wakefields, electrons are accelerated to relativistic energies and emit secondary bremstrahlung γ-rays. These have led to the observation of photonuclear reactions [10–12] and efficient e^+e^- pair production through the Bethe-Heitler effect [14]. The setup also offers prospects for Bethe-Heitler creation of muon pairs [15] and single pion photoproduction through the reaction [16]

$$p + \gamma \longrightarrow n + \pi^+, \tag{5.3}$$

We point out that the latter process relies on single photo-absorption and does not exhibit the multiphoton character of the process studied below. Particle reactions such as $\mu^+\mu^-$ and $\pi^+\pi^-$ production were also considered in an e^+e^- plasma coupled to a photon field [17–20]. Single pion production in strong magnetic fields [154] and in collisions of laser-accelerated protons with nuclei have been studied theoretically as well [155].

5.2 Theoretical Framework

The aim of this theoretical part is to determine the cross section σ for reactions (5.1) and (5.2). This quantity is very important in hadronic physics that expresses the probability of such hadronic process occurring. We first briefly review the existing laser-dressed QED approach to muon pair production in the combined field consisting of an electromagnetic wave and an atomic nucleus [94–97, 100, 102, 103].

5.2.1 QED Description of Multiphoton Muon Pair Creation

Within the external-field approximation of QED, the Lagrangian density of the problem reads

$$\mathcal{L} = \overline{\psi}[i\gamma_\mu(\partial^\mu + ieA_L^\mu + ieA_C^\mu) - m]\psi, \tag{5.4}$$

where ψ is the bispinor field of $\mu^+\mu^-$ leptons; A_L^μ and A_C^μ are the four-potentials of the laser wave and the nuclear field, respectively, m and e are the muon mass and coupling constant. In the spirit of the Furry picture, one may split the total Lagrangian $\mathcal{L} = \mathcal{L}_V + \mathcal{L}_C$ into an unperturbed part

$$\mathcal{L}_V = \overline{\psi}(i\gamma_\mu D^\mu - m)\psi, \tag{5.5}$$

and a remaining interaction

$$\mathcal{L}_C = e\overline{\psi}\gamma_\mu A_C^\mu \psi. \tag{5.6}$$

Here, $D^\mu = \partial^\mu + ieA_L^\mu$ denotes the gauge covariant derivative with respect to the laser field where $\partial^\mu = \partial/\partial x_\mu$ and $x \equiv x^\mu \equiv (t, \vec{x})$. The laser field is assumed to be a monochromatic plane wave with the four-potential given by Eq. (3.7). For $\delta_0 = \pm 1$, the amplitude of the vector potential (3.7) is given by the two constant four-vectors $a_1^\mu = (0, a, 0, 0)$ and $a_2^\mu = (0, 0, a, 0)$ perpendicular to each other, which means that the wave propagates along the z-axis with the vector $k_L^\mu \equiv (\omega_L, \vec{k}_L) = \omega_L(1, 0, 0, 1)$. Further, the square of the averaged value of $A_L^\mu(k_L x)$ is

$$\overline{A_L^2} = -\frac{a^2}{2}(1 + \delta_0^2),$$

and the laser phase is given by

$$k_L x = k_L^\mu x_\mu = \omega_L \cdot (t - z),$$

with

$$k_L^2 = k_L A_L = k_L a_1 = k_L a_2 = a_1 a_2 = 0.$$

The field theory of $\mathcal{L}_V$ in Eq. (5.5) can be solved exactly by the so-called Dirac-Volkov states $\psi_{p_\pm, s_\pm}$ which include the interaction of the leptons with the plane-wave laser field up to all orders [156]. The leptons are characterized by their four-momenta $p_\pm^\mu$ and spin projections $s_\pm$ outside the laser field. The Dirac-Volkov solutions may be used as basis states in perturbative calculations with respect to the remaining Coulomb interaction with the nucleon. As a result, the leading-order S-matrix element for multiphoton muon pair production on a proton at rest reads

$$S_{\mu^+\mu^-} = i \int d^4x \; \overline{\psi}_{p_-, s_-}(x)\gamma^0 \psi_{p_+, s_+}(x) V_C(x), \tag{5.7}$$

where

$$V_C(x) = eA_C^0(x) = \frac{e^2}{4\pi|\vec{x}|} \tag{5.8}$$

denotes the Coulomb potential energy in this frame and γ^0 is a Dirac matrix. Although the laser field is treated as a classical electromagnetic wave, photons arise from a mode expansion of the oscillatory parts in the S-matrix (5.7) which contains multiphoton processes of arbitrary order as given by Eq. (4.10). The $\mu^+\mu^-$ production rate is obtained from (5.7) as

$$R_{\mu^+\mu^-} = \int \frac{d^3\vec{p}_+}{(2\pi)^3} \int \frac{d^3\vec{p}_-}{(2\pi)^3} \sum_{s_+, s_-} |S_{\mu^+\mu^-}|^2. \tag{5.9}$$

The cross section of the QED reaction (5.2) may be obtained by dividing out the photon flux $\Phi = \omega_L a^2/4\pi$ of the classical wave.

A few additional remarks are in order here.

1. For a proper description of muon pair production in the field of a heavy nucleus, the finite nuclear extension needs to be taken into account in general [102, 103]. Here we restrict our consideration to protons as projectiles, which may be treated as pointlike [see Eq. (5.8)] to a good approximation.

2. Being interested in order-of-magnitude estimates for the production rates, the recoil suffered by the proton during the process is ignored for simplicity.

3. We will consider x-ray laser fields where the value of the Lorentz-invariant parameter $\xi_\mu = ea/m$ is much smaller than unity. In this regime of laser-matter coupling, a process involving n photons could, in principle, be calculated within n-th order of perturbation theory in the photon field. We find it more convenient, however, to work within the framework of laser-dressed QED.

5.2.2 Effective Hadronic Model of Multiphoton Pion Pair Production

Theoretical studies of meson photoproduction off nucleons has been made since the 1960's and many theoretical problems were solved along the way. Most of the models used are phenomenological, which are based on effective Lagrangians for the meson-nucleon interaction [157] or dynamical models using effective Hamiltonian approaches [158–161]. Among them we also cite the unitarized pole models for pion photoproduction and πN scattering, which incorporate the current-algebra low-energy theorems [162–164]. Some authors [165, 166] presented a phenomenological fit of the data on single-pion photoproduction, whereby the photoproduction amplitude consists of the Born approximation and the standard Breit-Wigner parametrization for the resonance contributions taken from pion-nucleon scattering data. Aznauryan [167] includes the so-called "*Regge-poles*" amplitudes to the Breit-Wigner parametrization of resonance contributions in order to take into account the exchange of heavier mesons. Others authors [168] extended the study of pion photoproduction to Kaon and η mesons by combining the low energy QCD Lagrangian and the quark model.

In the phenomenological models of $\pi^+\pi^-$ photoproduction, which are based on effective Lagrangians for the pion-nucleon interaction, it was found that a proper description of the process requires the inclusion of more than 40 Feynman graphs (see, for example, [157] and references therein). In the present case of interest, where the pions are created by the absorption of more than one photon, the number of relevant Feynman diagrams increases tremendously, which renders a consideration on this level almost prohibitorily involved. However, order-of-magnitude estimates for $\pi^+\pi^-$ multiphoto-production rates may be obtained by applying the following model.

We consider a charged pion of rest mass m_π and free four-momentum $p^\mu = (p^0, \vec{p})$ moving in the potential of combined ultra-strong laser and nuclear Coulomb fields. The corresponding laser four-potential in the radiation gauge is given by Eq. (3.7). We first have to formulate the S-matrix elements to obtain the total and differential cross sections for the pair production process, i.e. for the reaction (5.1). Thereby, we shall take into account the underlying structure of pions from quarks and gluons, since the latter interact not only through the strong forces (with each other) but also through the electromagnetic forces. This is the first major difference between the study of lepton- and meson pair production. We therefore use the exact Volkov-solutions of the equation of motion for composite and spin-zero particles in an external electromagnetic field calculated in Subsection 3.2.3 of Chapter 3.

Before we begin to formulate the S-matrix, let us give an estimate of how high the frequency and the intensity of the laser field should be to induce the reaction (5.1). We define the coupling parameter ξ between the laser beam of electric field strength $E_L = a\omega_L$ and a given charged particle of mass m by

$$\xi = ea/m = eE_L/(m\omega_L).$$

Pair production via absorption of few high-frequency photons with $\omega_L \leqslant m$ takes place when $\xi \ll 1$, while for $\xi \gg 1$ and $E_L \ll E_L^{cr}$ the pair production is a tunneling process. Here E_L^{cr} is the critical field strength for pair production via the Schwinger process. In the tunneling process of $\pi^+\pi^-$ (or equivalently e^+e^-), the laser's electric field strength should be high enough that it can spontaneously tunnel virtual $\pi^+\pi^-$ (e^+e^-) pairs, out of the QCD (QED) vacuum, into real $\pi^+\pi^-$ (e^+e^-) pairs. In that case, values of E_L^{cr} can be estimated

by considering that the work produced by the laser field on one of these particles over a reduced Compton wavelength $\lambda\!\!\!^{-}_C$ must be equal to m, $eE_L^{cr} \cdot \lambda\!\!\!^{-}_C \stackrel{!}{=} m$. Since $\lambda\!\!\!^{-}_C = 1/m$, we then obtain for e^+e^- pairs

$$E^{cr}_{e^+e^-} = \frac{m_e^2}{e} \approx 0.862 \text{ MeV}^2 \approx 1.323 \times 10^{16} \text{ Volt/cm}, \tag{5.10a}$$

which corresponds to a critical intensity in QED of

$$I_{\rm QED} = (E_L^{cr})^2 \simeq 0.74 \text{ MeV}^4 \approx 4.65 \times 10^{29} \text{ W/cm}^2. \tag{5.10b}$$

For $\pi^+\pi^-$ we deduce

$$I^{cr}_{\pi^+\pi^-} \equiv I_{\rm QCD} = \left(\frac{m_\pi}{m_e}\right)^4 I_{\rm QED} \approx 4 \times 10^{-3} \text{ GeV}^4 = 2.5 \times 10^{39} \text{ W/cm}^2. \text{ (!)} \tag{5.11}$$

These very high values, both for QED and QCD, required to achieve directly the phenomenon of vacuum pair production is a main obstacle to the experimental realization and verification of the theories. The second critical field intensity in Eq. (5.11) is out of reach, but the first one in Eq. (5.10b) may be achieved indirectly in the nuclear rest frame of a target nucleus, when it moves with a relativistic velocity and colliding head-on with a high-frequency laser beam. For example, in a head-on collision geometry, when the laboratory values of the laser photon energy is around $\omega_L^{\rm lab} \simeq 10$ keV, the electric field strength $E_L^{\rm lab} \simeq 2 \times 10^{12}$ V/cm and, on the other hand, when a proton moves with a Lorentz factor of $\gamma \approx 7000$, then the laboratory values of both the laser field strength and frequency will be enhanced by a factor $(1+\beta)\gamma$ in the proton rest frame due to the relativistic Doppler effect, leading to $E_L \approx 3.6 \times 10^{16}$ V/cm and $\omega_L \approx 140$ MeV $\approx m_{\pi^\pm}$ in this frame. In that situation, nonlinear hadronic and QED processes can well occur. The presence of such ultra-strong laser field in the proton rest frame can polarize the QCD vacuum, from which virtual $\pi^+\pi^-$ (or evidently e^+e^-) pairs can be created. The sufficient energy is imparted into the QCD vacuum to bridge the energy gap to the positive-energy continuum, and hence creating real pions.

In principle, the pion energy scale can be achieved experimentally by a combination of an x-ray free electron laser (e.g. the XFEL at DESY or the LCLS at SLAC) with an ultrarelativistic proton beam as at the LHC in CERN. Also efforts are undertaken to develop tabe-top x-ray laser devices, which could be operated in conjunction with the LHC [169]. We remind that the currently highest laser frequency in the world is about 1 keV produced by the LCLS at SLAC, and in the future coherent frequencies up to 10 keV may be achieved.

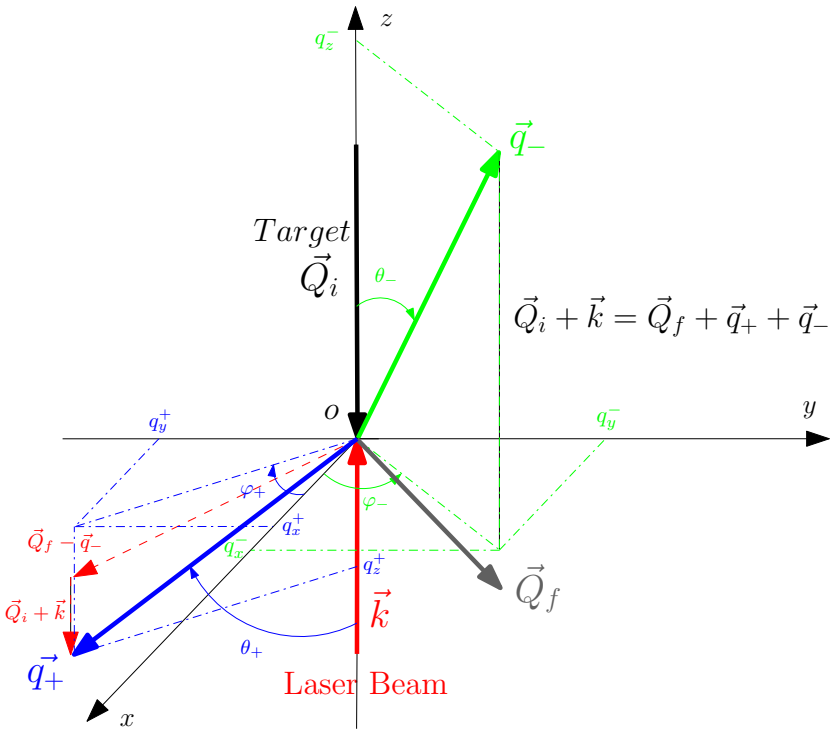

Figure 5.2: A head-on collision in the laboratory system of the incident laser beam (red) with an ultrarelativistic proton beam (black) creating a π^+ (blue) and π^- (green) particle pair.

In the following calculations, $\pi^+\pi^-$ pairs are created by a head-on collision of the laser wave with an ultrarelativistic proton of electric charge $|e|$ and intial four-momentum $Q_i^\mu = (Q_i^0, \vec{Q}_i)$ moving at $\gamma \approx 7000$, as shown in Figure 5.2. After the interaction, the laser dressed four-momentum of the proton becomes $Q_f^\mu = (Q_f^0, \vec{Q}_f)$ and the momentum transfer to the proton is $Q^\mu = Q_i^\mu - Q_f^\mu = (Q^0, \vec{Q})$. We point out that the proton is treated as an external potential which will be specified later, not as a quantum particle. The dynamics of the created pions is described by the following covariant Lagrangian density up to second order in $F_{\mu\nu}$ [123]

$$\mathcal{L} = \mathcal{L}_0 + \mathcal{L}_{\rm had} = (D_\mu\phi)^* (D^\nu\phi) [\delta_{\mu\nu} - \mathcal{K}_{\mu\nu}] - m_\pi^2 \phi\phi^* + \mathcal{L}_{\rm had}, \tag{5.12}$$

which includes the unperturbed part $\mathcal{L}_0$ as given by Eq. (3.8). Here $\phi \equiv \phi_-(x) = (\phi_1 - i\phi_2)/\sqrt{2}$ denotes the scalar π^--meson field and $\phi^* \equiv (\phi_1 + i\phi_2)/\sqrt{2}$ its complex conjugate. The complex structure of the produced pions is taken into account by including their electric and magnetic polarizabilities λ_e and λ_m. The experimental value $\lambda_e + \lambda_m \approx 0.16 \times 10^{-4}$ fm^3 has recently been measured in Primakoff scattering of high-energy pions with the COMPASS spectrometer at the Super Proton Synchrotron (SPS) in CERN in 2004 [170], (see also [171]). Theoretically, λ_e and λ_m can be calculated in the framework of effective field theory models, such as the non-perturbative QCD or the linear σ-model.

Similarly as in Subsection 5.2.1, we decompose the Lagrangian density (5.12) into an unperturbed part $\mathcal{L}_0 \equiv \mathcal{L} - \mathcal{L}_{\rm had}$ and a remaining interaction $\mathcal{L}_{\rm had}$. The field theory of $\mathcal{L}_0$, which contains the electromagnetic coupling of the $\pi^+\pi^-$ mesons to the laser field, can be solved exactly as presented in Subsection 3.2.2. Namely, we use the Hamilton's principle of least action (i.e. the Euler-Lagrange equations, Eq. (3.10)) with respect to $\phi(x)$ and $\phi^*(x)$ to derive the equations of motion of the $\pi^+\pi^-$ meson pairs. Thus, similarly to Eq. (3.11) we obtain

$$D_\mu D^\mu \phi(x) - D_\mu \left[\mathcal{K}_{\mu\nu} \left(D_\nu \phi(x)\right)\right] + m_\pi^2 \phi(x) = 0, \tag{5.13a}$$

$$D_\mu^+ D_+^\mu \phi^*(x) - D_\mu^+ \left[\mathcal{K}_{\mu\nu} \left(D_\nu^+ \phi^*(x)\right)\right] + m_\pi^2 \phi^*(x) = 0, \tag{5.13b}$$

with[2] $D_\mu^+ = \partial_\mu - ieA_\mu$.

[2] To simplify the notations, we leave out again the subscript L from the laser vector potential ($A_L^\mu \to A^\mu$).

Now, taking the approximations made for the laser vector potential (3.7) into account (i.e. the Lorentz gauge and the boundary conditions), and following exactly the same derivations as those of the previous Subsection 3.2.2, Eqs. (5.13) give two normalized solutions generalizing the known Volkov-Gordon states for the charged π^- and π^+ mesons in the presence of the laser wave in a normalizing volume V. These solutions correspond to positive and negative energies at $t \to \pm\infty$, respectively

$$\phi_-(x) = \frac{1}{\sqrt{2Vq_-^0}} \cdot \exp\left[i(p_-x) - i\int_{-\infty}^{kx} \left(\frac{e(p_-A)}{(kp_-)} + \frac{e^2A^2}{2(kp_-)} - \frac{\lambda_e+\lambda_m}{2m_\pi}(kp_-)\left(\frac{\partial A_\nu}{\partial\eta}\right)^2 \right) d\widetilde{\eta} \right], \tag{5.14a}$$

$$\phi_+(x) = \frac{1}{\sqrt{2Vq_+^0}} \cdot \exp\left[-i(p_+x) - i\int_{-\infty}^{kx} \left(\frac{e(p_+A)}{(kp_+)} - \frac{e^2A^2}{2(kp_+)} + \frac{\lambda_e+\lambda_m}{2m_\pi}(kp_+)\left(\frac{\partial A_\nu}{\partial\eta}\right)^2 \right) d\widetilde{\eta} \right]. \tag{5.14b}$$

The quantity q_-^0 (q_+^0) in Eqs. (5.14) denotes the time component of an effective momentum of π^- (π^+) in the laser field, which is defined by[3]

$$q^\mu \stackrel{\text{def}}{=} p^\mu + \frac{a^2}{4(kp)}\left(e^2 - \frac{\lambda_e+\lambda_m}{m_\pi}(kp)^2 \right)(1+\delta_0^2)k^\mu, \tag{5.15a}$$

and we have well $kq = kp$. The square of q^μ gives the square of an *effective pion mass*

$$q^2 \stackrel{\text{def}}{=} m_\pi^{*2} = m_\pi^2(1+\xi^2),$$

which is related to an *effective*[4] dimensionless Lorentz-invariant intensity parameter of the laser field

$$\xi \stackrel{\text{def}}{=} \frac{a}{m_\pi\sqrt{2}} \cdot \sqrt{\left(e^2 - \frac{\lambda_e+\lambda_m}{m_\pi}(kp)^2 \right)(1+\delta_0^2)}. \tag{5.15b}$$

This is an expression of the fact that the *quivering motion* forced upon the π^+ and π^- mesons by the presence of the laser wave increases its inertia, and then leads to a higher effective mass m_π^*. The latter can be interpreted as a mass shift of $\pi^+\pi^-$ mesons due to the electromagnetic pion-laser coupling as well as to the pion polarizablities. The gauge potential A_L^μ in (3.7) couples directly to the $\pi^\pm$ meson current density, as expressed by Eq. (3.17)

$$j_\mu(x) \equiv -i\left(\frac{\partial\mathcal{L}}{\partial(\partial_\mu\phi)}\phi - \frac{\partial\mathcal{L}}{\partial(\partial_\mu\phi^*)}\phi^* \right) = \frac{1}{Vq^0}\left[p_\mu + eA_\mu - \left(\frac{e(pA)}{(kp)} + \frac{e^2A^2}{2(kp)} - \frac{\lambda_e+\lambda_m}{2m_\pi}(kp)\left(\frac{\partial A_\alpha}{\partial\eta}\right)^2 \right) k_\mu \right].$$

Let us now focus on the pion-proton and the pion-laser interactions. The term $\mathcal{L}_{\text{had}}$ in Eq. (5.12) represents the hadronic interaction between the pion and the proton. In the present model, this interaction is assumed to be mediated by the exchange of the isoscalar-scalar σ meson of mass m_σ and coupling constant g_σ, which is described by the following Yukawa-type potential

$$V_{\text{had}}(x) = \frac{g_\sigma^2}{4\pi}\frac{\mathrm{e}^{-m_\sigma|\vec{x}|}}{|\vec{x}|}. \tag{5.16}$$

[3] Here also we simplify the notations by leaving out the "±" sign from p^μ and q^μ.
[4] We have introduced this word because of the momentum dependence of ξ.

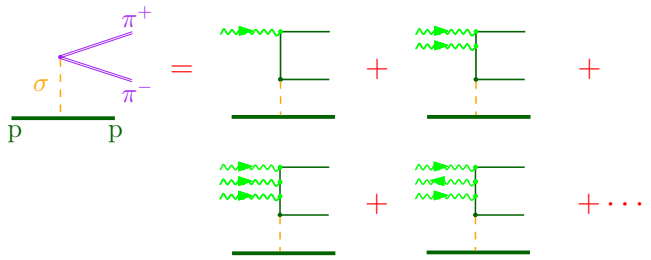

Figure 5.3: Graphical equation in terms of Feynman diagrams for laser-induced multiphoto-production of $\pi^+\pi^-$ pairs on the proton. In the present model, the pion-proton coupling is mediated by σ meson exchange, described by the Yukawa-type potential (5.16). The pion-laser interaction is accounted for to all orders by using the Gordon-Volkov states (5.14). They are indicated by the double lines in the Furry-Feynman diagram on the left-hand side of the equation, which corresponds to the amplitude (5.17).

The latter models the pion-proton interaction via σ meson exchange [172, 173]. It reflects the short-range nature of the hadronic interaction, which represents an essential difference with the long-range Coulomb potential (5.8) ($\propto 1/|\vec{x}|$). The squared coupling constant g_σ in Eq. (5.16) may be viewed as the product of the σ-meson coupling constants to the proton and the pion, $g_\sigma^2 = g_{\sigma\mathrm{pp}} g_{\sigma\pi\pi}$. In our model, g_σ is considered as a free parameter whereby we determine its numerical value by taking reference to the available experimental data on $\pi^+\pi^-$ production by single-photon absorption on the proton. The interaction of the pions with the laser field is accounted for to all orders by using the Gordon-Volkov states (5.14). When the pion-laser coupling parameter is small, $\xi = ea/m_\pi \ll 1$, a perturbative expansion into ordinary Feynman diagrams may be performed. Some typical low-order terms are shown on the right-hand side of the equation, with the wavy lines symbolizing the absorbed (or emitted) laser photons (see Fig. 5.3).

The leading-order S-matrix element for $\pi^+\pi^-$ multiphoto-production on the proton in the presence of the intense laser field may be written as (B.1).

$$S^{(1)}_{\pi^+\pi^-} = i \int d^4x \, \left(\phi_-^* \overleftrightarrow{\partial_t} \phi_+\right) V_{\mathrm{had}}(x) = i \int dx^0 d^3\vec{x} \left(\phi_-^* \left(\partial_t \phi_+\right) - \phi_+ \left(\partial_t \phi_-^*\right)\right) V_{\mathrm{had}}(x). \tag{5.17}$$

Before we proceed, we have to specify the polarization of the laser beam; we assume the latter to be circularly polarized, i.e. $\delta_0 = 1$. Inserting the wave functions (5.14) into Eq. (5.17) yields

$$S^{(1)}_{\pi^+\pi^-} = \frac{i}{2V\sqrt{q_-^0 q_+^0}} \cdot \int d^4x \; V_{\mathrm{had}}(\vec{x}) \Big[- i \left(q_-^0 - q_+^0\right) + i\omega_L \beta_1 \cos(\eta) + i\omega_L \beta_2 \sin(\eta) \Big] \times$$
$$\exp\left[-i \left(q_-^\mu + q_+^\mu\right) x_\mu + i\alpha_1 \sin(\eta) - i\alpha_2 \cos(\eta)\right], \tag{5.18}$$

where (B.2)

$$\alpha_j = \left[\frac{(a_j p_-)}{(k p_-)} - \frac{(a_j p_+)}{(k p_+)}\right] \cdot e, \tag{5.19a}$$

$$\beta_j = \left[\frac{(a_j p_-)}{(k p_-)} + \frac{(a_j p_+)}{(k p_+)}\right] \cdot e, \tag{5.19b}$$

for $j = 1, 2$. Here, p_- and p_+ stand for the free four-momentum of π^- and π^+ with positive and negative energy, respectively, when the external laser field is turned off. For further evaluation of the $S^{(1)}_{\pi^+\pi^-}$-matrix elements, we can expand analytically all periodic terms of Eq. (5.18) into Fourier series and compute their coefficients B_n, C_n and D_n using ordinary Bessel-functions of integer order n, we obtain (B.2)

$$S^{(1)}_{\pi^+\pi^-} = \frac{i}{2V\sqrt{q_-^0 q_+^0}} \cdot \sum_{n \geq n_0}^{+\infty} \mathcal{M}_n \int d^4x V_{\mathrm{had}}(\vec{x}) \exp\left[-i \left(q_-^\mu + q_+^\mu - n k^\mu\right) x_\mu\right]. \tag{5.20}$$

Here the *reduced* transition amplitude $\mathcal{M}_n$ of the process is expressed as follows

$$\mathcal{M}_n = i \left(q_+^0 - q_-^0\right) B_n + i\omega_L \beta_1 C_n + i\omega_L \beta_2 D_n,$$

with

$$B_n = J_n(\alpha)e^{-in\eta_0}, \tag{5.21a}$$

$$C_n = \frac{1}{2}\left[J_{n-1}(\alpha)e^{-i(n-1)\eta_0} + J_{n+1}(\alpha)e^{-i(n+1)\eta_0}\right], \tag{5.21b}$$

$$D_n = \frac{1}{2i}\left[J_{n-1}(\alpha)e^{-i(n-1)\eta_0} - J_{n+1}(\alpha)e^{-i(n+1)\eta_0}\right], \tag{5.21c}$$

and $\alpha_1 = \alpha\cos\eta_0$, $\alpha_2 = \alpha\sin\eta_0$ and $\alpha := \sqrt{\alpha_1^2+\alpha_2^2}$ are the arguments of the ordinary Bessel-functions. The integer n_0 in Eq. (5.20) denotes the minimum number of photons needed from the laser field to produce the $\pi^+\pi^-$ pairs. In order that reaction (5.1) may take place, the absorbed photon energy $n\omega_L$ in the nuclear rest frame must be greater than or equal to the rest energy of the created pairs in the final state, that is

$$n\omega_L \geq m^*_{\pi^-} + m^*_{\pi^+} \quad \Longrightarrow \quad n_0 = \text{floor}\left[\frac{2m^*_{\pi^\pm}}{\omega_L}\right] + 1 \tag{5.22a}$$

and then we can get

$$\text{p} + n\omega_L \longrightarrow \text{p}^* + \pi^- + \pi^+ \quad \text{for } n \geq n_0. \tag{5.22b}$$

The integral of the exponential term in Eq. (5.20) can be easily calculated by decomposing the four-momentum transfer to the proton $Q_n^\mu \overset{\text{def}}{=} q_-^\mu + q_+^\mu - nk^\mu$ into space and time coordinates. The integration over time coordinate yields a delta-function of energy conservation between both $\pi^\pm$ states. The integration over the three dimensional space coordinates gives the known Fourier transform of the Yukawa potential (5.16) (For more details, see Appendix B.2).

Squaring the S-matrix (5.20) and dividing by a unit time T yields the differential production rate

$$\begin{aligned} d^6R &= \frac{1}{T}\frac{Vd^3\vec{q}_+}{(2\pi)^3}\frac{Vd^3\vec{q}_-}{(2\pi)^3}|S^{(1)}_{\pi^+\pi^-}|^2 \\ \Longleftrightarrow d^5R &= \frac{g_\sigma^4}{128\pi^5}\sum_{n\geq n_0} dE_+\sin\theta_+ d\theta_+ d\varphi_+ \sin\theta_- d\theta_- d\varphi_- |\vec{q}_+||\vec{q}_-|\frac{\mathcal{M}_n^2}{\left(m_\sigma^2 + |\vec{Q}_n|^2\right)^2}, \end{aligned} \tag{5.23}$$

similarly as in Eq. (5.9) but with the spin sum omitted. In the last line we used the relation

$$|\vec{q}_-|^2 d|\vec{q}_-|\delta\left(q_+^0 + q_-^0 - nk^0\right) = |\vec{q}_-|q_-^0 dE_-\delta(E_+ + E_- - n\omega_L),$$

with $E_\pm = q_\pm^0$ and we integrated over the energy E_- of the π^--meson. Thus, the diffrential rate for the pair production process becomes

$$d^5R = \frac{g_\sigma^4}{128\pi^5}\sum_{n\geq n_0} dE_+\sin\theta_+ d\theta_+ d\varphi_+ \sin\theta_- d\theta_- d\varphi_- |\vec{q}_+||\vec{q}_-|\frac{\mathcal{M}_n^2}{\left(m_\sigma^2 + |\vec{Q}_n|^2\right)^2}. \tag{5.24}$$

Integrating over all possible momenta yields the total number of produced $\pi^+\pi^-$ pairs per time by absorbing $n \geq n_0$ photons, namely (B.3)

$$R = \frac{g_\sigma^4}{64\pi^4}\sum_{n\geq n_0}\int_{m_\pi^*}^{n\omega_L - m_\pi^*} dE_+ \int_0^\pi \sin\theta_+ d\theta_+ \int_0^\pi \sin\theta_- d\theta_- \int_0^{2\pi} d\varphi_- \frac{|\vec{q}_+||\vec{q}_-|}{\left(m_\sigma^2 + |\vec{Q}_n|^2\right)^2}\mathcal{M}_n^2. \tag{5.25}$$

Finally, the cross section of the hadronic reaction (5.1) may be obtained by dividing out the photon flux $\Phi = \omega_L a^2/4\pi$.

5.3 Numerical Results and Discussion

5.3.1 Results on $\pi^+\pi^-$ Production by Single-Photon Absorption

First, we use our theory to investigate the $\pi^+\pi^-$ photoproduction by single-photon absorption, where a comparison with experimental data is possible. Value of the σ meson mass taken throughout the numerical calculation is $m_\sigma = 550$ MeV [174]. By setting $g_\sigma = 7.79$, we reproduce the $\pi^+\pi^-$ photoproduction cross section $\sigma_{\pi^+\pi^-}$ at 440 MeV as measured with the DAPHNE detector at MAMI [37, 38]. With this choice, we find reasonable agreement with the experimental data in the energy range from threshold up to ≈ 480 MeV, as shown in Fig. 5.4. Due to the adjustment of g_σ to the measured cross section, the Yukawa potential in Eq. (5.16) becomes an effective potential which mimics the contributions from the other relevant Feynman graphs [157] in an approximate way.

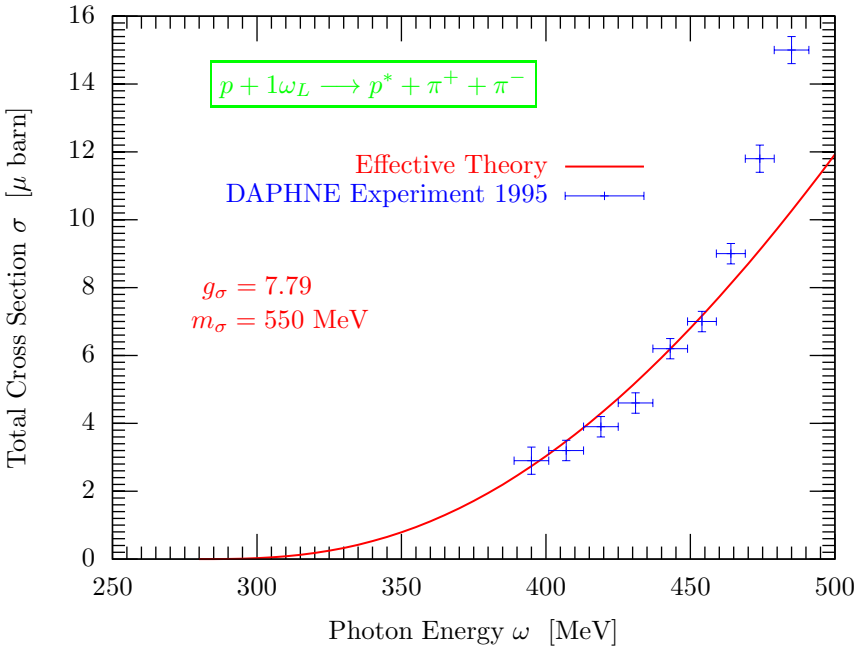

Figure 5.4: Total cross sections for $\pi^+\pi^-$ production by single-photon absorption on the proton. Shown are the experimental data recorded with the DAPHNE detector at MAMI [37, 38] and the results from the present phenomenological model. The coupling constant for the pion-nucleon interaction was set to $g_\sigma = 7.79$ in order to reproduce the measured cross section at 440 MeV.

We note that, at higher photon energies, our predictions nevertheless would deviate significantly from the experimental data in [37, 38]. In fact, within our model the cross section raises to a good approximation like a power law

$$\sigma_{\pi^+\pi^-} \sim (\omega_L - 2m_\pi)^\kappa, \tag{5.26}$$

with $\kappa \approx 2.3$, and thus cannot reproduce the saturation occurring above 700 MeV observed in experiment. Such high energies, however, are not crucial in view of $\pi^+\pi^-$ multiphoto-production. Namely, when a pion pair is created by the absorption of two photons with a total energy of 700 MeV, the energy of each single photon already lies above the $\pi^+\pi^-$ threshold. Since the probability for an n-photon process generally scales like ξ^{2n} in the perturbative coupling regime ($\xi \ll 1$), the two-photon process is strongly suppressed as compared with the dominant single-photon process. Hence, for our purposes the good agreement in the energy range up to 480 MeV may be considered sufficient to obtain order-of-magnitude estimates for $\pi^+\pi^-$ multiphoto-production.

Figure 5.5 displays the angular distribution of one of the produced pions by one photon absorption as a function of the polar emission angle θ, which is measured with respect to the incident laser wave vector $\vec{k}_L$ (see

Fig. 5.2). In each curve an amount of energy of $\omega_L = 360, 400, 440, 460$ and 480 MeV is absorbed from the laser beam. The spectra have been normalized to the same height in order to facilitate their comparison.

ω_L [MeV]	360.0	400.0	440.0	460.0	480.0
$\theta_{\max}$ [deg]	40.80	33.96	29.67	27.61	25.61

Table 5.1: Energy dependence of the polar emission angle θ of one of the produced pions.

The position of the maximum at each value of ω_L is shown in Table 5.1 and the results are in reasonable agreement with experimental observation [175]. As we can see, the larger the photon energy, the more shifted is the maximum towards smaller angles and the more narrow become the distributions. This happens because by increasing ω_L, the momentum $\vec{q}$ of the created pion becomes larger and larger and shifted along the propagation direction of the laser wave vector in the z-direction, so that $\theta \equiv (\widehat{\vec{q}, \vec{e}_z})$ goes to zero.

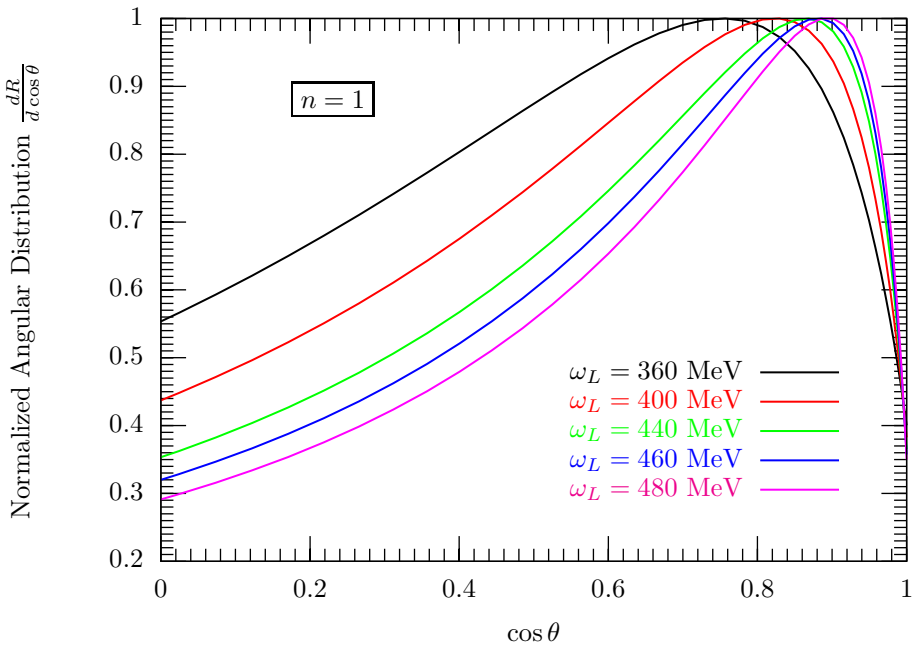

Figure 5.5: Normalized angular distributions of one of the particles in $\pi^+\pi^-$ photoproduction on the proton by one photon absorption. The spectra refer to the proton frame and the angle is measured with respect to the laser beam direction (i.e. with respect to $\vec{k}_L$).

5.3.2 Results on Multiphoton $\pi^+\pi^-$ Production

Based on Eq. (5.17), we calculate total rates and angular spectra for multiphoto-production of $\pi^+\pi^-$ pairs in ultrarelativistic proton-laser collisions. The value $g_\sigma = 7.79$ is used for the pion-nucleon coupling constant in the effective potential (5.16). The threshold for $\pi^+\pi^-$ production by two-photon absorption lies at an x-ray laser frequency of $\omega_L^{\rm lab} \approx m_\pi/2\gamma \approx 10$ keV in the laboratory frame, when the proton beam is counterpropagating the laser beam with a Lorentz factor of $\gamma = 7000$. This frequency domain is aspired by the currently emerging x-ray laser facilities [116, 117, 151–153]. Below, we mainly concentrate on processes involving two photons.

Figure 5.6 shows our results on the total production rates as a function of the photon energy, referring to the rest frame of the proton. In the laboratory frame, the rates are reduced to $R_{\rm lab} = R/\gamma$ due to time dilation. For the laser vector potential, the value $ea = 5.1$ keV has been assumed. It corresponds to x-ray

intensities of the order of 10^{22} W/cm^2 in the laboratory frame. In view of the remarkable recent advances in x-ray technology, this level appears achievable nowadays at large-scale XFEL machines, though lying about three orders of magnitude above their original design values. For example, the recently commissioned Linac Coherent Light Source in Stanford/USA is currently able to produce 1-keV x-ray pulses with an intensity up to 10^{18} W/cm^2 [152]. Reduction of the present focal area of ~ 1 μm^2 down to $\sim$ (10 nm)^2 would enhance the intensity to 10^{22} W/cm^2. Corresponding improved x-ray focusing techniques are on the way [176].

Let us consider an example. For a photon energy of 200 MeV in the proton frame, the $\pi^+\pi^-$ production rate by two-photon absorption amounts to $R \sim 10^3$ s^{-1} as shown in Figure 5.6. Hence, in the collision of an LHC proton beam containing 10^{11} particles [150] with an x-ray pulse of 100 fs duration [151,152], the probability for production of one pion pair would be 10^{-8}, assuming that a million protons interact with the field due to only partial beam overlap. An average production rate of about one $\pi^+\pi^-$ pair per hour is obtained by taking the envisaged x-ray pulse repetition rate of 10 kHz into account [151]. Note that the latter could be synchronized with the revolution frequency of the LHC proton beam. The $\pi^+\pi^-$ production rate by two-photon absorption scales as the square of the applied x-ray intensity, as long as $\xi \ll 1$ holds.

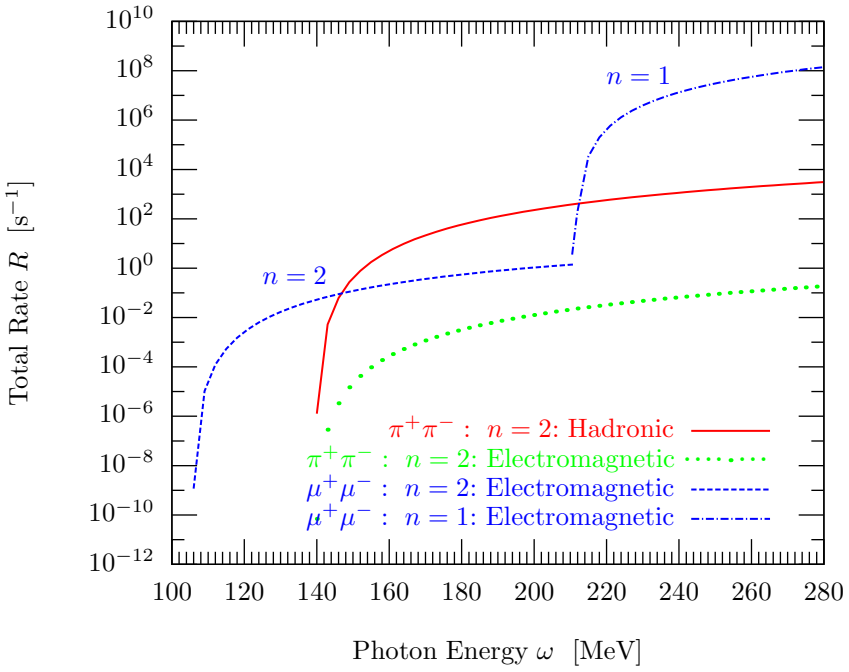

Figure 5.6: Total rates for $\pi^+\pi^-$ and $\mu^+\mu^-$ pair production on the proton by one- and two-photon absorption, as functions of the photon energy. The amplitude of the laser vector potential is $ea = 5.1$ keV, corresponding to lab-frame photon intensities $I_{\rm lab} = (\omega_L^{\rm lab}\, a)^2/4\pi$ of the order of 10^{22} W/cm^2.

We note that the effect of the electric and magnetic pion polarizabilities turns out to be immaterial for the present parameters. The reason is that the parameter

$$\frac{(\lambda_e + \lambda_m)(p_\pm k)^2}{m_\pi}/ \approx (\lambda_e + \lambda_m) m_\pi^3 \sim 10^{-5}, \tag{5.27}$$

which effectively quantifies the coupling of the external laser field to the pion polarizabilities [123], is much smaller than its coupling $e^2 \approx 0.0917$ to the pion charge.

In order to detect the process of $\pi^+\pi^-$ production by two-photon absorption unambiguously in experiment, it is necessary to discriminate it from competing pion production channels. A strong background of π^+ will form through the single-photon reaction (5.3). The produced neutron may further lead to π^- creation via the subsequent reaction

$$n + \omega_L \longrightarrow \pi^- + p.$$

For the purpose of discrimination, the angular and energetic distributions of the generated π^- might serve as a fingerprint for the nonsequential two-photon process; see also Fig. 5.7 below. Besides, a background of e^+e^- pairs will arise from the ordinary (single-photon) Bethe-Heitler process on the proton. Note that these background processes are not so strong to deplete the x-ray beam noticeably [102, 103].

It is interesting to compare the $\pi^+\pi^-$ production rate by two-photon absorption with the corresponding rate for $\mu^+\mu^-$ production [102, 103]. Although the muon mass is substantially smaller than the pion mass, $\pi^+\pi^-$ production is dominant in the frequency range between approximately 150 and 210 MeV, as shown in Figure 5.6. For example, at a photon energy of 200 MeV, the production of pions exceeds the production of muons by three orders of magnitude. The dominance of $\pi^+\pi^-$ production is due to the much larger strength of the hadronic interaction. The purely electromagnetic contribution to $\pi^+\pi^-$ production [resulting from the Coulomb potential of the proton in Eq. (5.8)] is suppressed by four orders of magnitude and, thus, smaller than the $\mu^+\mu^-$ rate. For higher photon energies ($\omega_L > 2m_\pi$), the channel of $\mu^+\mu^-$ production by a single photon opens and represents the dominant process. Our results imply that in the frequency interval 150 MeV $\lesssim \omega_L \lesssim$ 210 MeV muon pairs are predominantly produced indirectly via two-photon $\pi^+\pi^-$ production and subsequent pion decay

$$\pi^+ \longrightarrow \mu^+ + \nu_\mu, \tag{5.28a}$$

and

$$\pi^- \longrightarrow \mu^- + \bar{\nu}_\mu. \tag{5.28b}$$

Figure 5.7 displays our results on the angular distribution $dR/d\cos\theta$ of one of the created pions by one-, two- and three-photon absorption. The respective photon energies were chosen such that the energy absorbed in total is always 360 MeV. The polar emission angle θ is measured with respect to the incident laser wave vector.

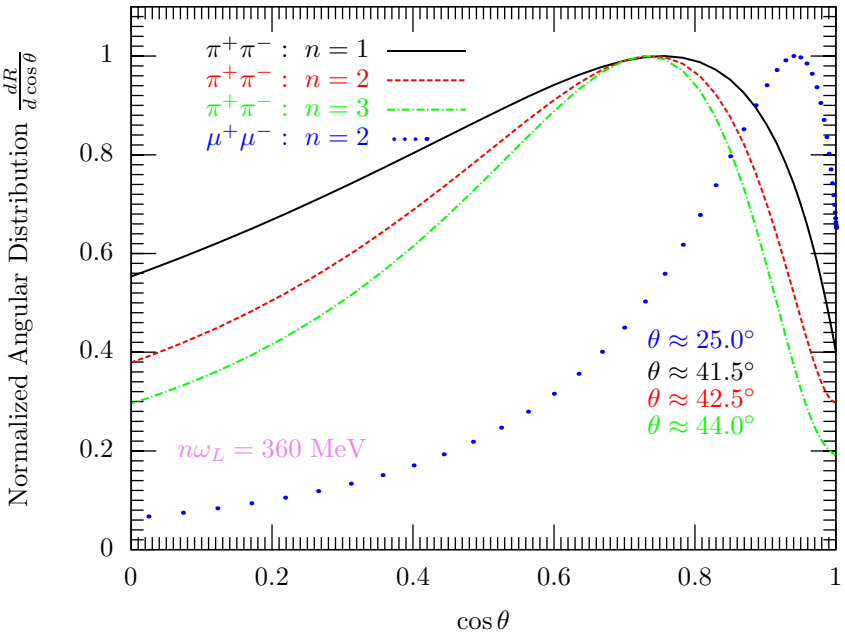

Figure 5.7: Angular distributions of one of the particles in $\pi^+\pi^-$ and $\mu^+\mu^-$ photoproduction on the proton. The spectra refer to the proton frame and the angle is measured with respect to the laser beam direction (i.e. with respect to $\vec{k}_L$). In all cases, an identical amount of energy is absorbed from the laser field ($n\omega_L = 360$ MeV). The spectra have been normalized to the same height in order to facilitate their comparison.

The calculated angular spectrum for $\pi^+\pi^-$ production by one photon attains a maximum at $\theta \approx 41.5°$. We note that the position of the maximum is in reasonable agreement with experimental observation [175]; our

model overestimates, however, the contributions from very large emission angles. For two- and three-photon absorption the position of the maximum is shifted towards slightly larger angles ($\theta \approx 42.5°$ and $\theta \approx 44°$, respectively) and the distributions become more narrow. These are characteristic multiphoton effects which have also been found in e^+e^- pair production by few-photon absorption [177].

We draw again a comparison with two-photon production of $\mu^+\mu^-$ pairs. As Figure 5.7 shows, here the angular distribution is peaked at smaller angles around $\theta_+ \approx 25°$ and the contribution from large angles is suppressed. The differences are caused by the long-range nature of the Coulomb potential (5.8) as compared to the short-ranged Yukawa potential (5.16). In the latter case, the particles are mainly produced at short distances which gives rise to large momentum transfers $\boldsymbol{q}$ corresponding to large emission angles. For the muons, small momentum transfers are relatively more important since the Fourier transform of the Coulomb potential is proportional to $1/\boldsymbol{q}^2$, as compared to $1/(\boldsymbol{q}^2 + m_\sigma^2)$ for the Yukawa potential (5.16). For more details, see Eq. (B.8) of Appendix B.2.

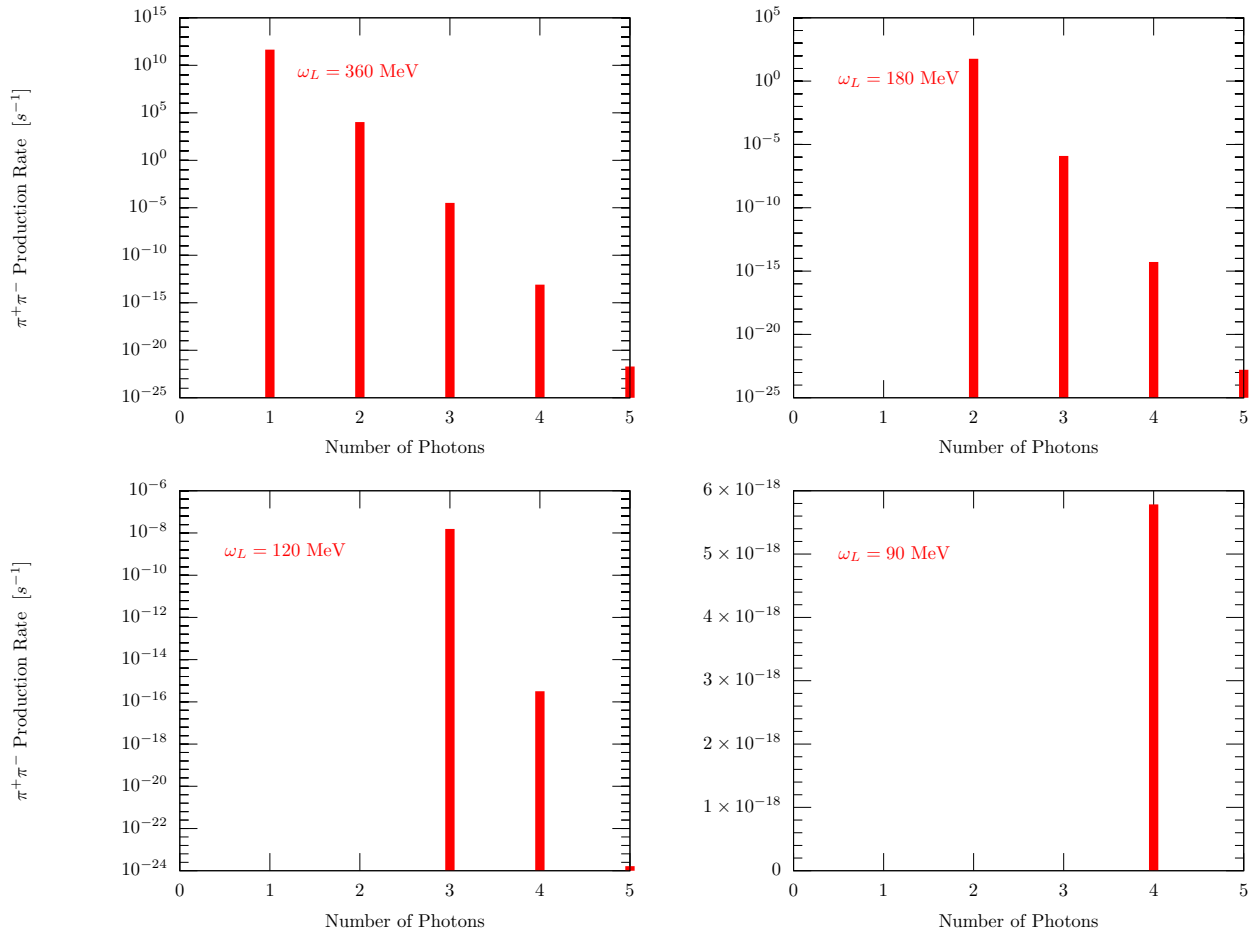

Figure 5.8: The photon number distributions of one of the particles in $\pi^+\pi^-$ photoproduction on the proton as a function of the number n of the absorbed laser photons. The distributions are computed at various photon energies: $\omega_L = 90, 120, 180, 360$ MeV of the circularly polarized laser. The corresponding intensities are respectively 7.32×10^{21}, 1.30×10^{22}, 2.93×10^{22} and 1.17×10^{23} W/cm^2 in the laboratory frame.

In Figure 5.8 we show the photon number distributions of π^- or π^+ meson as a function of the number n of the absorbed laser photons. We see that the photoproduction rate decreases with increasing the number of absorbed laser photons from 1 to 5. We explain this behavior by the fact that the arguments α in Eqs. (5.21) of the ordinary Bessel-functions are much smaller than 1 at all intensities. According to our calculations we have

found that $\alpha \leqslant 10^{-8}$, so that we can well approximate $B_n(\alpha)$, $C_n(\alpha)$ and $D_n(\alpha)$ as: $const \cdot \alpha^n$, and the $\pi^+\pi^-$ photoproduction process is perturbative.

5.3.3 Kinematic Investigation of $\pi^+\pi^-$ Pair Production

It would be interesting to investigate the hadronic reaction (5.1) kinematically in order to obtain informations about the velocities and masses of all particles after interaction. Before the proton has been treated as an external potential, i.e. its recoil motion was neglected, while here as a massive particle and we want to look into proton recoil. We consider the reaction (5.1) for $n = 1$ as illustrated in Figure 5.2. We denote the four-momentum of the photon before interaction by

$$k_L^\mu = (\omega_L,\ \omega_L \cdot \vec{e}_z),$$

and the proton by

$$p^\mu = (\gamma m_\mathrm{p},\ -\gamma m_\mathrm{p}\beta \cdot \vec{e}_z).$$

After interaction, we denote the four-momentum of

- the π^--meson by: $p_-^\mu \equiv (\gamma_- m_\pi,\ \gamma_- m_\pi \beta_- \cdot \vec{e}_1)$,
- the π^+-meson by: $p_+^\mu \equiv (\gamma_+ m_\pi,\ \gamma_+ m_\pi \beta_+ \cdot \vec{e}_2)$, with $p_-^2 = p_+^2 = m_\pi^2$, and
- the recoiling proton by: $p^{*\mu} = (\gamma^* m_\mathrm{p}^*,\ -\gamma^* m_\mathrm{p}^* \beta^* \cdot \vec{e}_z)$,

where we assumed that the accelerated proton is not deflected from its direction of propagation. The conservation of energy and momentum merely equates the sum of energies and momenta before and after interaction, that is

$$k_L^\mu + p^\mu \stackrel{!}{=} p_-^\mu + p_+^\mu + p^{*\mu}. \tag{5.29}$$

Squaring both sides of this equation gives

$$\begin{aligned}
&\frac{2m_\pi^2}{m_\mathrm{p}^2}\left[1 + \gamma_-\gamma_+(1 - \beta_-\beta_+ \cos\widehat{(\vec{p}_-, \vec{p}_+)})\right] = 1 + \left(\frac{m_\mathrm{p}^*}{m_\mathrm{p}}\right)^2 + \\
&\omega_L\left[\frac{\gamma}{m_\mathrm{p}}(1 - \beta \cdot \cos\widehat{(\vec{e}_z, \vec{p})}) - \frac{\gamma^*}{m_\mathrm{p}}(1 - \beta^* \cdot \cos\widehat{(\vec{e}_z, \vec{p}^*)})\frac{m_\mathrm{p}^*}{m_\mathrm{p}}\right] - 2\gamma\gamma^*(1 - \beta\beta^* \cos\widehat{(\vec{p}, \vec{p}^*)})\frac{m_\mathrm{p}^*}{m_\mathrm{p}}.
\end{aligned} \tag{5.30}$$

We suppose that π^+ and π^- travel in the yz plane with the same speed and kinetic energy, i.e. $\beta_- = \beta_+ = \beta_{\pi^\pm} \Rightarrow \gamma_- = \gamma_+ = \gamma_{\pi^\pm}$, and $\widehat{(\vec{p}_-, \vec{p}_+)} = 2\theta$. Values of θ can be taken from the results of Subsection 5.3.1. We also have $\widehat{(\vec{e}_z, \vec{p})} = \widehat{(\vec{e}_z, \vec{p}^*)} = \pi$ and $\widehat{(\vec{p}, \vec{p}^*)} = 0$. Thus, we can solve equation (5.30) for m_p^*, the solution will be in terms of the photon energy of the laser beam ω_L, the reduced velocity of one of the created pions $\beta_{\pi^\pm}$ and the reduced velocity of the nucleon resonance β^*.

In Figures 5.9 we show the dependence of the nucleon resonance rest mass m_p^* with its reduced velocity and the reduced velocity of the created $\pi^\pm$-pions. By increasing the laser photon energy up to 480 MeV, the mass of the exited proton after interaction exceeds 1200 MeV, which corresponds to the nucleon resonances $\underset{\mathrm{uud}}{\Delta}^+(1236)$, $\mathrm{N}^*(1440)$, $\mathrm{N}^*(1520)$ and $\Delta^+(1700)$.

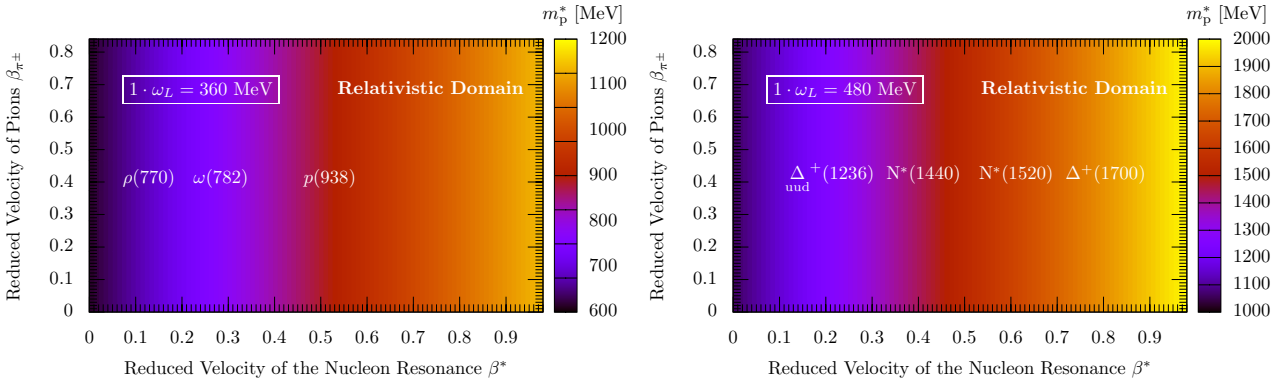

Figure 5.9: Map of the nucleon resonance rest mass m_p^* as a function of its reduced velocity and the reduced velocity of one of the created pions by one-photon absorption. The input parameters are: Laser photon energy: $\omega_L = 360$ MeV (Left) and $\omega_L = 480$ MeV (Right). The corresponding angles between π^+ and π^- particles momenta are taken from Table 5.1 and multiplied by 2. The initial Lorentz Factor of the proton: $\gamma = 7000$ with a rest mass of roughly 938.27 MeV..

In Figure 5.10 we take the velocities of the created pions as $\beta_{\pi^\pm} = 0.9$, and we show the dependence of the nucleon resonance rest mass with its reduced velocity and the photon energy of the laser beam. In the photon energy range between 300 and 500 MeV, m_p^* is between 1.0 and 1.44 GeV. This result is in agreement with phenomenological calculations based on effective Lagrangians for the meson-nucleon interaction [157].

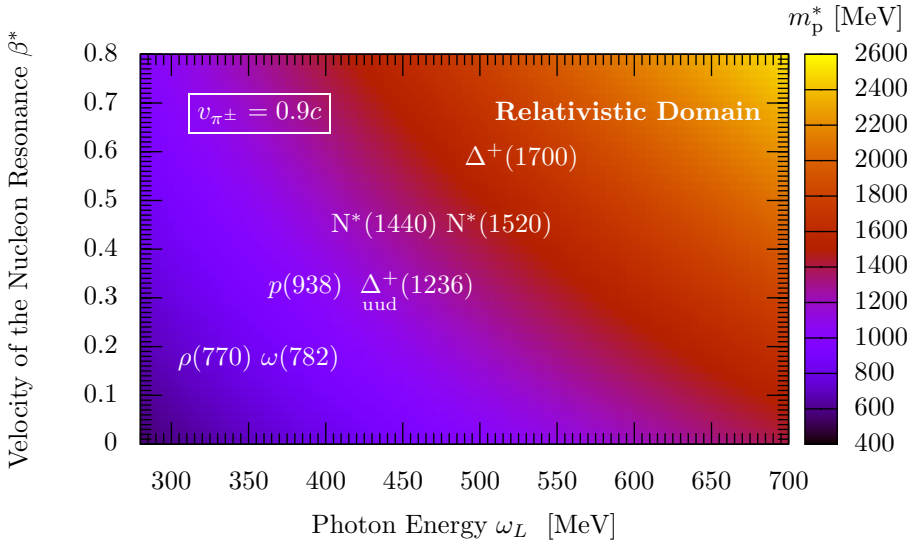

Figure 5.10: Map of the nucleon resonance rest mass m_p^* as a function of its reduced velocity and the laser photon energy. Th velocities of the created pions is taken as $\beta_{\pi^\pm} = 0.9$.

We note that by $n > 1$, Eq. (5.30) yields the same results as by one photon absorption, as long as the total photon energy $n\omega_L$ fulfils Eq. (5.22a). Furthermore, we see that for proton energies of about 360 MeV,

the proton recoil is small, rendering the description of the proton by an external potential in the previous Subsection 5.3.2 reasonable.

–VI–

Conclusions and Outlook

In the present doctoral thesis, we have dealt with different problems associated with nuclear- and hadronic processes in intense light-matter interaction. In the first part, we have studied the photoemission of a weakly-bound proton from a halo-nucleus by absorption of a γ-ray photon in the presence of a strong optical laser beam. The electromagnetic interaction of the emitted proton with the laser photon field was incorporated into nonrelativistic Volkov state using the dipole approximation, while an approximated wave function was used to describe the intial state of the weakly bound proton-halo. It was shown that the assisting laser field modifies the properties of the photonuclear effect in a characteristic way. We have investigated the energy distribution of the photoproton in terms of the number of absorbed laser photons, as well as the angular proton distribution as a function of the polar emission angle. The dependencies on field frequencies, polarizations and geometries were discussed as well. The results presented in the first part of the thesis yield the following conclusions:

(1) The presence of the laser beam, with high frequency and high electric field strength, has a minor effect on the γ-photon energy dependence of the total photoproton cross section.

(2) The maximum value of the total cross section, when plotted as a function of the γ-photon energy, is considerably larger than those obtained from experimental data of photoproton cross sections in stable nuclei [136–139]. This result confirms our expectation that it is easier to induce a photonuclear reaction in halo-nuclei than in stable ones by using high-energy photons, because of their small binding energy and their large spatial extension.

(3) For fixed input parameters of both the γ-ray photon and the laser field (i.e., ω', E', ω_L and E_L), the total photoproton cross section remains unchanged. The total cross section is also independent of the orientation of the electric field vector $\vec{E}_L$ with respect to $\vec{E}'$ and of the laser polarization (circular or linear).

(4) The photoproton energy distribution, when plotted as a function of the number n of exchanged laser photons, is symmetric around $n = 0$, which means that the absorption and the emission of n laser photons have almost the same probabilities. This characteristic agrees with that reported by the Low's theorem for multiphoton processes [142].

(5) The multiphoton character of the photonuclear effect becomes apparent for copropagating γ-ray photon and circularly polarized laser field. In contrast, single-photon character is apparent for orthogonally propagating ones. In both cases, multiphoton and single-photon characters, appear more clearly and rapidly by increasing the electric field strength, or equivalently the intensity of the circularly-polarized laser field. This result is quite different when the laser is linearly-polarized: The difference between the multiphoton and the single-photon character becomes most apparent at higher laser intensities. In general terms, we have observed a strong effect of the orientation of the laser's electric field vector on the energy spectra of the photoproton-halo.

(6) The probability of inducing the photonuclear effect by one-photon absorption, is higher for copropagating laser and γ-ray photon than for orthogonally propagating ones, and this fact is true for any polarization of the laser field.

(7) As the proton is ejected from core-halo by the γ-ray photon and travels out through the high-frequency laser, its back and forth motion becomes more sensitive for copropagating waves than for orthogonally propagating waves.

(8) The probability of inducing the photonuclear reaction in a halo-nucleus by absorbing n-photons from a circularly polarized laser beam is higher than that from a linearly polarized laser. This result is in good agreement with experimental observations in atomic physics [143, 144]. In addition, our result also agrees with perturbation theory calculations for weak couplings [145–149], which indicate that circular polarization cross sections and rates are somewhat larger than for linear polarization due to the field correlation (photon statistics) effects in single-photon and multiphoton processes.

(9) The angular proton distribution, when summing over all exchanged laser photons, depends neither on the polarization of the laser field, nor on the orientation of its electric field vector $\vec{E}_L$ with respect to that of the γ-photon, i.e. $\vec{E}'$.

(10) Single-photon and multiphoton angular distributions of the photoproton at a given proton energy depend strongly on the field geometries, polarizations and strengths.

We have thus learned from this part how to induce a photonuclear reaction in exotic halo-nuclei with optimum field configurations, i.e. in terms of orientation, polarization and strength. We would say that low-frequency circularly polarized laser beam and orthogonally propagating with a γ-ray photon would be the best field configuration. In addition, there is no reason to restrict this estimation to exotic halo-nuclei, since by increasing the laser electric field strength and at the same time the photon energy of the γ-ray, we can achieve the typical nuclear level spacing required to induce a photonuclear reaction in stable nuclei.

In the second part of the thesis, a phenomenological model of $\pi^+\pi^-$ production by multiphoton absorption on the proton has been presented. The electromagnetic interaction of the pions with the photon field was incorporated into scalar-relativistic Volkov states, while an effective potential was used to describe the hadronic pion-nucleon coupling. The model contains one free parameter which has been adjusted to a measured cross section of $\pi^+\pi^-$ single-photon production at 440 MeV. Multiphoto-production of pion pairs could, in principle, be realized by utilizing the 7 TeV proton beam at CERN-LHC in conjunction with a compact 10-15 keV x-ray laser source.

Predictions for total rates of two-photon $\pi^+\pi^-$ production were provided. In particular, it was shown that the two-photon production of $\pi^+\pi^-$ pairs substantially dominates over the (direct) production of muon pairs for photon energies above 150 MeV up to the threshold for $\mu^+\mu^-$ single-photoproduction. In this range of photon energies, muons are thus predominantly created indirectly via pion decays. We note that a similar conclusion was drawn in [15] with respect to pion and muon production by single bremsstrahlung photons in a laser-generated plasma.

Angular pion spectra have also been calculated which reflect the short-range nature of the hadronic interaction. When the $\pi^+\pi^-$ pair is created by more than one photon, the typical emission angles are slightly larger corresponding to larger momentum transfers in the process.

Throughout the second part, the accelerated proton has been treated as an external potential, i.e. its recoil motion was neglected. By investigating the $\pi^+\pi^-$ photoproduction process kinematically where the proton is treated as a massive particle, we have found that for proton energies of about 360 MeV, the proton recoil is small, rendering the description of the proton by an external potential reasonable.

Outlook

As an outlook for further research, we discuss some general issues for which the processes of laser-assisted photonuclear effect in halo-nuclei and the multiphoto-production of pions might prove to be especially useful.

- **For the laser-assisted photonuclear effect in halo-nuclei:**

One may ask, "What could happen after the emission of the proton from the halo-nucleus?" In reality, when the proton is emitted through the γ-ray-induced photonuclear effect, different scenarios could happen after its acceleration or deceleration by the strong laser field. For example, (a) a proton recombination with the core-halo, which may be seen as an inverse process of the photonuclear effect, (b) further nuclear fissions giving rise to other nuclides before any γ- or β-decay occurs, (c) a proton-impact double ionization, etc. From there it would be interesting to investigate these scenarios and to specify the optimum field configuration to drive these reaction chains. So, we can get from these studies time informations in the nuclear dynamics of the dissociation process. These investigations are analogous to what people might have calculated for the photoelectron emission [17, 102, 178], and thus it would be important to draw analogies with field-induced processes known from atomic physics. The first part of this thesis is thus a first step of the generalization of the recollisions concept from atoms to nuclei.

Owing to a large and still ongoing technological progress in generating intense coherent photon beams from powerful laser sources, the synthesis of nuclei in the laboratories with large proton-neutron asymmetry or with other exotic properties might be possible. However, to this day, it is still unclear at the theoretical level how the protons and neutrons are held together to form such exotic objects, even if the lifetimes of some of them are too short. The current realistic and phenomenological models of atomic nuclei, which have been developed to explain the data from photonuclear reactions using stable nuclei only, are in disagreement with a wide range of experiments on the properties of exotic nuclei. Thus, our study of laser-assisted photonuclear processes may help to improve our understanding of the structures and dynamics of exotic nuclei far from stability, and hence to make more consistency between theory and experimental observations.
We can extend our stuy by using the so called "improved Coulomb-Volkov state" [30, 32, 33] instead of the "Volkov state" to take into account the Coulomb interactions between the nuclear-core and the emitted proton. But in general, we can try to construct our Hamiltonian (or the Lagrangian density for a relativistic treatment) which includes: (a) the kinetic energy of the proton, (b) the Coulomb interactions between the proton and the nuclear-core, (c) the spin-orbit coupling between the bound proton-halo and the nuclear-core, and (d) the strong interaction between the bound-proton and the nuclear-core using a meson-exchange potential or simply a Woods-Saxon potential. Afterwards, we should impose some constraints on the Hamiltonian or the Lagrangian, so that the derived wave function from the equation of motion of the proton fulfils two conditions: First, the initial wave function for the bound-proton should experimentally be adequate for describing the main halo properties of the isotope we want to investigate (e.g., the mean square radius, binding energy, etc.); Second, the continuum wave function of the proton should describe the motion of the proton traveling out through a strong electromagnetic field, for example, it may be similar to the Coulomb-Volkov wave function.

In these ways, our study of laser-assisted photonuclear processes in halo-nuclei, or especially the study of the laser-assisted (γ, p) reactions, may potentially contribute to understand various astrophysical processes. For example, the solarboron-neutrino problem [84, 85], the existence of hyperons in neutron stars [179], the stellar nucleosynthesis, i.e. the synthesis of chemical elements in the stars which takes place via photonuclear reactions with exotic nuclei, and especially in nucleosynthesis of heavy proton-rich nuclei during supernovae explosions [5, 6]. Third, our study may provide a better understanding of high-density high-temperature phenomena in ultrarelativistic heavy-ion collisions [180].

This work may also give relevant informations and confidence to experimentalists about how to generate proton beam from laser-assisted or laser-induced (γ, p) reactions with optimum field configurations as discussed in detail here, and as we know, the proton beam generation is very important in various disciplines, such as in nuclear medicine, proton beam radiography in tumor detection, nuclear chemistry and in fusion reactors.

- **For the multiphoto-production of $\pi^+\pi^-$ pairs in ultrarelativistic proton-laser collisions:**

Due to their long wavelength, photons interact uniformly over the nuclear volume and can therefore provide quantitative information on the entire structure of a given nucleus. Multiphoton processes such as $\pi^+\pi^-$ production might be able to complement insights into the nuclear interior from single-photon reactions, since the momentum transfers involved exhibit a different distribution. This might help to gain an improved understanding of the short-range repulsion and intermediate-range attraction in the nucleon-nucleon potential.

A main focus of pion photo-production is presently lying on polarization observables [39–43]. Pion pair production via multiphoton absorption from a circularly polarized laser beam could be of particular interest in this regard. Since all photons carry the same helicity, the simultaneous absorption of several of them might lead to characteristic signatures in the polarization properties of the produced pions.

Finally, photoproduction of pions possesses an interesting analogy in atomic physics. A formal relation between the strong-field processes of e^+e^- pair production and atomic photoionization in intense laser fields has already been revealed (see, e.g., [95]). In the same spirit, a connection between photoionization of atoms and photoproduction of pions may be established, taking into account that pions can be produced both as single particles and in pairs. An analogy with single and double ionization of helium by one- and two-photon absorption is therefore suggestive. These four different ionization processes have found a sustained interest in atomic physics because of their sensitivity to electron-electron correlations [181]. While the production of single pions and pion pairs by one photon has been examined for a long time, we presented in the second part of this thesis a first study of pion pair production by two-photon absorption. The picture consisting of all four channels may be completed by a consideration of single pion production by two-photon absorption.

–I–

Some Complements to Laser-Assisted Photonuclear Effect

In this Appendix we present a brief discussion of some equations derived in Section 4.3.

A.1 The Jacobi-Anger Expansion

For any $(x,t) \in (\mathbb{R}\times\mathbb{R}), n \in \mathbb{Z}$ we have

$$\exp\left(ix\sin t\right) = \sum_{n=-\infty}^{+\infty} c_n e^{int}, \qquad \text{with} \quad c_n = \frac{1}{T}\int_{-T/2}^{+T/2} e^{ix\sin t} e^{-int} dt \qquad \text{for} \quad T = 2\pi.$$

Thus, c_n is the integral representation of ordinary Bessel-functions

$$J_n(x) \equiv \frac{1}{2\pi}\int_{-\pi}^{+\pi} \exp\left[-i(nt - x\sin t)\right] dt = c_n. \tag{A.1}$$

That is,

$$e^{ix\sin t} = \sum_{n=-\infty}^{+\infty} J_n(x) e^{int}, \tag{A.2a}$$

or

$$e^{-ix\sin t} = \sum_{n=-\infty}^{+\infty} J_n(x) e^{-int}. \tag{A.2b}$$

A.2 The γ-Ray Photon Flux

According to Eq. (4.8), the electrostatic and magnetic fields of the γ-ray are given by

$$\vec{E}' = -\frac{\partial \vec{A}'}{\partial t} = i\omega' A_0' e^{i\left(\vec{p}\,'\vec{r} - \omega' t\right)} \cdot \vec{e}_z, \tag{A.3a}$$

$$\vec{B}' = \overrightarrow{\text{rot}}\vec{A}' = -ip' A_0' e^{i\left(\vec{p}\,'\vec{r} - \omega' t\right)} \cdot \vec{e}_y, \tag{A.3b}$$

where $A_0' = \sqrt{\dfrac{2\pi}{V_{ph}\cdot\omega'}}$. Assuming that $\vec{p}\,' = p_x' \cdot \vec{e}_x \equiv k'\vec{e}_x$ we get $\vec{p}\,'\vec{r} = k'x$.

To determine the γ-ray photon flux, we first calculate the mean value of the Poynting vector when averaged over time, and then dividing it by the photon energy. We have

$$\begin{aligned}\Phi &= \frac{\langle \vec{R}' \rangle}{\omega'} \\ &= \frac{1}{\omega'} \cdot \frac{1}{2} \frac{1}{\pi \mu_r} Re \left(\vec{E}' \times \vec{B}'^{*} \right) \\ &= \frac{1}{\omega'} \cdot A_0'^2 \omega' k' \\ &= \frac{1}{\mu_r V_{ph}}. \end{aligned} \tag{A.4}$$

If we neglect the effect of the laser beam when the proton is initially bound to the nucleus, we can take the relative permeability $\mu_r = 1$, which simply yields $\Phi = 1/V_{ph}$.

–II–

Pair Production Rate

In this Appendix we present in detail the proofs of different equations from Chapter 5 and we discuss their physical contents.

B.1 The first order of the T-Matrix Expansion

Proof of Eqs. (5.17):

The first order of the Klein-Gordon T-matrix by an scattering potential $\hat{V}(x) = \left(\partial_\mu V^\mu(x) + V_\mu(x)\partial^\mu\right)$ describing the process of $\pi^+\pi^-$ pair production is

$$\begin{aligned}
S^{(1)}_{\pi^+\pi^-} &= \frac{i^1}{1!}\int d^4x\; T\{\phi^*_-\hat{V}\phi_+\} \\
&= i\int dx^0 d^3\vec{x}\;\phi^*_-\left(\partial_\mu V^\mu + V^\mu\partial_\mu\right)\phi_+ \\
&= i\int dx^0 d^3\vec{x}\;\phi^*_-\left[\underbrace{\left(\partial_\mu V^\mu\right)}_{=0}\cdot\phi_+ + V^\mu\cdot\left(\partial_\mu\phi_+\right) + V^\mu\left(\partial_\mu\phi_+\right)\right] \qquad \text{(Lorentz gauge)} \\
&= i\int dx^0 d^3\vec{x}\left(\phi^*_-\left(\partial_\mu\phi_+\right) - \phi_+\left(\partial_\mu\phi^*_-\right)\right)V^\mu(x) \quad \text{because } \phi^*_-\cdot\left(\partial_\mu\phi_+\right) = -\left(\partial_\mu\phi^*_-\right)\cdot\phi_+ \\
&= i\int d^4x\;\left(\phi^*_-\overleftrightarrow{\partial_\mu}\phi_+\right)V^\mu(x). \qquad \text{(B.1)}
\end{aligned}$$

By taking $V^\mu(x)$ as a scalar Yukawa-type potential, i.e $V^\mu(x) = (V_{\text{had}}(x), \vec{0})$, then we get

$$S^{(1)}_{\pi^+\pi^-} = i\int dx^0 d^3\vec{x}\left(\phi^*_-\left(\partial_t\phi_+\right) - \phi_+\left(\partial_t\phi^*_-\right)\right)V_{\text{had}}(x). \qquad \text{(B.2)}$$

Q.E.D. (5.17)

B.2 Evaluation of the $S^{(1)}_{\pi^+\pi^-}$-Matrix Elements

Proof of Eqs. (5.20), (5.21):

The function f defined by $f(\eta) \overset{\text{def}}{=} \exp ie\left[\alpha_1\sin(\eta) - \alpha_2\cos(\eta)\right]$ is periodic for all values of $\eta = k^\mu x_\mu$ of period 2π, as well as $\cos(\eta)f(\eta)$ and $\sin(\eta)f(\eta)$. These three functions appearing in the $S^{(1)}$-matrix (5.18) can be

expanded analytically into Fourier series of coefficients B_n, C_n and D_n, respectively. That is

$$f(\eta) = \sum_{n=-\infty}^{+\infty} B_n e^{+in\eta}, \qquad \cos(\eta) f(\eta) = \sum_{n=-\infty}^{+\infty} C_n e^{+in\eta} \qquad \text{and} \qquad \sin(\eta) f(\eta) = \sum_{n=-\infty}^{+\infty} D_n e^{+in\eta}.$$

Inserting these transformations into Eq. (5.18) then yields Eq. (5.20). Now in order to determine B_n, C_n and D_n as in eqs.(5.21) we first write f as follows

$$f(\eta) = \exp ie\left[\alpha \sin(\eta - \eta_0)\right],$$

for $\alpha = \sqrt{\alpha_1^2 + \alpha_2^2}$, $\alpha_1 = \alpha\cos(\eta_0)$ and $\alpha_2 = \alpha\sin(\eta_0)$.

The Jacobi-Anger expansion: For any $(x,t) \in (\mathbb{R}\times\mathbb{R}), n \in \mathbb{Z}$ we have

$$\exp(ix\sin t) = \sum_{n=-\infty}^{+\infty} c_n e^{int}, \qquad \text{with} \quad c_n = \frac{1}{T}\int_{-T/2}^{+T/2} e^{ix\sin t} e^{-int} dt \qquad \text{for} \quad T = 2\pi.$$

Thus, c_n is the integral representation of ordinary Bessel-functions

$$J_n(x) \equiv \frac{1}{2\pi}\int_{-\pi}^{+\pi} \exp\left[-i(nt - x\sin t)\right] dt = c_n. \tag{B.3}$$

That is,

$$e^{ix\sin t} = \sum_{n=-\infty}^{+\infty} J_n(x) e^{int} \quad \text{or} \quad e^{-ix\sin t} = \sum_{n=-\infty}^{+\infty} J_n(x) e^{-int}.$$

i. *Identification of* B_n: $\quad x \longrightarrow \alpha, \quad t \longrightarrow \eta - \eta_0$

$$\begin{aligned} &\Longleftrightarrow e^{i\alpha\sin(\eta-\eta_0)} = \sum_{n=-\infty}^{+\infty} J_n(\alpha) e^{in(\eta-\eta_0)} = \sum_{n=-\infty}^{+\infty} J_n(\alpha) e^{-in\eta_0}\cdot e^{in\eta}. \\ &\Longleftrightarrow \boxed{B_n = J_n(\alpha) e^{-in\eta_0}}. \end{aligned} \tag{B.4}$$

ii. *Identification of* C_n:

$$\begin{aligned} \sum_{n=-\infty}^{+\infty} C_n e^{in\eta} &\overset{!}{=} \cos(\eta) e^{i\alpha\sin(\eta-\eta_0)} \\ &= \frac{1}{2}\left(e^{i\eta} + e^{-i\eta}\right) e^{i\alpha\sin(\eta-\eta_0)} \\ &= \frac{1}{2}\sum_{n=-\infty}^{+\infty} J_n(\alpha) e^{-in\eta_0}\left(e^{i\eta} + e^{-i\eta}\right) e^{in\eta} \\ &= \frac{1}{2}\sum_{n=-\infty}^{+\infty} J_n(\alpha) e^{-in\eta_0} e^{i(n+1)\eta} + \frac{1}{2}\sum_{n=-\infty}^{+\infty} J_n(\alpha) e^{-in\eta_0} e^{i(n-1)\eta} \\ &= \frac{1}{2}\sum_{n'=-\infty}^{+\infty} J_{n'-1}(\alpha) e^{-i(n'-1)\eta_0} e^{in'\eta} + \frac{1}{2}\sum_{n''=-\infty}^{+\infty} J_{n''+1}(\alpha) e^{-i(n''+1)\eta_0} e^{in''\eta} \\ &= \sum_{n=-\infty}^{+\infty} \frac{1}{2}\left[J_{n-1}(\alpha) e^{-i(n-1)\eta_0} + J_{n+1}(\alpha) e^{-i(n+1)\eta_0}\right] e^{in\eta} \end{aligned}$$

$$\Longleftrightarrow \quad \boxed{C_n = \frac{1}{2}\left[J_{n-1}(\alpha) e^{-i(n-1)\eta_0} + J_{n+1}(\alpha) e^{-i(n+1)\eta_0}\right]}. \tag{B.5}$$

iii. *Identification of* D_n:

$$\sum_{n=-\infty}^{+\infty} D_n e^{in\eta} \stackrel{!}{=} \sin(\eta) e^{i\alpha \sin(\eta-\eta_0)}$$

$$= \frac{1}{2i}\left(e^{i\eta} - e^{-i\eta}\right) \sum_{n=-\infty}^{+\infty} J_n(\alpha) e^{-in\eta_0} e^{-in\eta}$$

$$\Longleftrightarrow \quad \boxed{D_n = \frac{1}{2i}\left[J_{n-1}(\alpha)e^{-i(n-1)\eta_0} - J_{n+1}(\alpha)e^{-i(n+1)\eta_0}\right]}. \tag{B.6}$$

Q.E.D. (5.21)

Now taking $Q_n^\mu \stackrel{\text{def}}{=} q_-^\mu + q_+^\mu - nk^\mu$ for $\mu = 0,1,2,3$, we decompose the integral I of the exponential term in Eq. (5.20) into space and time coordinates

$$\begin{aligned}
I :=& \int d^4x V_{\text{had}}(x) \exp\left[-i\left(q_-^\mu + q_+^\mu - nk^\mu\right) x_\mu\right] \\
=& \frac{g_\sigma^2}{4\pi} \int_{-\infty}^{+\infty} dt \exp\left[-i\left(q_-^0 + q_+^0 - n\omega_L\right) t\right] \cdot \int d^3\vec{x} \frac{\mathrm{e}^{-m_\sigma|\vec{x}|}}{|\vec{x}|} \exp\left[-i\left(\vec{q}_- + \vec{q}_+ - n\vec{k}_L\right)\vec{x}\right] \\
=& \frac{g_\sigma^2}{2}\, \delta\left(q_-^0 + q_+^0 - n\omega_L\right) \cdot \int_0^{+\infty} \mathbf{x}^2 d\mathbf{x} \int_0^\pi \sin\theta\, d\theta \int_0^{2\pi} d\varphi \frac{1}{\mathbf{x}} e^{-i|\vec{Q}_n|\cdot\mathbf{x}\cos\theta - m_\sigma\cdot\mathbf{x}} \\
=& \pi g_\sigma^2\, \delta\left(q_-^0 + q_+^0 - n\omega_L\right) \cdot \int_0^{+\infty} \frac{\mathbf{x} d\mathbf{x}}{+i|\vec{Q}_n|\cdot\mathbf{x}} \int_0^\pi \left(+i|\vec{Q}_n|\cdot\mathbf{x}\sin\theta\right) e^{-i|\vec{Q}_n|\cdot\mathbf{x}\cos\theta - m_\sigma\cdot\mathbf{x}} d\theta \\
=& \pi g_\sigma^2\, \delta\left(q_-^0 + q_+^0 - n\omega_L\right) \cdot \int_0^{+\infty} \frac{d\mathbf{x}}{i|\vec{Q}_n|} e^{-m_\sigma\cdot\mathbf{x}} \left(e^{i|\vec{Q}_n|\cdot\mathbf{x}} - e^{-i|\vec{Q}_n|\cdot\mathbf{x}}\right).
\end{aligned} \tag{B.7}$$

The Integral in the last expression is no more divergent at $x \longrightarrow \infty$, because of the factor $e^{-m_\sigma\mathbf{x}}$. After integral evaluation we obtain

$$\begin{aligned}
I =& \pi g_\sigma^2\, \delta\left(q_-^0 + q_+^0 - n\omega_L\right) \cdot \left\{\frac{1}{i|\vec{Q}_n|} \int_0^{+\infty} d\mathbf{x} \left(e^{(-m_\sigma + i|\vec{Q}_n|)\mathbf{x}} - e^{-(m_\sigma + i|\vec{Q}_n|)\mathbf{x}}\right)\right\} \\
=& \pi g_\sigma^2\, \delta\left(q_-^0 + q_+^0 - n\omega_L\right) \cdot \frac{1}{i|\vec{Q}_n|} \cdot \left\{\frac{1}{-m_\sigma + i|\vec{Q}_n|}\left[e^{(-m_\sigma + i|\vec{Q}_n|)\mathbf{x}}\right]_0^{+\infty} + \frac{1}{m_\sigma + i|\vec{Q}_n|}\left[e^{-(m_\sigma + i|\vec{Q}_n|)\mathbf{x}}\right]_0^{+\infty}\right\} \\
=& \pi g_\sigma^2\, \delta\left(q_-^0 + q_+^0 - n\omega_L\right) \cdot \frac{1}{i|\vec{Q}_n|} \cdot \left\{\frac{2i|\vec{Q}_n|}{m_\sigma^2 + |\vec{Q}_n|^2}\right\} \\
=& \frac{2\pi g_\sigma^2}{m_\sigma^2 + |\vec{Q}_n|^2}\, \delta(Q_n^0).
\end{aligned} \tag{B.8}$$

Finally, the Klein-Gordon $S^{(1)}$-matrix (5.20) becomes

$$S_{\pi^+\pi^-}^{(1)} = \frac{i\pi g_\sigma^2}{V\sqrt{q_-^0 q_+^0}} \cdot \sum_{n\geq n_0}^{+\infty} \frac{\mathcal{M}_n}{m_\sigma^2 + |\vec{Q}_n|^2} \delta(Q_n^0). \tag{B.9}$$

Q.E.D. (5.20)

B.3 The Total Pair Production Rate

Proof of Eqs. (5.25):

The square of the $S^{(1)}$-matrix is

$$|S^{(1)}_{\pi^+\pi^-}|^2 = \frac{\pi^2 g_\sigma^4}{q_-^0 q_+^0 V^2} \cdot \sum_{n\geq n_0} \sum_{n'\geq n_0} \frac{\mathcal{M}_n \mathcal{M}_{n'}}{\left(m_\sigma^2 + |\vec{Q}_n|^2\right)^2} \delta\big(Q_n^0\big)\delta\big(Q_{n'}^0\big). \tag{B.10}$$

For large but finite T we consider transitions in the time interval $[-T/2, T/2]$, during which the total energy of the absorbed photons is equal to the sum of the effective energies of the created $\pi^+\pi^-$ pairs. The energy δ-function can approximately be written as follows

$$\delta\big(Q_{n'}^0\big) \approx \frac{1}{2\pi}\int_{-T/2}^{T/2} dt e^{iQ_{n'}^0 t} = \frac{1}{2\pi Q_{n'}^0} \cdot \left[\sin\left(Q_{n'}^0 t\right) - i\cos\left(Q_{n'}^0 t\right)\right]_{-T/2}^{T/2} = \frac{1}{\pi Q_{n'}^0}\sin\left(\frac{T}{2}Q_{n'}^0\right). \tag{B.11}$$

Since

$$\lim_{Q_{n'}^0\to 0}\delta\big(Q_{n'}^0\big) = \frac{T}{2\pi}\lim_{Q_{n'}^0\to 0}\frac{\sin\left(\frac{T}{2}Q_{n'}^0\right)}{\left(\frac{T}{2}Q_{n'}^0\right)} = \frac{T}{2\pi},$$

we arrive under the constraint $Q_{n'}^0 \to 0$ at

$$|S^{(1)}_{\pi^+\pi^-}|^2 = \frac{\pi g_\sigma^4}{2V^2 q_-^0\, q_+^0} \cdot T \sum_{n\geq n_0} \frac{\mathcal{M}_n^2}{\left(m_\sigma^2 + |\vec{Q}_n|^2\right)^2}\delta\big(Q_n^0\big). \tag{B.12}$$

We know that the dynamics of $\pi^+\pi^-$ mesons is described by the Gordon-Volkov wave functions (5.14) with the wave numbers $\vec{k}_\mp = 2\pi/\lambda_\mp = \vec{q}_\mp$ (We always use the H.-L. units (1)). Let us require that the density of states for these wave functions is stationary in a box having a large (but finite) volume $V = L^3$, that is

$$L = n_x^\mp \lambda_x^\mp, \quad L = n_y^\mp \lambda_y^\mp \ \text{ and } \ L = n_z^\mp \lambda_z^\mp \quad \Longleftrightarrow \quad k_x^\mp \cdot L = 2\pi n_x^\mp, \quad k_y^\mp \cdot L = 2\pi n_y^\mp \ \text{ and } \ k_z^\mp \cdot L = 2\pi n_z^\mp.$$

Then we get

$$d^3 n_\mp = dn_x dn_y dn_z = \frac{L^3}{(2\pi)^3} d\vec{k}_x^\mp d\vec{k}_y^\mp d\vec{k}_z^\mp = \frac{V}{(2\pi)^3} d\vec{k}_\mp = \frac{V}{(2\pi)^3} d^3\vec{q}_\mp.$$

The differential rate for $\pi^+\pi^-$ pair production by absorbing $n \geq n_0$ photons is given by

$$\begin{aligned}
d^6 R =& \frac{1}{T} d^3 n_+ d^3 n_- |S^{(1)}_{\pi^+\pi^-}|^2 \\
& \frac{1}{T}\frac{V d^3\vec{q}_+}{(2\pi)^3}\frac{V d^3\vec{q}_-}{(2\pi)^3}|S^{(1)}_{\pi^+\pi^-}|^2 \\
=& \frac{\pi g_\sigma^4}{2(2\pi)^6}\sum_{n\geq n_0}\frac{d^3\vec{q}_+}{q_+^0}\frac{d^3\vec{q}_-}{q_-^0}\frac{\mathcal{M}_n^2}{\left(m_\sigma^2 + |\vec{Q}_n|^2\right)^2}\delta\big(Q_n^0\big) \\
=& \frac{\pi g_\sigma^4}{2(2\pi)^6}\sum_{n\geq n_0}\frac{|\vec{q}_+|^2}{q_+^0} d|\vec{q}_+| \sin\theta_+ d\theta_+ d\varphi_+ \frac{|\vec{q}_-|^2}{q_-^0} d|\vec{q}_-| \sin\theta_- d\theta_- d\varphi_- \frac{\mathcal{M}_n^2}{\left(m_\sigma^2 + |\vec{Q}_n|^2\right)^2}\delta\big(Q_n^0\big).
\end{aligned} \tag{B.13}$$

In the last line we expressed $d^3\vec{q}_\mp$ in spherical coordinates, $d^3\vec{q}_\mp \equiv |\vec{q}_\mp|^2 d|\vec{q}_\mp| \sin\theta_\mp d\theta_\mp d\varphi_\mp$. The quantities q_-^μ and q_+^μ are Lorentz-invariant, that is:

$$q_\mp^2 = const. \Longrightarrow 2q_\mp^\mu dq_{\mp\mu} = 0 \Longleftrightarrow |\vec{q}_\mp| d|\vec{q}_\mp| = q_\mp^0 dq_\mp^0.$$

Multiplying each side of $|\vec{q}_-| d|\vec{q}_-| = q_-^0 dq_-^0$ by $|\vec{q}_-|\delta\big(Q_n^0\big)$ yields

$$|\vec{q}_-|^2 d|\vec{q}_-|\delta\big(q_+^0 + q_-^0 - nk^0\big) = |\vec{q}_-| q_-^0 dE_- \delta(E_+ + E_- - n\omega_L).$$

Integrating over E_- we obtain

$$d^5R = \frac{\pi g_\sigma^4}{2(2\pi)^6}\sum_{n\geq n_0} dE_+ \sin\theta_+ d\theta_+ d\varphi_+ \sin\theta_- d\theta_- d\varphi_- |\vec{q}_+||\vec{q}_-| \frac{\mathcal{M}_n^2}{\left(m_\sigma^2+|\vec{Q}_n|^2\right)^2} \underbrace{\int_{m_\pi^*}^{n\omega_L - m_\pi^*} dE_- \delta(E_+ + E_- - n\omega_L)}_{=1},$$

$$\Longleftrightarrow d^5R = \frac{\pi g_\sigma^4}{2(2\pi)^6}\sum_{n\geq n_0} dE_+ \sin\theta_+ d\theta_+ d\varphi_+ \sin\theta_- d\theta_- d\varphi_- |\vec{q}_+||\vec{q}_-| \frac{\mathcal{M}_n^2}{\left(m_\sigma^2+|\vec{Q}_n|^2\right)^2}. \tag{B.14}$$

Taking into account that d^5R independent on φ_+ and integrating over all possible momenta yields the total number of produced $\pi^+\pi^-$ pairs per time by absorbing $n \geq n_0$ photons

$$\boxed{R = \frac{g_\sigma^4}{64\pi^4}\sum_{n\geq n_0}\int_{m_\pi^*}^{n\omega_L - m_\pi^*} dE_+ \int_0^\pi \sin\theta_+ d\theta_+ \int_0^\pi \sin\theta_- d\theta_- \int_0^{2\pi} d\varphi_- \frac{|\vec{q}_+||\vec{q}_-|}{\left(m_\sigma^2+|\vec{Q}_n|^2\right)^2}\mathcal{M}_n^2}. \tag{B.15}$$

Q.E.D. (5.25)

B.4 Intensity of a Laser Field

Proof of Eqs. (5.10):

We have assumed the laser field to be a monochromatic, linearly polarized or circularly polarized plane wave with the four-potential given by Eq. (3.7). We work as before in the Coulomb gauge with div $\vec{A}_L = 0$ and vanishing scalar potential, $V_L = 0$. We have

$$\vec{A}_L = a\cos(\omega_L t - \omega_L z)\cdot\vec{e}_x + a\delta_0 \sin(\omega_L t - \omega_L z)\cdot\vec{e}_y = A_x\cdot\vec{e}_x + A_y\cdot\vec{e}_y.$$

The magnetic field is

$$\vec{B}_L = \overrightarrow{\text{rot}}\ \vec{A}_L = \vec{\nabla}\times\vec{A}_L = a\omega_L\delta_0\cos(\omega_L t - \omega_L z)\cdot\vec{e}_x + a\omega_L\sin(\omega_L t - \omega_L z)\cdot\vec{e}_y \quad \text{and} \quad B_L \equiv \|\vec{B}_L\| = a\omega_L.$$

The electrostatic field is

$$\vec{E}_L = -\underbrace{\overrightarrow{\text{grad}}\ V_L}_{=0} - \frac{\partial\vec{A}_L}{\partial t} = a\omega_L\sin(\omega_L t - \omega_L z)\cdot\vec{e}_x - a\omega_L\delta_0\cos(\omega_L t - \omega_L z)\cdot\vec{e}_y \quad \text{and} \quad E_L \equiv \|\vec{E}_L\| = a\omega_L.$$

The corresponding Poynting vector is

$$\vec{R}_L \overset{\text{def.}}{=} \vec{E}_L\times\vec{H}_L = \frac{1}{\mu_0\mu_r}\vec{E}_L\times\vec{B}_L = \frac{\varepsilon_0 c^2}{\mu_r}\vec{E}_L\times\vec{B}_L = \frac{\varepsilon_0 c^2}{\mu_r}a^2\omega_L^2\left[\sin^2(\omega_L t - \omega_L z) + \delta_0^2\cos^2(\omega_L t - \omega_L z)\right]\cdot\vec{e}_z.$$

Since the intensity of the electromagnetic field of the laser is the time-averaged magnitude of the Poynting vector, then we get

$$I^{\text{medium}}_{\text{plane wave}} \overset{\text{def.}}{=} \|\langle\vec{R}_L\rangle\| = \frac{\varepsilon_0}{2\mu_r}(1+\delta_0^2)(a\omega_L c)^2.$$

In vacuum the relative permeability μ_r is equal to 1 an then

$$I^{\text{vacuum}}_{\text{plane wave}} = \frac{1}{2}(1+\delta_0^2)\varepsilon_0 c^2(a\omega_L)^2 \quad \text{with} \quad (a\omega_L)^2 = E_L^2 = B_L^2.$$

Thus, in H.-L. units we obtain

$$I^{\text{vacuum}}_{\text{plane wave}} = \frac{1}{2}(1+\delta_0^2)(a\omega_L)^2. \tag{B.16}$$

Acknowledgements

First, I would like to thank gratefully my Supervisors Prof. Dr. Dr. Carsten Müller and Prof. Dr. Christoph H. Keitel for their guidances and supports and who have kept me on the right track throughout my research.

I thank B. Kopeliovich, H.J. Pirner, and B. Povh for helpful discussions on various aspects of hadronic interactions. A.D. gratefully acknowledges the scholarship support from the International Max-Planck Research School for Quantum Dynamics in Physics, Chemistry and Biology (IMPRS-QD).

I would like to thank Dr. Karen Z. Hatsagortsyan for the helpful discussions on multiphoton physics and recollision dynamics.

I express my gratitude to my family members in Tunisia, especially to: Jeddi-Mohammad Dadi, Ommi-Lemha Dekim, Ommi-Hlima Bent Issa, Ammi-Salem Ben Mashoud, Mabrouka Dekim, Ali Htiwech, Khali-Abdallah Dekim, Bechir Ben-Bilgacem, Ammi-El-Hussein, Bachar, Kaies, Sofien, Sonia, Marwa, Ezzeddine, Jemhi,..., who have been a constant support to me through my whole life, this thesis is for you.

Finally, in the spirit of leaving the best till last, I wish to thank my most distinguished wife, Aicha Bendada for sharing her feelings with me, for her help and support, and for her sacred dedication to my family life, which has allowed me to complete this thesis.

Declaration

The work presented in this thesis is based on research carried out at the Max Planck Institute for Nuclear Physics (MPIK) in Heidelberg, Germany, within the Theory Division of Prof. Dr. Keitel, *Theoretical Quantum Dynamics in Intense Laser Fields*. No part of this thesis has been submitted elsewhere for any other degree or qualification and it is all my own work unless referenced to the contrary in the text.

Signed from, Anis Dadi (Signer) **on**, Monday, February 20, 2012 (date) **in** Heidelberg/Germany (place)

Bibliography

[1] P. J. Mohr, B. N. Taylor and D. B. Newell, Reviews of Modern Physics **80**, 633-730 (2008).

[2] J. Chadwick and M. Goldhaber, Nature **134**, 237 (1934); Proc. R. Soc. A **151**, 479 (1935).

[3] W. Gentner, Compt. Rend. **199**, 1211 (1934); W. Bothe and W. Gentner, Z. Phys. **106**, 236 (1937); **112**, 45 (1939).

[4] G. C. Baldwin and G. Klaiber, Phys. Rev. **71**, 3 (1947).

[5] S. E. Woosley and W. M. Howard, Astrophys. J. Suppl. Ser. **36**, 285 (1978).

[6] M. Rayet *et al.*, Astron. Astrophys. **298**, 517 (1995).

[7] C. Nair *et al.*, Phys. Rev. C **78**, 055802 (2008).

[8] R. Röhlsberger *et al.*, Science **328**, 1248 (2010).

[9] H. Schwoerer, J. Magill, and B. Beleites (Eds.), Lasers and Nuclei (Springer, Heidelberg, 2006).

[10] K. W. D. Ledingham, P. McKenna, and R. P. Singhal, Science **300**, 1107 (2003).

[11] D. Umstadter, J. Phys. D **36**, R151 (2003).

[12] K. W. D. Ledingham and W. Galster, New J. Phys. **12**, 045005 (2010).

[13] For details and the current status, see http://www.elilaser.eu. Potential applications are also discussed in D. Habs, T. Tajima, J. Schreiber, C. P. J. Barty, M. Fujiwara, and P. G. Thirolf, Eur. Phys. J. D **55**, 279 (2009).

[14] H. Chen *et al.*, Phys. Rev. Lett. **105**, 015003 (2010).

[15] A. I. Titov, B. Kämpfer, and H. Takabe, Phys. Rev. ST Accel. Beams **12**, 111301 (2009).

[16] S. Karsch *et al.*, Laser Part. Beams **17**, 565 (1999).

[17] C. Müller, K. Z. Hatsagortsyan, and C. H. Keitel, Phys. Lett. B **659**, 209 (2008).

[18] I. Kuznetsova, D. Habs, and J. Rafelski, Phys. Rev. D **78**, 014027 (2008).

[19] M. H. Thoma, Rev. Mod. Phys. **81**, 959 (2009).

[20] V. N. Nedoreshta, S. P. Roshchupkin, and A. I. Voroshilo, Laser Phys. **19**, 531 (2009).

[21] P. Kálmán and J. Bergou, Phys. Rev. C **34**, 1024 (1986).

[22] P. Kálmán, Phys. Rev. C **39**, 2452 (1989).

[23] D. Kis, P. Kálmán, T. Keszthelyi, and J. Szívós, Phys. Rev. A **81**, 013421 (2010).

[24] S. Matinyan, Phys. Rep. **298**, 199 (1998).

[25] A. Shahbaz, C. Müller, T. J. Bürvenich, and C. H. Keitel, Nucl. Phys. A **821**, 106 (2009).

[26] T. J. Bürvenich, J. Evers, and C. H. Keitel, Phys. Rev. Lett. **96**, 142501 (2006).

[27] A. Pálffy, J. Evers, and C. H. Keitel, Phys. Rev. C **77**, 044602 (2008).

[28] H. R. Reiss, Phys. Rev. C **27**, 1199 (1983).

[29] E. K. Akhmedov, Sov. Phys. JETP **58**, 883 (1983).

[30] A. Cionga, V. Florescu, A. Maquet and R. Taïeb , Phys. Rev. A **47**, 1830-1840 (1993).

[31] T. E. Glover, R. W Schoenlein, A. H. Chin, and C. V. Shank, Phys. Rev. Lett. **76**, 2468 (1996).

[32] C. Leone *et al.*, Phys. Rev. A **38**, 5642-5651 (1988).

[33] D. B. Milošević and F. Ehlotzky, Phys. Rev. A **57**, 2859-2866 (1998).

[34] P. OKeeffe *et al.*, Phys. Rev. A **69**, 051401(R) (2004).

[35] M. Meyer *et al.*, Phys. Rev. A **74**, 011401(R) (2006); Phys. Rev. Lett. **101**, 193002 (2008).

[36] D. Burke *et al.*, Phys. Rev. Lett. **79**, 1626 (1997).

[37] A. Braghieri *et al.*, Phys. Lett. B **363**, 46 (1995).

[38] J. Ahrens *et al.*, Phys. Lett. B **551**, 49 (2003).

[39] J. Ajaka *et al.*, Phys. Lett. B **475**, 372 (2000).

[40] Y. Assafiri *et al.*, Phys. Rev. Lett. **90**, 222001 (2003).

[41] O. Bartalini *et al.*, Eur. Phys. J. A **26**, 399 (2005).

[42] S. Strauch *et al.*, Phys. Rev. Lett. **95**, 162003 (2005).

[43] M. Battaglieri *et al.*, Phys. Rev. D **80**, 072005 (2009).

[44] D. Dale *et al.*, PRIMEX Experiment, JLab-E-02-103.

[45] H. R. Reiss, J. Math. Phys. **3**, 59 (1962).

[46] A. I. Nikishov and V. I. Ritus, Zh. Eksp. Teor. Fiz. **46**, 776 (1964) [Sov. Phys. JETP **19**, 529 (1964)].

[47] H. Mitter, Acta Phys. Austr. Suppl. **14**, 397 (1975).

[48] P. Möller *et al.*, At. Data Nucl. Data Tables **39**, 225 (1988).

[49] W. D. Myers and W. J. Swiatecki, Phys. Rev. C **57**, 3020 (1998).

[50] A. Bohr and B. R. Mottelson, Nuclear Structure, Vol. I (World Scientific, Singapore, 1998).

[51] P. A. Seeger and W. M. Howard, Nucl. Phys. A **238**, 491-532 (1975).

[52] G. E. Brown, J. H. Gunn, and P. Gould, Nucl. Phys. **46**, 598 (1963).

[53] M. Jaminon and C. Mahaux, Phys. Rev. C **40**, 354 (1989).

[54] C. H. Johnson, D.J. Horn, and C. Mahaux, Phys. Rev. C **36**, 2252 (1987).

[55] J. P. Blaizot *et al.*, Nucl. Phys. A **591**, 435 (1995).

[56] D. H. Youngblood *et al.*, Phys. Rev. Lett. **82**, 691 (1999).

[57] U. Garg *et al.*, Nucl. Phys. A **788**, 36 (2007).

[58] J. Piekarewicz, Phys. Rev. C **69**, 041301 (2004).

[59] T. Li *et al.*, Phys. Rev. Lett. **99**, 162503 (2007).

[60] G. Colo *et al.* Phys. Rev. C **70**, 024307 (2004).

[61] T. Minamisono *et al.*, Phys. Rev. Lett. **69**, 2058 (1992).

[62] A. Dadi, Phys. Rev. C **82**, 025203 (2010).

[63] I. Tanihata *et al.*, Phys. Rev. Lett. **55**, 2676 (1985).

[64] P. G. Hansen and B. Jonson, Europhys. News **4**, 409 (1987).

[65] T. Aumann *et al.*, Phys. Rev. C **59**, 1252-1262 (1999).

[66] N. Fukuda *et al.*, Phys. Rev. C **70**, 054606 (2004).

[67] T. Nakamura *et al.*, Phys. Rev. Lett. **83**, 1112-1115 (1999).

[68] I. Mazumdar, V. Arora, and V. S. Bhasin, Phys. Rev. C **61**, 051303(R) (2000).

[69] L. Trache *et al.*, Phys. Rev. Lett. **87**, 271102 (2001).

[70] D. Cortina-Gil *et al.*, Phys. Lett. B **529**, 36 (2002).

[71] D. Cortina-Gil *et al.*, Nucl. Phys. A **720**, 3 (2003).

[72] R. N. Majumdar, J. Phys. Soc. Jpn. **72**, 3087 (2003).

[73] M. S. Hussein *et al.*, Phys. Lett. B **640**, 91 (2006).

[74] T. Sumikama *et al.*, Phys. Rev. C **74**, 024327 (2006).

[75] S. Karataglidis and K. Amos, Phys. Lett. B **650**, 148 (2007).

[76] C. A. Bertulani, J. Phys. G: Nucl. Part. Phys. **34**, 315 (2007).

[77] R. Kanungo *et al.*, Phys. Lett. B **571**, 21-28 (2003).

[78] J. Schaffner-Bielich, J. A. Maruhn, H. Stöcker, and W. Greiner, Z. Phys. A **350**, 91-92 (1994).

[79] H. Lenske., J. Phys. G: Nucl. Part. **24**, 1429 (1998).

[80] T. Baker *et al.*, Phys. Rep. **289**, 235 (1997).

[81] G. Audi and A. H. Wapstra, Nucl. Phys. A **565**, 1 (1993).

[82] G. Audi, O. Bersillon, J. Blachot, and A. H. Wapstra, Nucl. Phys. A **729**, 3 (2003).

[83] M. Fukuda *et al.*, Nucl. Phys. A **656**, 209-228 (1999).

[84] Q. R. Ahmad *et al.*, Phys. Rev. Lett. **89**, 011301 (2002).

[85] S. N. Ahmed *et al.*, SNO Collaboration, Phys. Rev. Lett. **92**, 181301 (2004).

[86] H. Primakoff, Phys. Rev. **81**, 899 (1951).

[87] M. Zielinski *et al*, Phys. Rev. D **29**, 2633-2635 (1984).

[88] Y. Suzuki, R. G. Lovas, K. Yabana, and K. Varga, "*Structure and Reactions of Light Exotic Nuclei*", p 446-456, Taylor & Francis, London (2003).

[89] S. S. Chandel and S. K. Dhiman, Phys. Rev. C **68**, 054320 (2003).

[90] Y. Ogawa, K. Yabana, and Y. Suzuki, Nucl. Phys. A **543**, 722 (1992).

[91] K. Yabana, Y. Ogawa, and Y. Suzuki, Nucl. Phys. A **539**, 295 (1992).

[92] W. Koepf, Y. K. Gambhir, P. Ring, and M. M. Sharma, Z. Phys. A 340, 119 (1991).

[93] J. Meng and P. Ring, Phys. Rev. Lett. **77**, 3963-3966 (1996).

[94] F. Ehlotzky, K. Krajewska, and J. Z. Kamiński, Rep. Prog. Phys. **72**, 046401 (2009).

[95] C. Müller, A. B. Voitkiv, and N. Grün, Phys. Rev. A **70**, 023412 (2004).

[96] P. Sieczka *et al.*, Phys. Rev. A **73**, 053409 (2006).

[97] K. Krajewska and J. Z. Kaminski, Phys. Rev. A **82**, 013420 (2010).

[98] A. I. Milstein *et al.*, Phys. Rev. A **73**, 062106 (2006).

[99] A. Di Piazza *et al.*, Phys. Rev. A **81**, 062122 (2010).

[100] M. Yu. Kuchiev, Phys. Rev. Lett. **99**, 130404 (2007).

[101] A comparison with e^+e^- pair production in relativistic collisions of two nuclei may be found in G. Baur, K. Hencken, and D. Trautmann, Phys. Rep. **453**, 1 (2007).

[102] C. Müller, C. Deneke, and C. H. Keitel, Phys. Rev. Lett. **101**, 060402 (2008).

[103] C. Müller, Phys. Lett. B **672**, 56 (2009).

[104] G. Ewald *et al.*, Phys. Rev. Lett. **93**, 113002 (2004); Phys. Rev. Lett. **94**, 039901 (2005).

[105] D. Strickland and G. Mourou, Opt. Commun. **56**, 219 (1985).

[106] K. W. D. Ledingham *et al.*, Phys. Rev. Lett. **84**, 899 (2000).

[107] T. E. Cowan *et al.*, ibid. **84**, 903 (2000).

[108] T. Ditmire *et al.*, Nature (London) **398**, 489 (1999).

[109] R. A. Snavely *et al.*, Phys. Rev. Lett. **85**, 2945-2948 (2000).

[110] P. McKenna *et al.*, Phys. Rev. Lett. **91**, 075006 (2003).

[111] S. -W. Bahk *et al.*, Opt. Lett. **29**, 2837-2839 (2004).

[112] T. Zh. Esirkepov *et al.*, JETP Lett. **70**, 82 (1999).

[113] A. Dubietis *et al.*, Opt. Commun. **88**, 437-440, (1992).

[114] J. Fuchs *et al.*, Nature Phys. **2**, 48 (2006).

[115] L. Robson *et al.*, Nature Phys. **3**, 58 (2007).

[116] A. Pukhov, Nature Phys. **2**, 439 (2006); B. Dromey *et al.*, Nature Phys. **5**, 146 (2009).

[117] M. Klaiber *et al.*, Opt. Lett. **33**, 411 (2008), and references therein.

[118] C. B. Collins and L. A. Rivlin (eds.), Gamma-Ray Lasers: Proceedings of the 1st International Gamma-Ray Laser Workshop (GARALAS'95), Predeal, Romania, August 1995, Hyp. Interact. **107** (1997).

[119] G. T. Trammel, J. T Hutton, and J. P. Hannon, J. Quant. Spect. Rad. Transfer **40**, 693 (1988).

[120] V. Muccifora *et al.*, Nucl. Phys. A **711**, 254 (2002).

[121] H. Ohgaki *et al.*, Nucl. Instr. and Meth. A **353**, 384 (1994).

[122] D. M. Volkov, Z. Phys. **94**, 250 (1935).

[123] J.-F. Lu and S. I. Kruglov, J. Phys. G **20**, 1017 (1994).

[124] U. Kneissl *et al.*, Nucl. Phys. A **264**, 30 (1976).

[125] H. Ueno *et al.*, Phys. Rev. C **80**, 064609 (2009).

[126] B. A. Perdue *et al.*, Phys. Rev. C **83**, 034003 (2011).

[127] A. Kh. Shardanov and B. A. Yuryev, Yad. Fiz. **8**, 424 (1968).

[128] D. W. Anderson *et al.*, Phys. Rev. C **9**, 1919-1923 (1974).

[129] H. Ueno *et al.*, J. Phys. Soc. Jpn. **73**, 875 (2004).

[130] T. Rauscher, Phys. Rev. C **73**, 015804 (2006).

[131] W. Rapp, J. Görres, M. Wiescher, H. Schatz and F. Käppeler, Astrophys. J. **653**, 474 (2006).

[132] M. Altarelli *et al.*, Technical Design Report of the European XFEL, DESY, 2006-097 (http://www.xfel.net).

[133] L. F. DiMauro *et al.*, J. Phys. Conf. Ser. **88**, 012058 (2007).

[134] H. Feshbach *et al.*, Advances in Nuclear Phys. Vol. **25**, 207 (2000), Kluwer Academic/Plenum Publishing Corp., N.Y.

[135] L. D. Landau and E. M. Lifschitz, "Lehrbuch der Theoretischen Physik", Bd. **III**, Quantenmechanik (Akademie-Verlag, Berlin, 1974).

[136] R. Raut *et al.*, Phys. Rev. Lett. **108**, 042502 (2012).

[137] Carchon, R. Van de Vyver, H. Ferdinande, J. Devos, and E. Van Camp, Phys. Rev. C **14**, 456 (1976).

[138] *Handbook on Photonuclear Data for Applications-Cross Sections and Spectra*, IAEA-TECDOC-1178 (2000).

[139] E. G. Fuller, Phys. Rep. **127**, 185-231 (1985).

[140] G. Breit and E. P. Wigner, Phys. Rev. **49**, 519 (1936).

[141] E. Segré, "*Nuclei and Particles*", p. 497-498, Benjamin, London, (1977).

[142] F. E. Low, Phys. Rev. **110**, 974-977 (1958).

[143] R. A. Fox, R. M. Kogan, and E. J. Robinson , Phys. Rev. Lett. **26**, 1416-1417 (1971).

[144] R. M. Kogan, R. A. Fox, G. T. Burnham, and E. J. Robinson, Bull. Amer. Phys. Soc. **16**, 1411 (1971).

[145] J. P. Hernandez and A. Gold, Phys. Rev. **156**, 26-35 (1967).

[146] P. Lambropoulos, Phys. Rev. **168**, 1418 (1968); Phys. Rev. **144**, 1081 (1966).

[147] P. Lambropoulos, Phys. Rev. Lett. **28**, 585 (1972).

[148] T. Nakajima and G. Buica, Phys. Rev. A **74**, 023411 (2006).

[149] G. Buica and T. Nakajima, Phys. Rev. A **81**, 043418 (2010).

[150] http://lhc.web.cern.ch/lhc

[151] W. Ackermann *et al.*, Nat. Photon. **1**, 336 (2007).

[152] L. Young *et al.*, Nature **466**, 56 (2010).

[153] K. Nakajima, Nature Phys. **4**, 92 (2008), and references therein.

[154] A. Di Piazza, G. Calucci, Mod. Phys. Lett. A **20**, 117 (2005).

[155] V. Yu. Bychenkov *et al.*, Pis'ma Zh. Eksp. Teor. Fiz. **74**, 664 (2001) [JETP Lett. **74**, 586 (2001)].

[156] C. Itzykson and J. B. Zuber, *Quantum Field Theory* (McGraw-Hill, New York, 1980), Chapter 2-2-3.

[157] J. A. Gómez Tejedor and E. Oset, Nucl. Phys. A **571**, 667 (1994); J. C. Nacher *et al.*, Nucl. Phys. A **695**, 295 (2001).

[158] S. Nozawa, B. Blankleider, and T. H. Lee, Nucl. Phys. A **513**, 459-510 (1990).

[159] T. Sato and T. H. Lee, Phys. Rev. C **54**, 2660-2684 (1996); Phys. Rev. C **63**, 055201 (2001).

[160] M.G. Fuda and H. Alharbi, Phys. Rev. C **68**, 064002 (2003).

[161] V. Pascalutsa and J. A. Tjon, Phys. Rev. C **70**, 035209 (2004).

[162] M. G. Olsson, Nucl. Phys. B **78**, 55-76 (1974).

[163] M. G. Olsson and E. T. Osypowski, Phys. Rev D **17**, 174-184 (1978).

[164] R. M. Davidson, N. C. Mukhopadhyay, and R. S. Wittman, Phys. Rev. D **43**, 71-94 (1991).

[165] R. L. Walker, Phys. Rev. **182**, 1729-1748 (1969).

[166] D. Drechsel *et al.*, Nucl. Phys. A **645**, 145-174 (1999).

[167] I. G. Aznauryan, Phys. Rev. C **67**, 015209 (2003).

[168] Z. Li *et al.*, Phys. Rev. C **56**, 1099-1113 (1997); Q. Zhao *et al.*, Phys. Rev. C **65**, 065204 (2002).

[169] H. -P. Schlenvoigt *et al*, Nature Physics **4**, 130 (2008).

[170] P. Abbon *et al.*, Nucl. Inst. Meth. A **577**, 455 (2007).

[171] Yu. M. Antipov *et al.*, Phys. Lett. B **121**, 445 (1983).

[172] J. Hüfner, Phys. Rep. **21**, 1 (1975).

[173] C. J. Horowitz, H. O. Meyer, and D. K. Griegel, Phys. Rev. C **49**, 1337 (1994).

[174] B. D. Serot and J. D. Walecka, *The Relativistic Nuclear Many-Body Problem*, in: Adv. Nucl. Phys. **16**, (Plenum Press, New York, 1986), edited by J. W. Negele and E. Vogt.

[175] G. Gialanella *et al.*, Nuovo Cimento A **63**, 892 (1969).

[176] Focusing of 20-keV x-rays below 10 nm in one direction has been demonstrated in H. Mimura *et al.*, Nature Phys. **6**, 122 (2010).

[177] S. J. Müller and C. Müller, Phys. Rev. D **80**, 053014 (2009).

[178] Y. I. Salamin, S. X. Hu, K. Z. Hatsagortsyan, and C. H. Keitel, Phys. Rep. **427**, 41 (2006).

[179] J. Schaffner-Bielich *et al.* , Phys. Rev. Lett. **89**, 171101 (2002).

[180] U. Mosel, Hadron Spectroscopy: Tenth International Conference on Hadron Spectroscopy. AIP Conference Proceedings, Volume **717**, 733-742 (2004).

[181] R. Dörner *et al.*, Phys. Rev. Lett. **77**, 1024 (1996); L. A. A. Nikolopoulos, P. Lambropoulos, J. Phys. B **34**, 545 (2001).